XFD Progress Report

December 2002

Table of Contents

1   SRI-CAT BEAMLINES, TECHNICAL DEVELOPMENTS, AND SCIENTIFIC APPLICATIONS

1.1 Introduction

In May 2002, the Advanced Photon Source (APS) was reorganized into three divisions: the Accelerator Systems Division (ASD), the APS Operations Division (AOD), and the Experimental Facilities Division (XFD). Parts of the former User Program Division (UPD) were incorporated into XFD; other parts were incorporated into AOD. This *Progress Report* summarizes the main scientific and technical activities of XFD and parts of the former UPD from January 2001 through June 2002.

The report is divided into two major sections, 1) SRI-CAT Beamlines, Technical Developments, and Scientific Applications, and 2) User Technical Support, which describe the technical activities and research and development (R&D) accomplishments of the XFD and former UPD personnel in supporting the synchrotron radiation instrumentation (SRI) collaborative access team (CAT) and the general APS user community. Also included in this report is a comprehensive list of publications (see Appendix) by XFD and UPD staff members during the time period covered by this report.

The SRI CAT members have made a major impact on the development of new synchrotron radiation optics, instrumentation, and techniques. These state-of-the-art developments have attracted significant scientific community to SRI CAT beamlines and experimental capabilities. In the last two years, SRI CAT conducted collaborative research with more than 100 groups from different institutions and universities. In fall 2002, SRI CAT scheduled more than 50% of beam time for general users proposals. Both of these facts are clear illustration of the dedication of the SRI CAT staff to serve the user community effectively.

In addition to general user support on instrumentation development, SRI CAT has served the synchrotron radiation community in other ways as well. The SRI CAT often served as a test-bed for new accelerator concepts, such as quantitative characterization of the microfocused flux and beam coherence with reduced emittance operation in sector 2 and the canted undulator scheme for operating two beamlines from a single straight section, a prototype of which has been implemented in sector 4. The SRI CAT played an important part in better understanding the effect of top-up on photon beam stability and how these effects can be mitigated through gating techniques.

Members of SRI CAT have also played important roles in the development and running of the National School for Neutron and X-ray Scattering, which has been hosted by Argonne National Laboratory (ANL) for the last several summers. The goal of the school is to provide training for graduate students in the use of national user facilities, such as the APS.

SRI CAT also organized several user science workshops on biological/biomedical applications of x-ray microscopy, polarized x-rays, inelastic x-ray scattering, and nanoscale materials research. New initiatives drawing upon these workshops have resulted in new CATs, such as IXS CAT and Nano-CAT.

Significant accomplishments also took place in the area of user technical support. Staff members from both XFD and ASD completed the final design of the straight section and front end that accommodates the canted undulator setup—the system of choice for new structural biology CATs.

Advanced crystal, zone plate, and mirror x-ray optics have been developed with strong collaboration with the APS user community. Especially noteworthy is the development of profile coating by sputter deposition for the production of aspherical x-ray optical surfaces. This technology has recently been applied to fabricate elliptically shaped Kirkpatrick-Baez mirrors. Also noteworthy is the development and fabrication of a refractory x-ray lens having an adjustable focus.

Significant progress has been made in the area of high-energy x-ray technique development. In particular, the development of high-energy small-angle scattering combined with high-energy wide-angle scattering is proving to be a powerful new technique to study materials systems. The combination of these two techniques allows the gathering of information on texture, strain, and phase with simultaneous information on longer length scales probed by small-angle scattering.

Noteworthy advances were made in both x-ray microscopy techniques and applications,

especially in the biological and materials sciences. Highlights in this report include trace element analysis in marine protists by scanning fluorescence microscopy and microdiffraction imaging of antiferro-magnetic domains in chromium.

The program that utilizes polarization properties of x-rays advanced significantly in the last year. As an example, the strength and extent of interlayer exchange coupling and magnetic roughness was measured on Gd/Fe multilayers. This quantitative information was obtained by performing both x-ray resonance exchange scattering (XRES) and x-ray magnetic circular dichroism (XMCD) measurements.

Both SRI-CAT and user technical support have reached a mature state and are prepared for new challenges in the future.

1.2 X-ray Imaging and Optics Development

The effort in x-ray optics and imaging is on development of x-ray interferometers, development of propagation phase-contrast imaging, and high-heat-load optics. In particular, the phase-contrast imaging experiments are being conducted with scientists who were previously not synchrotron users. Through these collaborations, we hope to open a new experimental field to researchers in areas such as entomology.

1.2.1 Fresnel Propagation X-ray Phase-Contrast Imaging

The contrast in this technique is due to Fresnel diffraction. It corresponds to the defocusing technique in electron microscopy and is sensitive to the second derivative of

the phase. Its principal advantage is the simplicity of the setup. Furthermore, submicron resolution is achievable. This technique is made possible by the lateral coherence of the x-ray beam produced by third-generation synchrotron sources.

A drawback of the propagation technique is the nontrivial relationship between the object and the recorded image (actually a Fresnel diffraction pattern). But when a quantitative (numerical) retrieval of the phase is not needed, it can also be used in a qualitative way, namely, in the edge-detection regime.

This technique has been applied to a wide variety of systems. We imaged stainless-steel fuel injectors several millimeters in thickness using 70 keV x-rays (Lee et al., 2001). The results suggest the possibility of time-resolved studies. The superior spatial resolution of this technique allowed the examination of small (micron) crack openings in aluminum samples as a function of applied load. This is being used to help understand roughness-induced fatigue crack closures (Stock et al., submitted).

Phase-contrast imaging is a valuable tool to distinguish between two phases of the same material in a sample. As an example of this, we could see calcite crystal reinforcement at the incisal end of sea urchin teeth, as part of its strengthening and self-sharpening strategies (Stock et al., in press).

Working at relatively high energy (22 keV) with biological samples to reduce absorption, we could keep small insects alive for more than ten minutes and study their feeding and respiration mechanisms (Westneat et al., 2002). For instance, a new mechanism of tracheal pumping in the head and prothorax has been observed. An

example of the images from this work is shown in Fig. 1.1.

1.2.2 X-ray Imaging of Shock Waves Generated by High-Pressure Fuel Sprays

High-pressure, high-speed sprays are an essential technology in many applications, including fuel injection systems, thermal and plasma spray coatings, and liquid-jet machining. These liquid jets, often traveling at supersonic speeds, are optically opaque due to the highly dense liquid droplets surrounding the sprays. The detailed structure of the sprays, which is directly related to their effectiveness, cannot be resolved by optical methods. In the case of fuel injection, an understanding of the structure and dynamics of the jets is critical in optimizing the injection process to increase fuel efficiency and reduce emissions. In collaboration with Cornell University and ANL Energy Systems Division, we have used synchrotron x-radiography and a novel fast x-ray detector
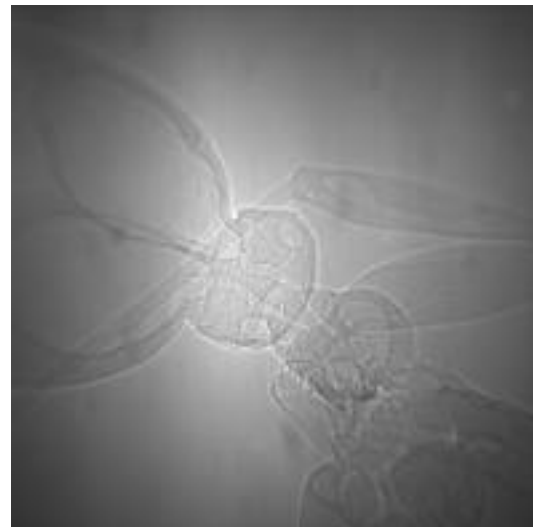

Fig. 1.1. Phase-contrast image of an ant abdomen.

to visualize the transient structure of supersonic diesel fuel sprays generated by high-pressure injection (MacPhee et al., 2002). The generated images allow quantitative analysis of the thermodynamic properties of the shock waves, which had proved to be impossible with optical imaging.

The experimental setup uses a high-pressure common-rail diesel injection system, typical of that in a passenger car, with a specially fabricated single-orifice nozzle. The orifice was 178 μm in diameter, and the injection pressure was selectable between 50 and 135 MPa. The fuel was injected into an x-ray-accessible spray chamber filled with an inert gas, sulfur hexafluoride (SF_6), at 1 atmospheric pressure and room temperature. The fuel used in this study was a blend of No. 2 diesel and a cerium-containing compound, with cerium concentration 4% by weight in the blend.

Two experimental arrangements were used. In the first, carried out at the APS 1-BM beamline, the injection apparatus was scanned through a small, focused x-ray beam. The transmitted beam was recorded using an avalanche photodiode (APD), which served as a fast point detector. At the D-1 beamline of CHESS, a wide bandpass (1%), extended size beam was used in conjunction with a fast pixel array detector (PAD). (The PAD detector was developed by Sol Gruner's group at CHESS.)

The combination of high-intensity x-rays from a synchrotron and the PAD allowed us to image the shock waves during the injection process. Figure 1.2 shows images of the fuel spray jet with the fuel injection pressure was set to 135 MPa. The leading edge of the fuel spray jet reaches 345 m/s and exceeds the sonic speed. The shock-wave front (the so-called Mach cone)

emanates from the leading edge of the fuel jet soon after emergence from the nozzle. Measurement of the Mach cone angles gives values that agree with the leading edge speed.

We also derived the mass density distribution of gas medium near and inside the Mach cone. In the plane perpendicular to the jet axis, the shocked region is a cone with an excess density in the SF_6 of 0.6 μg/mm^3 measured 10.4 mm from the spray tip. Behind the high-density region, the interior of the cone has a small but observable reduction in the gas density from the ambient, which implies that decompression has occurred away from the Mach cone.

This study has paved the way to directly study the complete range of fluid dynamics inside and close to high-pressure liquid sprays. The time-resolved, radiographic method should also prove useful in characterizing highly transient phenomena of, and in, optically dense materials, such as dense plasma and complex fluid-gas interactions.
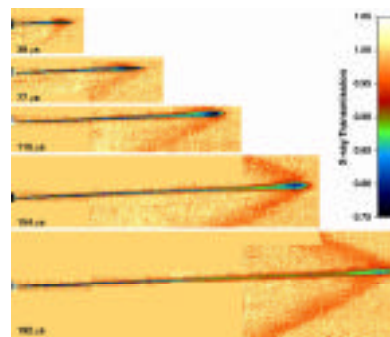
Fig. 1.2. Time-resolved radiographic images of fuel sprays and the shock waves generated by the sprays for time instances of 38, 77, 115, 154 and 192 μs after the start of the injection (selected from the total of 168 frames taken).

1.2.3 Crystal Diffraction Medical Imaging Lens

The first full-scale crystal-diffraction medical-imaging lens has been completed and tested. The lens consists of 13 concentric rings of copper single crystals aligned in such a manner that they all focus gamma rays or x-rays coming from a small source onto a small detector. The lens is capable of focusing x-rays and gamma rays with energies between 80 keV and 250 keV. The latest version of this imaging system is shown in Fig. 1.3. It is clear from this figure that the imaging system does not have to be close to the patient, eliminating any possible claustrophobia effect.
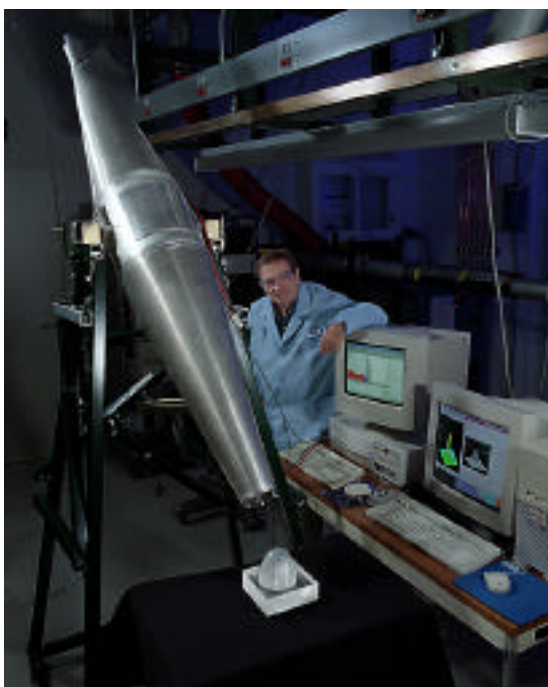
Fig. 1.3. The crystal diffraction medical-imaging lens system. The lens is located in the central cylinder section, the NaI detector is mounted at the upper end, and the breast phantom (with a small radioactive sample located inside) is shown below the end of the imaging system.

Tests of the imaging lens system were performed with energies of 121 keV (^{57}Co) and 141 keV (^{99}Tc), the latter being the most common source in medical imaging. Recent x-ray optics developments have reduced the spatial resolution to 3 mm FWHM (for a 1-mm-diameter source). This resolution is a factor of three better than most of the imaging systems in use today and is as good (and in most cases better) than the PET scanning instruments that are currently being developed.

The crystal-lens imaging system can be applied to small animals (e.g., rabbits, rats, or mice) that are used by the pharmaceutical industry for testing of newly developed drugs. It can also be used to image small parts of the human body such as blood vessels. Based on the data obtained with this lens, we are considering lenses with still better resolution, possibly as small as 1 mm FWHM. This resolution would allow the detection of very small tumors in places such as the female breast or in small test animals. There are many possibilities for nonmedical applications of such a lens system, including the examination of nuclear fuel elements and the location of radioactive material within a larger mass.

1.3   Time-Resolved X-ray Techniques Development

The time-resolved x-ray program can be divided into three parts: radiographic studies of fuel sprays, *in situ* measurements of nanoparticles in polymer-film systems, and x-ray streak camera development. Breakthroughs have been made in each of these areas during the time period covered by this report.

1.3.1 Real-Time Diffusion Dynamics of Polymer/Metal Nanocomposites Using X-ray Standing Waves

Polymer/metal nanocomposites have emerged in recent years as an important research area due to their practical and fundamental significance. Fundamental questions can be addressed by studying individual particle interactions with homopolymers (Shull & Kellock, 1995). In this study, we probed the polymer/metal interactions using a model nanocomposite system. The diffusion of the gold nanoparticles in polymeric thin films was measured in real time as the nanocomposite is annealed above the glass transition temperature (T_g). Total external reflection x-ray standing waves (TER-XSWs) were used to determine the profile of the metal particles perpendicular to the polymer surfaces during slow diffusion dynamics.

Float glass substrates were first placed in a thermal evaporation system and coated with a silver mirror. Poly(tert-butyl acrylate) (PtBA), MW = 352,000 g/mol, thin films (400 Å) were then spun cast from a butanol solution (Cole et al., 1999). The samples were then placed back in the evaporation system, where a thin layer of gold was deposited on the polymer films. The 4 Å gold layer was then sandwiched by another thin polymer film (400 Å) floated from a water bath. X-ray standing wave (XSW) experiments were performed at the 1-BM beamline under a helium environment. The x-rays were monochromatized to an energy of 12.1 keV, optimized for promoting Au L fluorescence.

Previously, the XSW method was used to locate a heavy atom marker layer in thin films with angstrom spatial resolution above a mirror surface (Bedzyk et al., 1989; Wang et al., 1991). The spatial distribution of the gold marker can be obtained by fitting the fluorescence profile as a function of incident angle with a realistic model (Parratt, 1954). The reflectivity and fluorescence experimental data at room temperature along with the fits are shown in Fig. 1.4. The reflectivity and fluorescence data were fitted up to the critical angle of the silver mirror, which is 5.08 mrad, as seen by the sharp decrease in the reflectivity.

The fluorescence yield is a convolution of the electric field intensity and the spatial distribution. In the current work, a Gaussian distribution was assumed with two fitting parameters: the half-width half-max (HWHM) of the distribution and its mean position above the mirror surface. The fit in Fig. 1.4b shows that the gold layer has a HWHM of 16 Å and is situated 366 Å above the mirror surface.

The samples were then annealed above T_g (= 49°C) to allow the gold nanoparticles to diffuse. The fluorescence profile taken after 180 minutes at 85°C is shown in Fig. 1.4c. The fit to the fluorescence profile shows significant broadening (HWHM = 40 Å) of the gold distribution, as well as movement of the mean position towards the air/film interface. This is partially attributed to the asymmetric nature of the mobility of the polymer films, since the silver substrate layer limits motion of the bottom PtBA chains. The HWHM values collected in real time during the anneal were used to determine effective diffusion coefficients that are on the order of 10^{-18} cm^2/s, showing the sensitivity of TER-XSWs to small diffusion distances.

1.3.2 Crystal Optics Simulations for X-ray Free-Electron Laser Pulses

Perfect crystal optics are expected to continue to be important for mono-

chromatizing and manipulating x-ray beams at fourth-generation x-ray sources. Given this, examining the fundamental physics of perfect-crystal diffraction (i.e., dynamical diffraction theory) in the regime of ultrashort (femtosecond) pulses is worthwhile. In this regime, the pulse lengths are comparable to or shorter than the extinction length scales of the crystal reflection. We have developed computer programs to calculate the diffraction properties under ultrashort pulses, initially without consideration of damage due to the high peak fields. Initial work consisted of computation of the Green's functions corresponding to crystal-reflection responses to incident -function electromagnetic impulses in Bragg and Laue geometries, for both reflected and transmitted beams. In addition to demonstrating quantitatively how crystal reflections respond to impulses, these

simulations pointed out the effect of delayed echos from back-face diffraction in thin Bragg crystals. (A similar effect exists for Laue crystals.) The studies were taken further to examine the modification of a self-amplified spontaneous emission (SASE) x-ray free-electron laser (XFEL) pulse's temporal structure through single- and double-crystal reflections of low and high orders. In addition to simulating the degree of smearing of an incident pulse's microbunching structure, the shot-to-shot time-integrated intensity fluctuations were examined (Fig. 1.5).

Attention has also been directed towards understanding the high-field-induced nonlinear corrections to the elastic-scattering cross section. This was deemed important in light of the possible necessity of modification of the electronic susceptibility for a dynamical diffraction theory valid at high x-ray intensities. Also motivating this issue is the frequently contemplated future technique of single-shot (or few-shot) diffraction studies of materials with focused XFEL beams. It is reasonable to ask whether, at such high intensities, the scattering intensities have the same quantitative interpretation (in connection to electronic structure) as in conventional x-ray scattering. To examine this, the next order perturbative correction to the usual (linear) scattering factor for x-rays was estimated to be 5 orders of magnitude weaker than the Thomson cross section.

1.4 High-Energy X-ray Scattering

The high-energy x-ray program is heavily involved in the development of instrumentation and techniques that will be used on a dedicated high-energy beamline at the APS (the former HEX-CAT project).
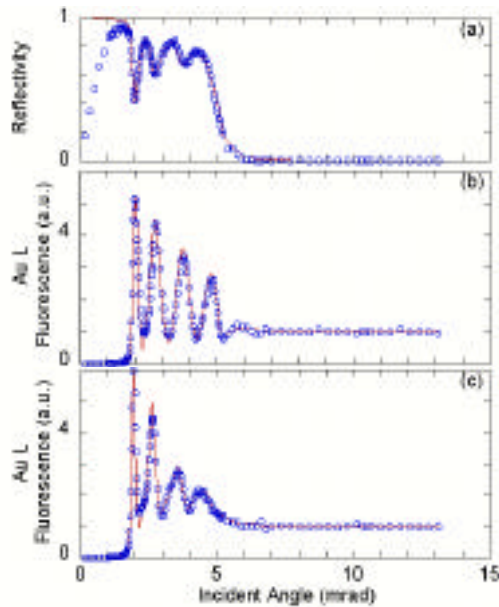
Fig. 1.4. Experimental data (circles) and fits (lines) at room temperature for (a) reflectivity and (b) fluorescence. The fluorescence profile after the sample has been annealed at 85°C for 180 minutes is shown in (c).

Part of this effort is to develop the user base for high-energy x-rays from the existing community of x-ray and neutron users. High-energy x-rays are being to a variety of scientific areas, but the largest use is now coming from applied materials science, in particular in the area of stress, strain, and texture measurements. The developments in high-energy small-angle scattering are unique and give a valuable new tool for examination of a variety of materials.

1.4.1 Development of a High-Energy SAXS Camera at Beamline 1-ID

High-energy small-angle x-ray scattering (SAXS) at second- and third-generation synchrotron sources has been demonstrated (Siddons et al., 1990; Bosecke & Diet, 1997), based primarily on Bonse-Hart geometries. Our aim is to develop a high-energy (HE)-SAXS camera for beamline 1-ID based on an in-line geometry. The camera allows for collection of anisotropic SAXS information, with good spatial resolution and is compatible with other high-energy techniques under development at sector 1 (e.g., wide-angle x-ray scattering (WAXS) and phase-contrast imaging).

Unlike Bonse-Hart SAXS cameras, the in-line camera allows for fast data acquisition and makes possible time-resolved studies, as
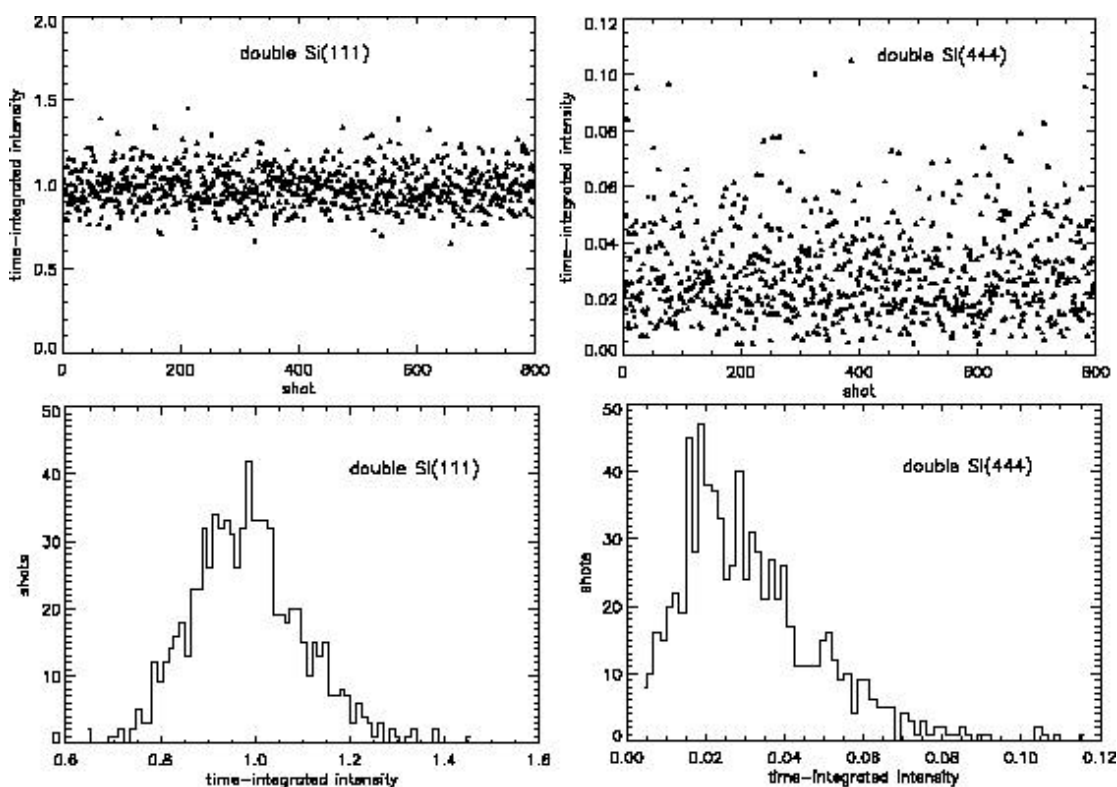
Fig. 1.5. Integrated intensity statistics of shot-to-shot fluctuations calculated after double Si(111) and Si(444) monochromators placed in an 8 keV SASE beam from the Linac Coherent Light Source (LCLS).

demonstrated for lower energy x-rays (Bras & Ryan, 1997).

Here we briefly outline instrumentation and data treatment and demonstrate the technique with spatially resolved measurements on thermal-barrier coatings grown by electron-beam phase vapor deposition (EB-PVD). This work was done in collaboration with a group from UNI-CAT/NIST. Many of the relevant properties of these coatings, including the elastic modulus and thermal conductivity, are related to the coating porosity and microcracking, which are in turn dependent on the deposition process parameters. Previous small-angle scattering (SAS) measurements on these coatings, using neutrons and lower energy x-rays (Allen et al., 2001) have revealed strong anisotropic SAS patterns related to orientation-dependent inhomogeneities. However since the beam size in those studies was on the order of the coating thickness (~800 μm), no information on any gradients in the sample was obtained.

An 80.72 keV beam from the high-energy monochromator was reduced to 100×20 μm^2 using 2-mm-thick W slits. Additional guard slits were placed ~1 m downstream to minimize background arising from parasitic scattering. Direct beam intensity and sample transmission were monitored with an ion chamber and PIN diode placed just upstream and downstream of the sample position, respectively, and the incident flux was measured to be ~3×10^9 ph/sec. The samples were cut into 0.5-mm-thick cross sections and measured in transmission geometry. The 2D SAXS intensity was recorded with a Bruker CCD detector located 4.9 m from the sample.

Figure 1.6 shows the sample transmission as a function of thickness. Within the coating, the transmission increases towards the top of

the coating due to an increase in porosity. Quantification of this porosity, by accounting for sample thickness and theoretical absorption factors, shows values ranging from 10-20% (Kulkarni et al., unpublished). Two-dimensional SAXS patterns are presented for four beam locations in Fig. 1.7. The SAXS patterns display marked anisotropies, as expected from the directional nature of deposition process and resulting porosity. Furthermore, differences in SAXS patterns are clearly visible as a function of position. Near the interface, the patterns show two maxima as a function of , while, further up in the coating, additional maxima are present.

Complementary microscopy studies reveal that these SAXS patterns are caused by a hierarchy of nm-sized porosity formed during deposition. These range from inter-columnar pores near the interface (SEM image in Fig. 1.7) to oriented intracolumnar pores and feathery cracks (as seen by TEM, Kulkarni et al., unpublished) further up in the coating.
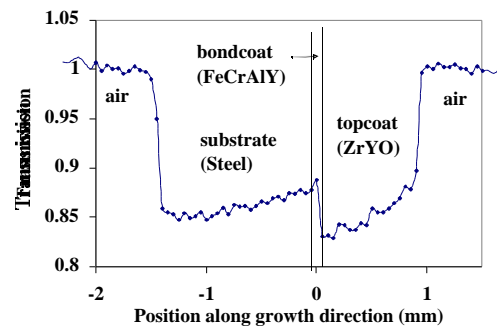

Fig. 1.6. Transmission across various layers of the thermal-barrier coating system. Spatial resolution (25 μm) is twice the spacing between points.
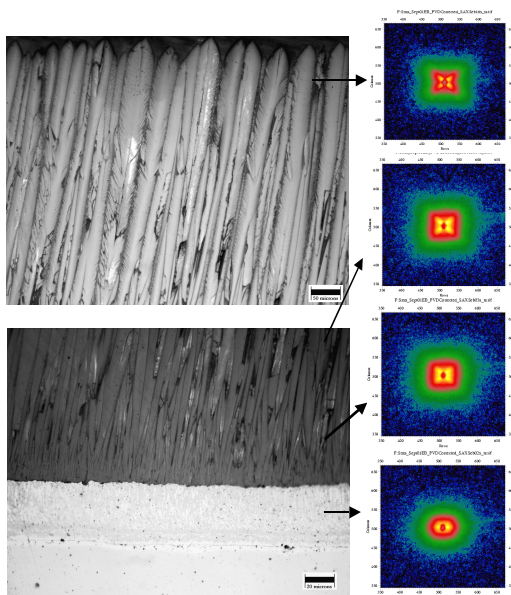
Fig. 1.7. Scanning electron microscope (SEM) images near the surface (top left) and interface (bottom left) of the TBC system, with corresponding HE-SAXS images (right).

1.4.2 Stress/Strain and Texture Measurements in Polycrystalline Materials

Most structural and functional materials are polycrystalline and understanding their bulk behavior is critical. Important structural parameters are the local stress/strain and texture. Applied materials are often hetero-geneous with performance governed by structural gradients on the size of grains (often between 1-100 µm). To validate the various mesoscale models that are proposed, experimental data are necessary that are averaged over a statistical ensemble of grains but still resolve the macrogradients. Currently, such data are essentially nonexistent due to the lack of suitable experimental techniques.

High-energy x-rays are a powerful tool to gather such data. The combined penetration

power, ample flux, and small focal sizes (down to 1 µm) offer unique experimental capabilities. Furthermore, 2-D detectors provide parallel, and therefore fast, data acquisition, opening up opportunities with *in situ* measurements. Efforts of the SRI-CAT high-energy program are illustrated by the following example.

Fiber fracture in metal-matrix composites often initiates damage zones that grow until the composite fails. To better understand the evolution of such damage from a micromechanics point of view, a model Ti-matrix/SiC-fiber composite was studied. The transfer of load from a broken fiber to the rest of a fiber-reinforced composite is one of the fundamental micromechanical processes determining strength. In order to predict strength, one needs to understand the details of this load transfer.

Using high-energy x-rays and a small sampling volume, the damage zone around a broken fiber was investigated (in collaboration with a group from California Institute of Technology). The studied composite system consists of a single row of unidirectional SiC fibers (SCS-6, 140 µm diameter) in a Ti-6Al-4V matrix, prepared by a proprietary technique at 3M Corp. A small region of the matrix was removed via acid etching to expose the SiC fibers. One fiber was intentionally broken in the exposed region, with the matrix left intact around and behind the exposed region.

The strain in the fibers and matrix was monitored using a $90{\times}90~\mu m^2$ beam while applying a tensile stress to the sample. Results of the strains within the broken fibers are shown in Fig. 1.8. The data were compared to a modified shear lag model that considers the elastic response of the matrix and the fibers. A comparison of the model
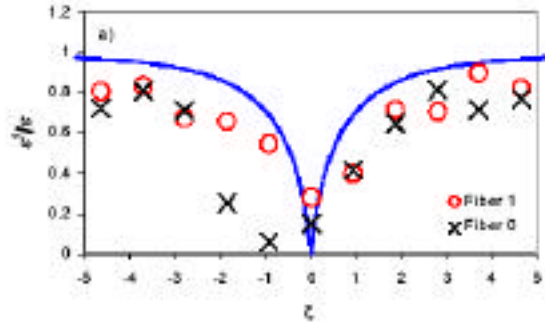
Fig. 1.8. Comparison of strains from model predictions (designated by lines) and XRD data from fibers (symbols). The applied stress was about 420 MPa. Strains were normalized with respect to the applied far field value. The dimensionless length describes the distance along the fibers from the crack.

and data shows a correlation on the trend of the data, but there are significant discrepancies. Results indicate the need for further refinements of the model, incorporating factors such as residual stress and matrix plasticity.

1.4.3 Resonant Powder Diffraction Studies of Gallium Distribution in the Type-I Clathrates

There has been considerable recent interest in the development of a new generation of more efficient materials for thermoelectric cooling. In order to achieve high efficiency, thermoelectric materials must simultaneously display reasonable electronic conductivity and very low thermal conductivity. The type-I clathrates $Sr_8Ga_{16}Ge_{30}$ and $Sr_4Eu_4Ga_{16}Ge_{30}$ display glass-like thermal conductivities along with relatively good charge carrier mobility making them good candidates for thermoelectric applications.

The static disorder associated with the presence of both gallium and germanium in the framework has a significant effect on the electrical properties of these materials. In collaboration with a group from Georgia Institute of Technology and the University of South Florida, we used resonant powder diffraction to investigate the gallium distribution in the type-I clathrates $Sr_8Ga_{16}Ge_{30}$ and $Sr_4Eu_4Ga_{16}Ge_{30}$. The analysis indicates a pronounced preference for the occupation of the 6c site by gallium (Fig. 1.9).
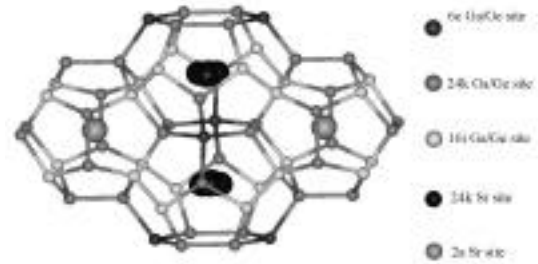
Fig. 1.9. Three crystallographically distinct sites exist in the framework of type-I clathrates, 6c, 16i, and 24k. There is static disorder of gallium/germanium over these sites.

1.4.4 High-Energy X-ray Optics: Achieving Higher Energy Resolution with Compound Refractive Lenses and Crystals

A liquid-nitrogen-cooled monochromator for high-energy x-rays (50-300 keV) consisting of two bent Si(111) Laue crystals adjusted to sequential Rowland conditions (Fig. 1.10) has been in operation for over two years at the 1-ID beamline. It delivers over ten times more flux than does a flat crystal monochromator at high energies, without any increase in energy width (E/E = 10^{-3}). Cryogenic cooling permits optimal flux, avoiding a sacrifice from the often-employed alternative technique of white-beam filtration. The fixed offset geometry

provides a fully tunable, in-line mono-chromatic beam.

Although 10^{-3} energy resolution in the 50-100 keV range is sufficient for most high-energy experiments presently conducted at the 1-ID beamline (e.g., pair-distribution function measure-ments, fluorescence spectroscopy, powder diffraction, and stress/texture deter-mination), it is sometimes desirable to have a narrower energy bandpass. Improved energy resolution ($E/E = 10^{-4}$ or better) would benefit high-resolution powder diffraction, line-shape analysis in stress/strain measurements, anomalous scattering from heavy elements, excitation of nuclear resonances, Compton profile studies, and high-resolution spectroscopy for inner shell atomic physics.

One approach to narrowing the energy resolution to 10^{-4} levels or better is by maintaining the current concept but with modified Laue crystal parameters of thickness, asymmetry, and reflection order.
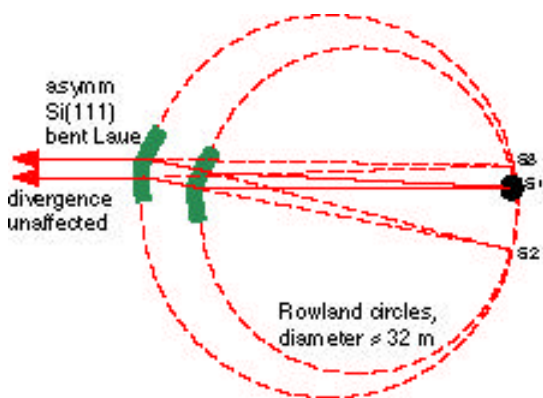
Fig. 1.10. Tunable, in-line high-energy x-ray monochromator composed of two vertically diffracting, bent Laue crystals located at about 32 m from the undulator source (S1).

However, higher resolutions at high x-ray energies demand excellent stability, which is difficult to achieve at the heat loads delivered by the white beam. So, attaining energy resolutions better than 10^{-4} is best done using additional postmono-chromatization optics after the existing broader bandwidth double-Laue system. This approach keeps the white beam optics invariant (and relatively simple), while permitting the subsequent high-resolution system to operate without significant thermal loads.

The post-monochromatization optics developed at 1-ID (Fig. 1.11) uses a compound refractive lens (CRL) to collimate (i.e., eliminate the angular divergence of) the beam from the double-Laue system. The resultant beam is better matched to the acceptance of the small angular width of the high-resolution, 4-reflection flat-crystal optics. The effective-ness of such a method is greatly enhanced by a pre-monochromator that is brilliance preserving—a feature inherent in the bent double-Laue system, but not, for example, in double mosaic-crystal monochromators, which are commonly used for high-energy x-rays. The performance of such an arrangement, as depicted in Fig. 1.11, is described here for an energy of 81 keV. The bent double-Laue pre-monochromator delivers 3×10^{12} ph/s in a 1×1 mm^2 beam of energy width $E/E = 1.5 \times 10^{-3}$ and a vertical divergence of 29 microrad. The beam then passes through an aluminum CRL consisting of 87 cylindrical holes of 1 mm diameter, separated by 50 micron walls. These parameters give the device a 35 m focal length for 81 keV radiation, resulting in the desired collimating action, as it is placed 35 m from the undulator source.
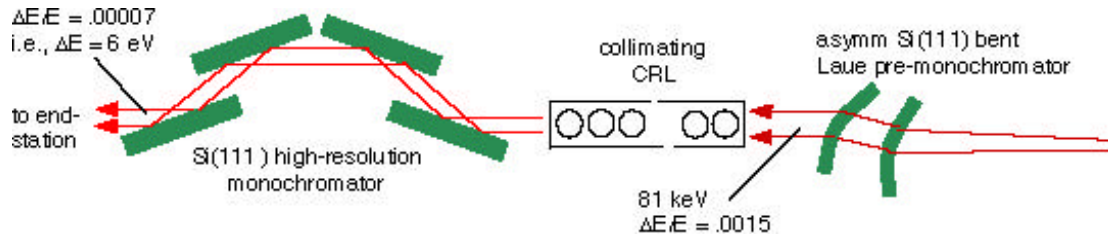
Fig. 1.11. High-resolution setup consisting of the bent Laue pre-monochromator, collimating lens, and 4-reflection flat crystal optics.

The collimated beam then Bragg reflects through four symmetric Si (111) crystals in a (+--+) configuration implemented by two dispersive channel-cut crystals. At 81 keV, a symmetric Si(111) Bragg crystal has energy and angular Darwin width acceptances of 1.4×10^{-4} and 3.5 microrad, respectively. So, ideally, one would expect this setup to monochromatize the beam to E/E = 1.4×10^{-4} with a flux loss (relative to the pre-monochromator output) of a factor of about 20. The flux loss is from a one order of magnitude improvement in mono-chromaticity with a 50% absorption loss through the CRL. In the experiment, a flux loss factor of about 50 was measured, a factor of 2 worse than expected. This is attributed to imperfect CRL collimation due to cylindrical aberrations. However, it turns out that this imperfect collimation also results in the final energy resolution being twice better than expected, i.e., 7×10^{-5} instead of 1.4×10^{-4}. So the final 81 keV beam intensity is 6×10^{10} ph/s in a 1×0.5 mm size (horiz. × vert.), with 6 eV energy resolution.

To test focusing with CRLs at high energies, an aluminum CRL similar to the one described above, but with 212 holes, was used to vertically condense the 1×1 mm^2 beam from the bent Laue monochromator into the end station located 25 m beyond the CRL. This 1:0.7 distance ratio geometry produced a 1.7×0.089 mm^2 (horiz x vert) line focus with a CRL transmission of 27%. The 90 micron spot size is roughly twice that expected from the source size, with the discrepancy most likely again due to cylindrical aberrations in the CRL.

The elimination of cylindrical aberrations by using parabolic, as opposed to cylindrical, holes in the CRLs would improve performance in both the high-energy-resolution and focusing optics. A novel approach to fabricating one-dimensionally parabolic aluminum CRLs by an extrusion process is being developed and is described elsewhere in this report.

1.4.5 High-Energy X-ray Fluorescence: Minority Additives in Arc Lamp Plasmas

In principle, almost all elements can be identified by fluorescence lines below 25 keV, without the necessity for a very high energy incident x-ray beam. All K lines for the lighter elements and L lines for the heavier ones are available below this energy. However, detection of heavy elements by K-shell excitation can be attractive. The merits of the K-line fluorescence detection approach include (i) penetration capability of the radiation both entering and leaving a dense or contained sample, and (ii) simpler spectra, uncomplicated by the presence of

numerous overlapping peaks as often encountered when dealing with L-lines and standard solid-state detectors. K-holes also have higher radiative yields, but these advantages must be weighed against the backgrounds from strong Compton scattering processes (both simple and multiple) at high energies.

An example of the application of K-shell fluorescence spectroscopy is the study of minority additives in arc lamp plasmas.

Small quantities of heavy-element additives (e.g., Dy, Ce, I) can significantly alter the lighting properties (spectral color and efficiency) of Hg lamps. The gas under arc-discharge is contained in jackets of ceramic alumina and pyrex, amounting to many millimeters of thickness for incident and fluorescence x-rays to penetrate (Fig. 1.12).

By using 60-90 keV incident radiation and detecting K-fluorescence, wall absorption does not pose a problem, and the spatial distribution of the minority additives relative to the majority species (Hg) can be measured (Fig. 1.13).
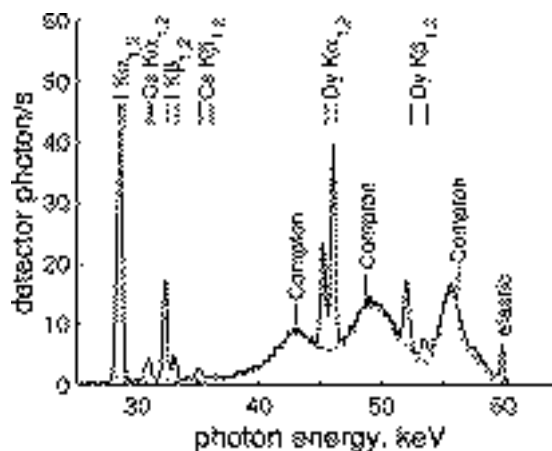
Fig. 1.13. X-ray-induced fluorescence spectrum of a 150 W ceramic metal-halide lamp with the lamp off (dotted line) and lamp on (solid line) showing characteristic fluorescence from Dy, I, and Cs, as well as Compton scattering from the lamp envelope, and elastic scattering from the envelope and Hg vapor.
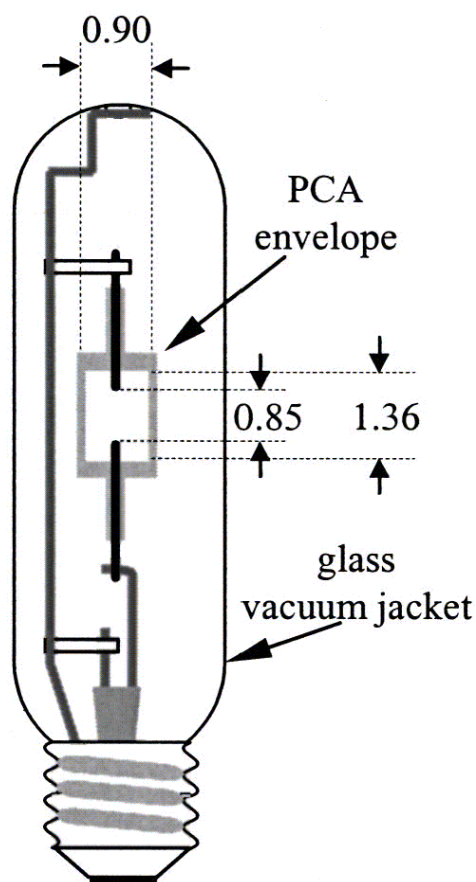

Fig. 1.12. The high-pressure arc lamp studied with x-ray-induced fluorescence consists of a ceramic alumina arc tube and a glass vacuum jacket. The arc tube is dosed with 16 mg Hg, 6.8 mg DyI_3, 1.2 mg CsI, and 12 Pa (90 Torr) Ar. (Dimensions are in mm.)

1.5 Search for X-ray-Induced Acceleration of the Decay of the 31-Yr Isomer of ^{178}Hf

Releasing the energy stored in an isomeric nuclear state in a controlled way with an atomic or electromagnetic trigger is an attractive speculation: the energy gain is on the order of the ratio of nuclear/atomic energies (i.e., MeV/keV). (Nuclear isomers are loosely defined as excited nuclear states with lifetimes longer than 10^{-9} s.) Nuclear isomers, therefore, represent an opportunity for a stand-alone energy source if suitable schemes for trigger and control of the energy release can be found. Potential applications include space drive, as well as very bright gamma-ray sources. The nucleus ^{178}Hf has a nuclear isomer with excitation energy of 2.447 Me. The 2.447 MeV isomeric state decays slowly (31 year half life) to the nearby state at 2.433 MeV. This J = 13^- state then loses energy in a rapid ($\sim 10^{-12}$ s) gamma-ray cascade ending at the 8^- rotational band head, which in turn decays via the ground-state rotational band cascade. The gamma-ray cascade is delayed at the 8^- state at 1.147 MeV, since the 8^- state is also isomeric, with a half-life of 4 s.

Reports of triggered decay of the ^{178}Hf isomer induced by x-rays delivered by a dental x-ray machine have been made (Collins et al., 1999). Enhancements amounting to 1-2% in the isomer decay rate had been reported for various gamma rays in the cascade. The reported integrated cross section for triggering the decay is 10^{-21} cm^2 keV, so large as to demand new physics. A collaboration involving LANL, LLNL, and ANL have sought to verify these reports taking advantage of the intense photon flux available at the APS beamline 1-ID, using white beam from a tapered undulator source. No induced decay was observed. The upper limits for the energy-integrated cross section

for such a process, over the range of x-ray energies 20-60 keV, are less than 2×10^{27} cm^2 keV, below the previously reported values by more than 5 orders of magnitude.

1.6 X-ray Microscopy and Microtomography

Since the last *Experimental Facilities Division/User Program Division Technical Progress Report* (ANL/APS/TB-38, 2000), the Micro-Techniques Group (now called the X-ray Microscopy Group) has continued to focus its efforts in the x-ray microscopy field. Application emphases were mainly in the biological/biomedical, environ-mental, and materials areas.

Novel x-ray microscopy experiments in the biomedical and environmental sciences continued to thrive. This was facilitated by operating two hard x-ray microprobes in parallel, with microfluorescence taking up ~40% operation of the 2-ID-D microprobe, and ~80% of the 2-ID-E side-branch microprobe. The high elemental sensitivity and spatial resolution of these instruments enabled trace elemental analyses in tissues, eukaryotic cells, and microorganisms at naturally occurring concentrations or at clinically relevant doses. Applications included studies of Pt- and Cu-derivative drug metabolism and Cr-induced carcinogenesis, metal contaminants in microbes at mineral surfaces and in marine and freshwater environments, metal distribution during cellular processes, and transfection of nanocomposites in cells. To explore these and future applications, we held a workshop on 14-15 May 2001, titled "Biological Applications of X-Ray Microbeams" (Lai et al., 2002). About 50 current and potential users attended. Other imaging modalities also flourished,

including microtomography optimized for high throughput, submicron-resolution phase tomography.

1.6.1 Transfection of TiO$_2$–Oligonucleotide Nanocomposites into Mammalian Cells

Nanotechnology can provide new capabilities for intracellular manipulation. For instance, hybrid complexes of TiO$_2$ nanoparticles and biopolymers can be used to remodel target DNA through the use of the photoelectrical properties of TiO$_2$ and the electrochemical properties and biological selectivity of the attached biopolymers. In particular, a polymerase chain reaction (PCR) with one oligonucleotide primer bound to TiO$_2$ nanoparticles shows (1) DNA bound to nanocomposite retains sequence-specific hybridization capability, (2) DNA-TiO$_2$ nanocomposites can participate in enzymatic reactions, and (3) illumination of nanocomposites causes breakage in the attached DNA within a short distance (few bp) from the nanoparticle. Thus the nanocomposites can be introduced into living cells, targeted to specific subcellular sites, and subsequently

used as platforms for initiation of intracellular processes.

A group led by G. Woloschak (ANL/BIO) and M. Thurnauer (ANL/CHM) introduced TiO$_2$ (4.3-nm-diameter) nanoparticles alone or in combination with "free" oligonucleotides into mammalian cells *in vitro*, using standard transfection methods. We mapped the location and quantity of Ti in the cells using scanning x-ray fluorescence microscopy at the 2-ID-D beamline (Figs. 1.14 and 1.15). Chi-square analysis of the data showed an association of transfection success and addition of free oligonucleotides to Ti nanocomposites during transfection. Further-more, free oligonucleotides that were identical to the ones bound to TiO$_2$ nanoparticles produced fewer cells displaying the Ti signal then those cells transfected with Ti nanocomposites and heterologous free oligonucleotides. This showed that nanocomposites can be introduced into cells using standard transfection methods and can then translocate into the cell nuclei. X-ray microfluorescence is crucial in quantifying the success rate of transfection and revealing the intracellular distribution of the nanocomposites.
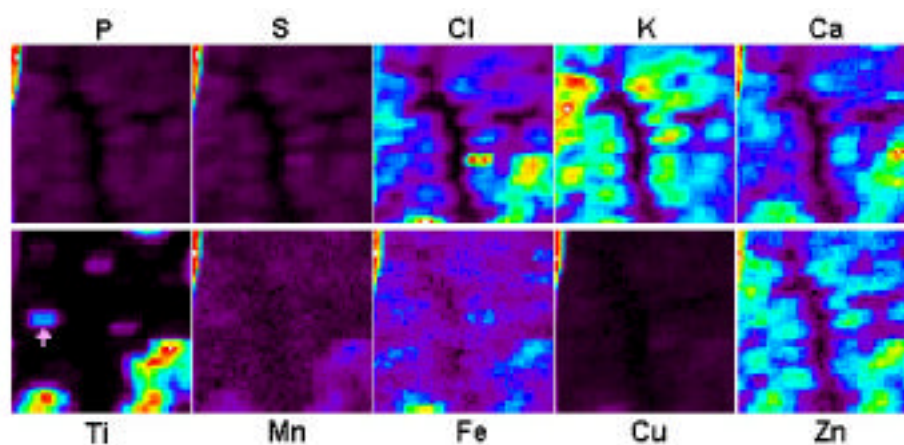
Fig. 1.14. X-ray fluorescence maps of several elements in a 90 μm × 90 μm area containing 28 HL60 cells transfected with TiO$_2$-oligonucleotide nanocomposites. The Ti map shows that seven cells contain Ti as a consequence of transfection.
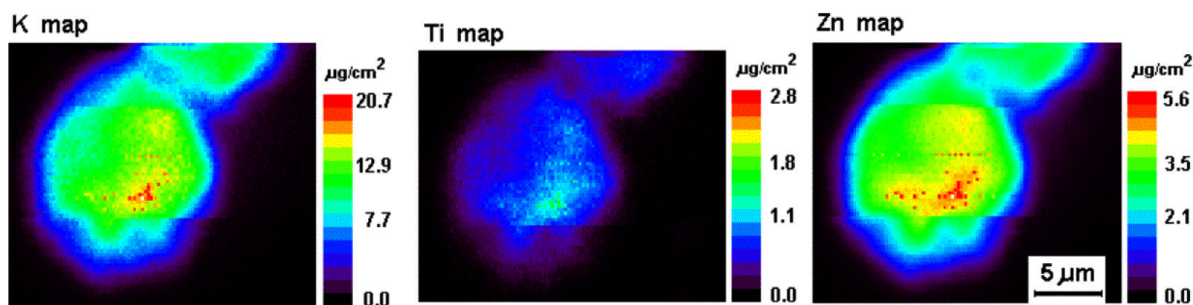
Fig. 1.15. High-resolution elemental maps of a 12 μm × 12 μm area of a single nucleus containing 3.6×10^6 nanoparticles. This nucleus was isolated from a whole cell transfected with R18Ss-TiO$_2$ nanocomposite and a free R18Ss oligonucleotide.

1.6.2 Trace Metal Contents of Individual Marine Protists

Over the past two years, B. Twining, S. Baines (SUNY-Stony Brook), and ourselves have used the 2-ID-E microprobe to map and quantify the trace elemental composition of single-celled microorganisms in the planktonic community. Accumulation of trace elements, such as Si, Fe, Cu, and Zn, by planktonic protists can influence the growth of primary producers (algae and phyto-plankton), elemental oceanic residence times, and metal bioaccumulation in aquatic food chains. Iron is of particular interest as it limits phytoplankton production in large oceanic regions. When Fe limits the growth of diatom cells, the cellular Si contents and thus sinking rates also change. Accumulation of Fe by protists thus influences the contribution of Fe-limited regions to oceanic C sequestration and global climate dynamics.
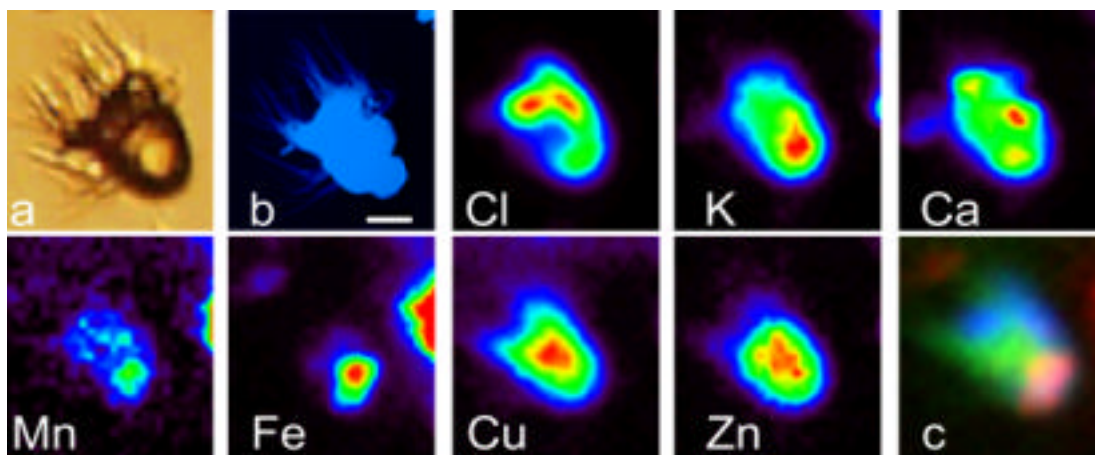
Fig. 1.16. Elemental maps of a marine ciliate (scale bar is 6 μm) collected off Southampton, NY. (a) Light micrograph. (b) Carbon content of the cell as measured by a scanning transmission x-ray microscope. Succeeding images (Cl, K, Ca, Mn, Fe, Cu, Zn) show elemental fluorescence uncorrected for background or spectral overlap. (c) Superposition of the Cl (blue), Fe (red), and Cu (green) images. Cl was chosen as a proxy for cellular biomass, while Fe and Cu trace metals show notably different spatial distributions within this cell.

In order to better understand the interactions between aquatic protists and both nutrient and contaminant trace metals, we have been measuring the elemental compositions of natural bacteria, algae, and their protozoan predators. Preliminary work using radioisotopes suggests that many metals do not absorb effectively onto bacteria and that protozoan predators are much more effective at concentrating certain trace metals from food than are metazoans. Microfluorescence studies (Fig. 1.16) allow us to determine if natural bacteria, photosynthetic algae, and nonphotosynthetic protozoa differ substantially in their trace-element concentrations and to predict more accurately the fate of trace metals incorporated into planktonic ecosystems. Cell-specific element analyses of phytoplankton will also allow us to determine the degree to which variability in algae species composition can affect the transfer of metals from the dissolved phase to higher organisms (e.g., fish). These data will greatly advance our knowledge of the factors that control the cycling of trace elements through food webs.

1.6.3 Quantitative 3D Submicron Phase Tomography

The significant increase in coherence obtained using third-generation synchrotrons, such as the APS, has driven major advances in phase imaging, which offers reduced radiation damage and the ability to observe object features with negligible absorption contrast. In recent years, research in this field has focused on development of accurate and rapid numerical methods (Paganin & Nugent, 1998) to extract the full complex refractive index of the object under study.

Previously, we demonstrated quantitative nanometer-scale two-dimensional (2D) x-ray phase microscopy at beamline 2-ID-B. We recently used the same optical system to perform tomographic phase imaging in three dimensions. In this experiment, a coherent 1.83 keV x-ray beam illuminated a sample consisting of a 9-μm-long commercial atomic force microscope (AFM) tip. A zone-plate lens magnified the object by 160 times onto an x-ray CCD camera, providing an image resolution of ~150 nm. To obtain the phase information, two defocused images were recorded on either side of the in-focus position by translating the zone plate along the optical axis. Two-dimensional projected phase maps were obtained from the defocus data after cropping and equilibration to compensate for beam intensity variations. This process was repeated at 1° intervals over a 180° angular range about the sample, then the phase data were aligned and reconstructed into three-dimensional (3D) images using the filtered back-projection method (Fig. 1.17). The resolution in these images is better than 900 nm, evidenced by the 6 pixel diameter of the spherical bump (a manufacturing defect) visible in Figs. 1.17b-f. The apparent faceted nature is typical of the manufacturing process used to etch crystalline AFM tips.
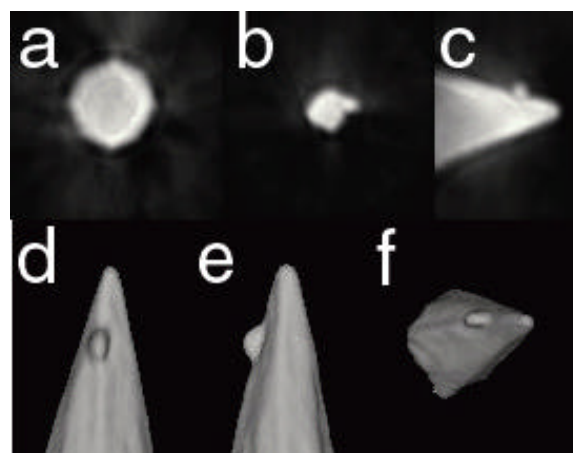

Fig. 1.17. Quantitative 3D reconstructions of the real part of the refractive index of the AFM tip. (a) Horizontal slice of the AFM tip. (b) A second slice including the spherical bump. (c) Vertical slice through the tomographic phase data. (d-f) Volume renderings of the AFM tip.

The reconstructed phase data yielded a measured refractive index decrement of $=(5.0\pm0.5)\times10^{-5}$. The calculated value of $=5.06\times10^{-5}$ at 1.83 keV, based upon the known composition of the AFM tip, is well within experimental error (McMahon et al., submitted).

1.6.4 Fast Tomography

Anatomical research in millimeter-scale organisms is notoriously time consuming. Because they may be too small to prepare directly and too large for, e.g., confocal microscopy, anatomical examination of such samples is traditionally done by preparation and analysis of histological sections, which are then reconstructed in 3D. Mechanical artifacts arising from the cutting process hinder fidelity and automation of the reconstruction, and a histological section series typically takes a week or more to acquire. In comparison, hundreds of specimens can be imaged in a typical run of 48-72 h using the fast microtomography system at beamline 2-BM. Using the ostracod *Scutigera coleoptrat* as a model sample, M. Fanenbruck (Ruhr U.) compared x-ray microtomography to conventional micro-anatomical methods. Unprocessed tomographic projections taken with 7.5 keV x-rays showed an impressive number of anatomical details, which would be invisible by light microscope. For example, some muscle bundles showed myostriation (Z-band distance of ~2.5 μm), confirming the spatial resolution was ~1 μm. By comparing the tomographic data (Fig. 1.18, left) to histological sections, we observed that almost all tissues were clearly discernible. Phase-contrast tomography or tissue-specific staining (e.g., with heavy-metal coupled antibodies) to enhance the contrast of soft tissues are promising future avenues.

Understanding biomineralization is essential to achieving controlled synthesis of complex biomimetic structures. Sea urchin ossicles are an important model because many aspects of echinoderm calcification resemble those in mammilian dental systems. For example, sea urchin teeth contain a wealth of structure evolved to enhance feeding efficiency. S. Stock (Northwestern U.) is using micro-tomography to study the strategies that sea urchins use to optimize biomechanical strength and toughness. In the sea urchin *(Lytechinius variegatus)* tooth fragment in Fig. 1.18 (right), the two rows of dark features are channels extending through the mineral. These features appear not to have been noted previously and may play an important role in nutrient or other transport within the tooth (Stock et al., submitted). Previous tomographic data revealed only faint bands from these rows, preventing correct interpretation of the structure.

Studies of new ceramic coatings developed at NIST, in collaboration with J. Ilavsky (SUNY/Stony Brook), seek to improve the efficiency and longevity of turbine engine components (Ilavsky et al., submitted). Electron-beam physical-vapor-deposited (EBPVD), yttria-stabilized zirconia (YSZ) thermal barrier coating deposits are used in turbine engines to protect intermetallic materials of turbine blades from hot gasses, resulting in an increased efficiency, reliability, and reduction of environmentally unfriendly gasses, such as NO_x. Figure 1.19 shows a fine columnar structure with small inter-columnar pores in the substrate of such a coating, while at top, the columns and voids are much larger. This structure was studied as function of deposition method and para-meters, as well as function of simulated in-service conditions (annealing). The speed of the 2-BM system has proven instrumental to obtain a good statistical base by analyzing a large number of samples.
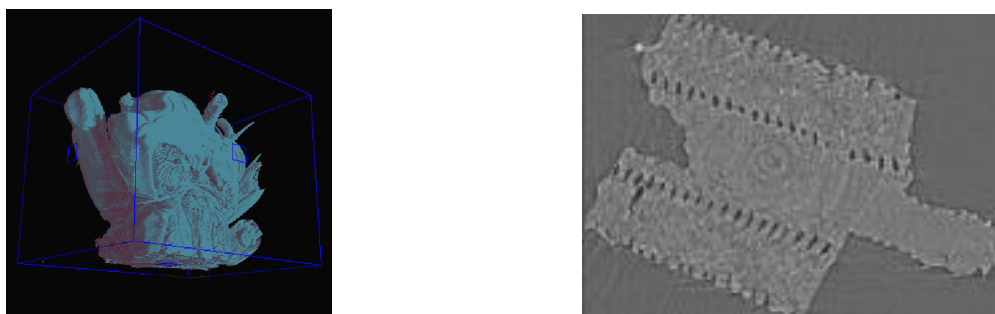
Fig. 1.18. Left: 3D visualization of the ostracod data with gray-scale segmentation of cuticle (cyan) and soft tissues (red). Right: Reconstructed slice of a sea urchin tooth fragment.
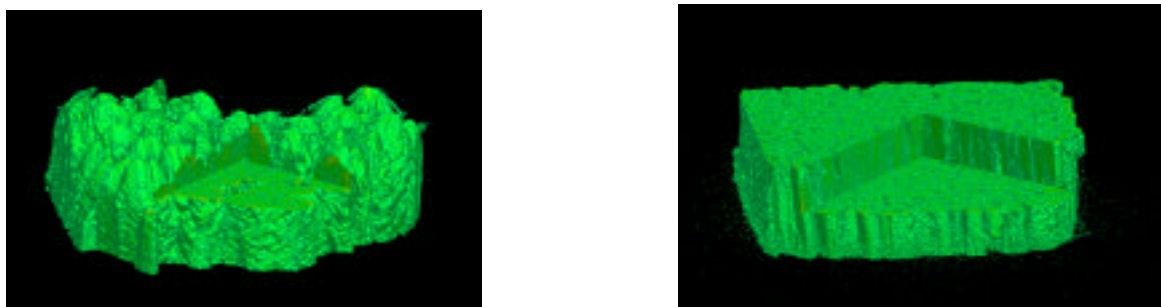
Fig. 1.19. Reconstructed 3D images of EBPVD-YSZ thermal barrier coatings. Left: Image showing structure at the top of the coating. Right: Image showing the structure of the same deposit at the substrate.

1.7 Diffraction and Coherent Scattering

Microdiffraction and coherent scattering methods that take advantage of high-resolution focusing optics and the APS brilliance are important components of the X-ray Microscopy Group user program. Recent highlights include diffraction imaging of antiferromagnetic domains, observation of columnar features in step-graded semiconductor films, combinatorial structure-property mapping of a binary alloy, phase-contrast imaging of defects in macro-molecular crystals, and measurement of x-ray speckle contrast shifts at absorption edges.

1.7.1 Microdiffraction Imaging of Antiferromagnetic Domains

Antiferromagnetic ordering refers either to existing interpenetrating sublattices of identical structure of local magnetic moments with opposite direction or to a zero total spin moment even though the spin density does not vanish. There have been few applications of antiferromagnets because the net magnetic moment is almost always zero at a practically accessible length scale and because they have been extremely difficult to image. We developed a new x-ray microdiffraction technique that makes it dramatically easier to map and analyze antiferromagnetic structure. We used it to reveal the broadening of the first-order "spin-flip" (SF) transition at 123 K in chromium, across which the spins rotate

by 90° at the walls between domains with orthogonal spin density wave (SDW) modulations (Evans et al., 2002).

Chromium is an antiferromagnet below the Néel transition at 311 K, in which the Coulomb interactions among electrons and the geometry of the Fermi surface conspire to produce incommensurate SDWs with modulation vectors that can lie along any of the three (001) axes of the unit cell. The SDW is accompanied by a lattice distortion and charge density wave (CDW) with a wave vector twice that of the SDW. In bulk Cr crystals, the orientation of spins relative to the wave vector of the SDW changes from transverse to longitudinal upon cooling through the SF transition. Combining nonresonant x-ray magnetic scattering with x-ray microdiffraction, we mapped the weak coupling between the long wavelength spin density modulation and the atomic-scale electron density modulation. A microfocused hard x-ray beam provided the high photon flux density necessary for weak magnetic scattering and the spatial resolution necessary for visualizing SDW domains. Figure 1.20 displays the SDW domains and their accompanying CDW domains in Cr at 130K. Figure 1.21 shows images of a single SDW domain at temperatures near the SF transition temperature. This first-order transition from transverse to longitudinal spin polarization results in the disappearance of magnetic scattering from the SDW domain due to the dependence of the scattering cross section on spin polarization. The SF transition begins at the boundary between SDW domains, revealing nucleation of a magnetic phase not at a structural grain boundary, as for the magnetic films, but at its magnetic equivalent. The interplay between macroscopically observable phenomena and the configuration of domains, both magnetic and ferroelectric, is increasingly important as density requirements in many technologies drive device feature sizes towards those of individual domains.

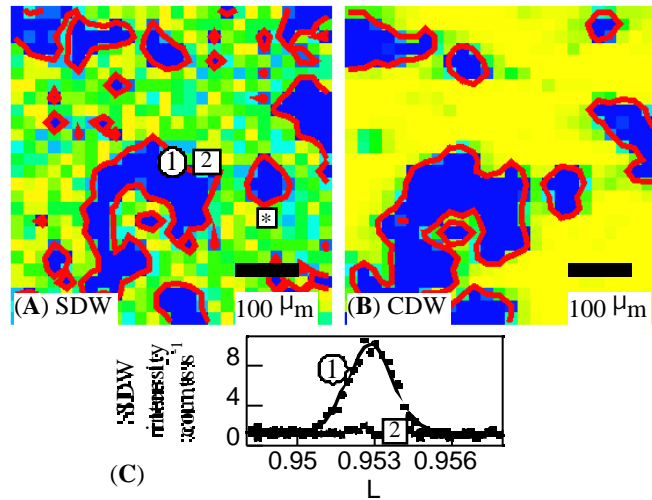

Fig. 1.20. Magnetic domains in Cr at T=130K. Intensity maps of the (A) SDW reflection and (B) CDW reflection from the same area of the Cr sample. (C) Reciprocal space scans at the positions indicated on the SDW map. The solid line is a Gaussian fit to the scan at position 1.
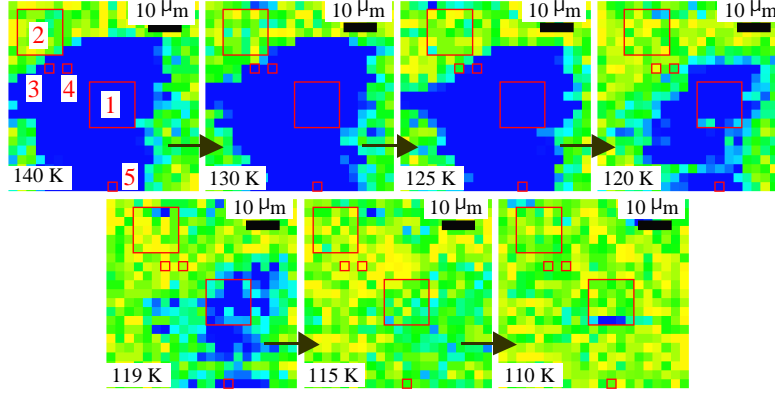
Fig. 1.21. Images of a single SDW domain at temperature near T_{SF}. This domain also appears at a different scale in Fig. 1 (marked with asterix).

1.7.2 Observation of Columnar Microstructure in Step-Graded $Si_{1-x}Ge_x$ /Si Films

$Si_{1-x}Ge_x$/Si(001) heterostructures are used in high-speed bipolar transistors in communications applications and have potential for high-speed field effect transistors (FETs). Electron microscopy studies have shown that epitaxial $Si_{1-x}Ge_x$ layers with x < 0.5 on Si(001) relax by the introduction of 60° misfit dislocations, with misfit segments running in perpendicular (110) directions parallel to the wafer surface and terminating in threading arms that run up to the wafer surface. Compositionally graded $Si_{1-x}Ge_x$ buffer layers have low-threading dislocation densities (typically 10^5-10^7 cm^{-2}) and are therefore useful for FETs. Strain-relaxed epitaxial films, such as $Si_{1-x}Ge_x$/Si(001), exhibit mosaic broadening originating from the misfit dislocations that relieve the strain. Although x-ray diffraction measurements on step-graded relaxed $Si_{1-x}Ge_x$ films have revealed local tilted regions having the same lattice parameter (d/d 5×10^{-4}) and a range of tilt angles up to ~0.25°, the lateral dimension of the tilted regions could only be roughly estimated (<20 µm) until now.

We used x-ray microdiffraction with an incident beam of size 0.25-2.7 µm and divergence of 0.004°-0.05° to investigate the structure of $Si_{1-x}Ge_x$ films. A CCD detector was employed to map diffraction intensities as functions of sample position or individual micrograins in the and 2 scattering plane. Rocking scans indicated a complex variety of shapes and wide range of tilt angles. All spectra showed a complex fine structure on the 0.01 - 0.02° scale. We solved the microstructure by comparing the results from films with low- and high-misfit dislocation densities and using an iterative fitting algorithm (Eastman et al., 2002). Rectangular columnar micrograins were found with average widths ranging from 0.6 - 3.7 µm. The vast majority are between 0.8 µm and 1.4 µm, extending from the misfit dislocation network near the SiGe/Si interface up to the wafer surface. The micrograins had similar lattice parameters (d/d 5 x 10^{-4}), but their (001) axes were tilted up to ~0.1° with respect to the (001) axes of the Si substrate. Measured diffuse scattering, about 10-20% of the diffracted intensity, suggested the existence of a nonuniform strained material near the boundary regions between the micrograins.

1.7.3 Phase Contrast X-ray Diffraction Imaging of Defects in Biological Macromolecular Crystals

The substantial decrease in source size and divergence offered by third-generation synchrotron facilities has enabled us to develop a new phase-contrast x-ray diffraction method for imaging defects in protein crystals (Hu et al., 2001). This coherence-based method is extremely sensitive to lattice irregularities compared to conventional x-ray topography. It provides a new way to characterize structural defects and the causes of lattice disorder over a wide spectrum of macromolecular crystal systems.

Figure 1.22 shows a phase-contrast x-ray diffraction image of a well-faceted and optically defect-free tetragonal hen egg-white lysozyme crystal taken at the (440) reflection at beamline 2-BM. Several defects are discernible. Dislocations D, dislocation loops (or half loops) L, and additional structural features exhibited greater contrast as the sample-to-camera distance was increased. Linear features originate from the growth

sector boundary (GB at the top-right corner in figure). A number of defects also emerge from the center of the crystal and originate from the initial nucleus. The dislocation segments are largely along the <001> and <110> directions, yet subtle osmotic pressure might play a role in the dislocation configuration given the intrinsic nature of weak macromolecular bonding. The loop-like dislocations are attributed to stress/strain relief around stress centers, e.g., caused by nonuniform trapping of impurities. This work illustrates that lattice defects and irregularities in weakly scattering protein crystals can be effectively mapped by simply incorporating phase information of exit x-ray waves into diffraction imaging.

1.7.4 Continuous Structure-Property Mapping of Combinatorially Synthesized $Fe_{1-x}Ni_x$ Binary Alloys

Mapping of complex structural and physical property relationships as functions of material composition is traditionally accomplished through synthesis and analysis of samples with discrete compositions, prepared one at a
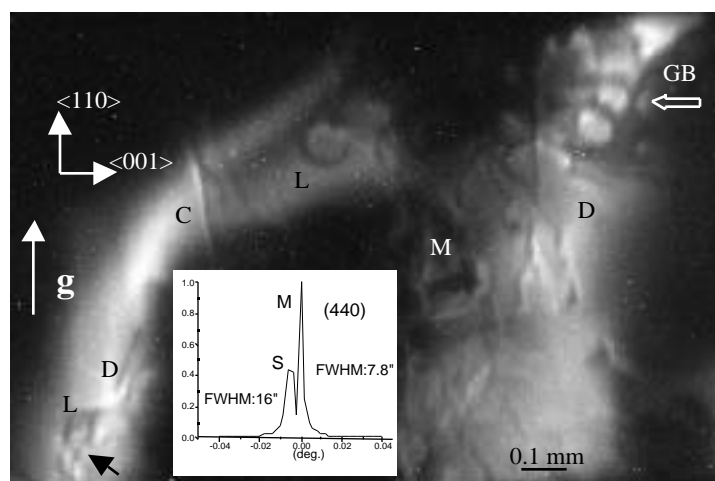

Fig. 1.22. Phase-contrast diffraction image of a hen egg-white lysozyme crystal; inset shows rocking curve. White regions diffract strongly. (g) Diffraction vector, (GB) growth sector boundary, (C) microcracks, (D) dislocation defect, (L) dislocation loop or half-loop.

time. This slow process limits detailed mapping, without which one may miss important opportunities in material discovery. At 2-BM, we are developing x-ray diffraction and fluorescence techniques to rapidly analyze combinatorial phase libraries.

To start, we mapped the well-documented $Fe_{1-x}Ni_x$ binary alloy system using a single composition-spread sample (Fig. 1.23) with x changing linearly from zero to one (Yoo et al., 2001). Its crystal structure and composition were determined by x-ray diffraction and fluorescence using a 50 µm beam oriented along the composition-spread direction. The $Fe_{1-x}Ni_x$ alloy system exhibited two dominant crystal structures: a Fe-rich, -phase with a body-centered-cubic (BCC) structure and a Ni-rich, -phase with a face-centered-cubic (FCC) structure with a rather broad two-phase overlap from x = 0.12 to 0.2. While both structures are rotationally epitaxial, the -phase alloys from x = 0.2 to 0.7 exhibited particularly excellent specular texture with better than 0.1° rocking curve width, which

suggests greater crystalline ordering than the alloys with other compositions. As shown in Fig. 1.24, the lattice constants for both phases satisfactorily reproduce those obtained from discrete bulk alloys, with minor discrepancies. First, the -phase retains much greater stability extending below x = 0.2, which can be attributed to a lower interfacial energy of the FCC film on the hexagonal substrate. Second, the lattice constant for the -phase is consistently smaller than the bulk values with the most significant deviation over the $0.5 < x < 0.8$ region, which can be attributed to the large degrees of the residual strain in this region. The magnetic properties, measured by less than 200 µm, are also well correlated with the structures characterized by x-rays (see scanning Hall probe and scanning magneto-optical Kerr effect with a spatial resolution of Fig. 1.24). The $Fe_{1-x}Ni_x$ composition-spread sample exhibited good overall structural agreement with bulk Fe-Ni alloys, providing convincing evidence that the combinatorial synthesis can be efficiently used for structure-property mapping.
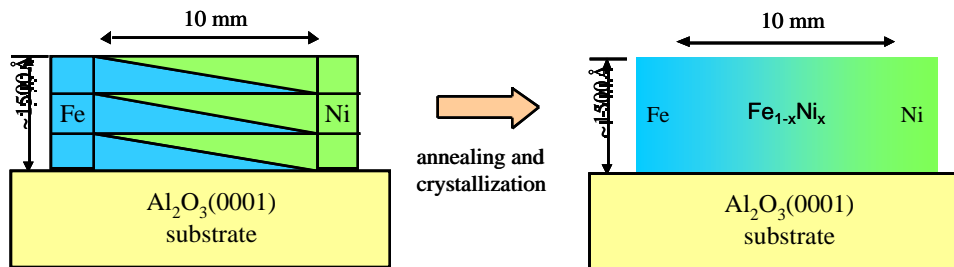
Fig. 1.23. Binary $Fe_{1-x}Ni_x$ composition-spread sample obtained by sputter-depositing thickness-gradient Fe/Ni multilayers at room temperature. As-grown multilayered films were annealed at 600°C for 3 h in evacuated ampoules, followed by air quenching, to obtain full compositional mixing normal to the film plane without oxidation and to achieve alloy phase formation.
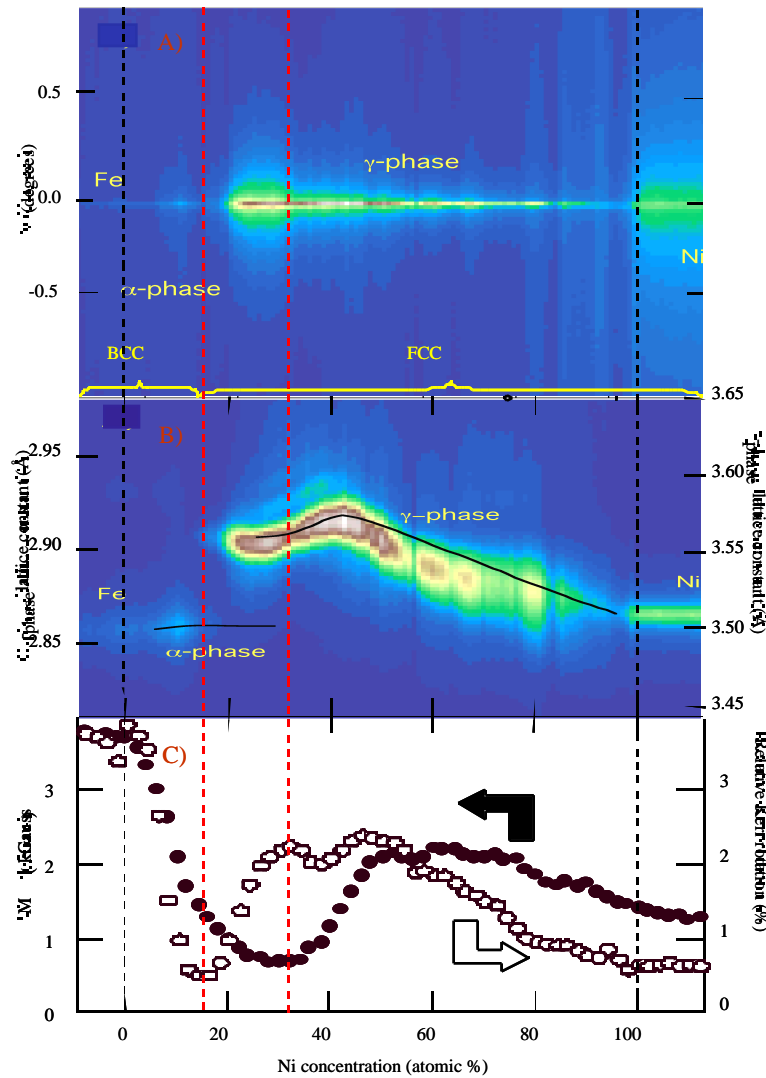
Fig. 1.24. (top) Structure-property map of the $Fe_{1-x}Ni_x$ sample. (middle) Specular texture of the composition-spread film obtained by   -rocking. The lattice constants were obtained from specular radial scans (bottom). Previously reported lattice constants obtained from discrete bulk alloys are shown as black lines for comparison. Red dashed lines show correlation of crystallographic structures with the magnetic properties. The regions below and above are the pure Fe and Ni phases, respectively.

1.7.5 X-ray Speckle Contrast Variation across Absorption Edges

X-ray speckle methods were introduced to the x-ray regime several years ago. At the 2-ID-B beamline, we are extending coherent scattering techniques, such as speckle, into the 1 to 4 keV range, which includes absorption edges in many important elements such as Al, Si, P, S, Zn, Ga, As, and the rare earths.

Coherent soft x-rays were recently used to probe the Gd M_5 (1190 eV) and Fe L_3 (707 eV) edges in resonant magnetic speckle experiments (Rahmim et al., 2002). Yet to our knowledge, the effect of absorption edges on x-ray speckle contrast has not yet been studied quantitatively. Standard speckle theory assumes that the energy dependence of the average intensity at a point in reciprocal space does not vary significantly over the

width of the spectral response function (Parry, 1984), and therefore does not predict any effect.

To test this, we recorded speckle data as a function of the incident x-ray energy across the Zn L_3 edge (1021 eV) in metallic zinc powder samples consisting of ~100 nm grains supported on 200-nm-thick silicon nitride membranes. The disordered powder samples were illuminated with a nearly (92%) coherent, 10-μm-diameter x-ray beam. We found by analyzing the intensity auto-correlation function of the data that the speckle contrast decreases as the absorption cross section increases at the edge (Fig. 1.25), indicating that standard speckle theory is indeed invalid near absorption edges (Retsch & McNulty, 2001). Speckle data taken across the K edge of a powdered aluminum sample (1560 eV) yielded comparable results. This effect has already been exploited to enhance speckle originating from a constituent element in a sample, e.g., to study ordering in anti-ferromagnetic domains. In addition to these
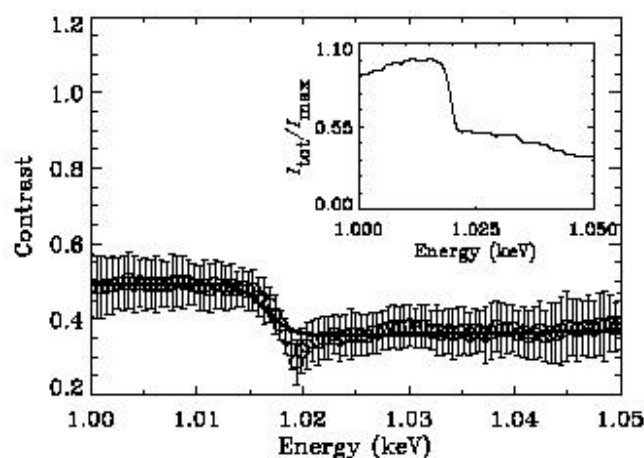
Fig. 1.25. X-ray speckle contrast versus energy in Zn powder (1.8-eV resolution), averaged over a small region of reciprocal space. The solid line shows a theoretical fit to the data points. Inset shows the total transmitted intensity measured directly

behind the sample, normalized by the beamline efficiency.

applications, edge-dependent contrast variations should be well understood if pre-, on-, and post-edge measurements are to be compared in coherent scattering experiments.

1.8 New Techniques and Instrumentation

Several technical enhancements supported our activities. We acquired a state-of-the-art visible fluorescence microscope and developed a precision kinematic sample holder that enables correlative visible and x-ray microscope studies as well as fast positioning of specimens with 1 μm accuracy. The 2-ID-E fluorescence microprobe was upgraded with a motorized table and curved rails allowing rapid and repeatable energy changes. We developed a compact, modular soft x-ray "nanoprobe" that permits rapid and reproducible optics alignment in the soft x-ray scanning microscope and diffractometer. Other key instrumentation developments included a quantitative x-ray beam coherence diagnostic, commissioning of the 2-BM broad-band double-multilayer monochroma-tor, a major upgrade of the fast microtomography system, integration of the hard x-ray microprobe with a six-circle diffractometer, and fabrication of high-aspect-ratio "lobster-eye" and antiscatter collimators by deep x-ray lithography.

1.8.1 Spatial Coherence Measurement

The dream of creating intense, highly coherent x-ray beams is fueled by the tantalization of new coherence-based x-ray experiments, as well as by existing techniques, such as scanning microscopy, interferometry, coherent scattering, and phase measurement. Thus there is strong motivation

to develop an efficient means to measure the spatial coherence of x-ray beams. We performed a Young's two-slit interference experiment in the soft x-ray region at the 2-ID-B beamline and used it to measure the dependence of the spatial coherence of the x-ray beam on the exit slit of the beamline monochromator. Narrowing the exit slit increases the degree of spatial coherence $|\mu_{12}|$ of the beam, which is directly related to the visibility of the interference fringes produced in a Young's experiment. The Young's slits were fabricated an array of seven slit pairs with 10–200 μm separation in gold. The interference patterns were measured with a scanning avalanche photodiode detector masked with a 5 μm slit. The fringe visibility decreased as the exit slit was widened and as the Young's slit separation was increased (Fig. 1.26), in keeping with expectation. The data showed the beam to have high coherence at Young's slit separations up to 100 μm, in good agreement with the predicted coherence profile (Paterson et al., 2001). A complete measurement of the coherence function requires determination of the degree of coherence over the full range of slit separations in the beam (a time-consuming experiment by the Young's method).

Developing a faster approach is the focus of continuing research.

1.8.2 The 2-BM Double-Multilayer Monochromator

We significantly enhanced the capabilities of the 2-BM beamline by incorporating a double-multilayer monochromator (DMM) into it (Chu et al., 2002). The first to be installed at the APS, the DMM was designed and constructed entirely in-house. Because multilayer optics typically have bandwidths ~100 times larger than crystal optics, methods that do not require a high degree of monochromaticity, such as x-ray tomography and fluorescence, benefit tremendously from the greater flux using a DMM. Figure 1.27 shows the DMM design and summarizes its two operating modes. In the normal mode, the DMM optics are inserted into the pink beam reflected by the M1 mirror at 2-BM. Four multilayer coatings allow continuous operation from 3.2-10.9 keV over a 1.35-1.90° incident angular range using the first-order reflection (Table 1.1). The coatings were deposited by DC magnetron sputtering on two 100 mm by 146 mm single-crystal
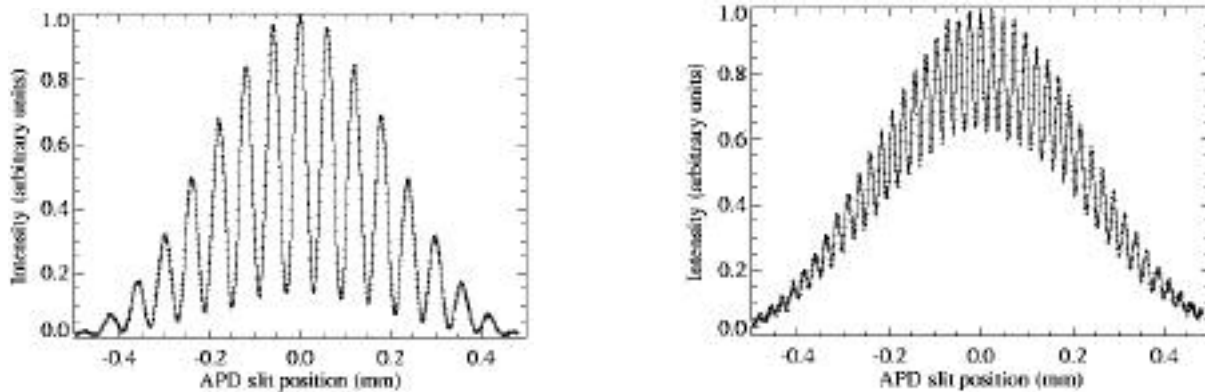
Fig. 1.26. Young's two-slit interference pattern recorded with 1.1 keV x-rays. The solid line is a theoretical fit to the data points. Young's slit separation of (a) 20 μm and (b) 50 μm.
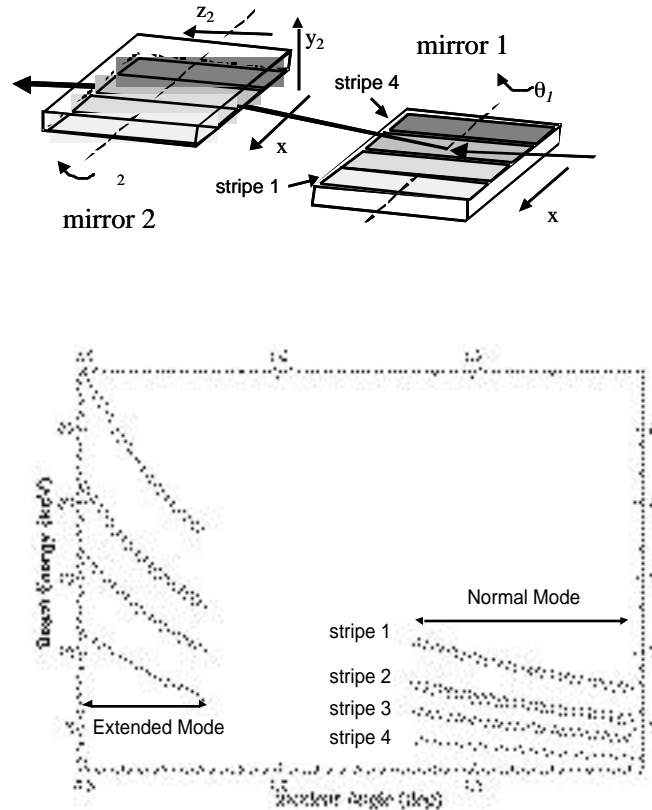
Fig. 1.27. (a) Schematic view of the DMM. Arrows indicate the allowed independent $_1$, $_2$, y_2, z_2 and coupled x motions. (b) The normal operating mode continuously covers 3.2 to 10.9 keV. The extended mode allows operation up to 28 keV using only stripe 2.

.

silicon substrates polished to 1 Å rms roughness and 0.4 µrad average slope error. All four coatings exhibit excellent reflectivity and minimal interfacial roughness and diffuseness (2-3 Å). In the normal operating mode, the DMM provides a fixed exit beam at the same position in the end-station as that from the 2-BM double-crystal mono-chromator (DCM). However, the DMM delivers 20-40 times more flux than the Si(111) DCM due to its greater bandpass. The DMM also operates in an extended mode at incidence angles of ~0.5-0.8°, giving access to a much wider energy range than originally intended. While the measured bandwidth is 3-4%, the practical flux gain at energies above 13.5 keV in this mode is much greater because the DCM can only reach these energies using the Si(333) reflection, which passes about 10 times lower flux than a Si(111) reflection.

1.8.3 Microtomography System Upgrade

During the last year, the 2-BM fast x-ray microtomography system underwent major upgrades, both in the instrumentation and in the parallel computer cluster used for data analysis (DeCarlo et al., 2002). The data

28

Table 1.1. Performance of the DMM optics.

Stripe	Multilayer structure	Measured reflectivity at 10 keV	Normal operating energy range	Reflectivity at operating energy range	Bandwidth at operating energy range
1	$[W(7.5) / Si(55.0)]_{35}$	78%	3.2-4.6 keV	~45%	~5%
2	$[W(9.7) / C(14.8)]_{100}$	65%	8.0-10.9 keV	~65%	~1.5%
3	$[W(14.2) / C(19.5)]_{50}$	82%	6.1-8.1 keV	~75%	~5.5%
4	$[W(6.8) / Si(36.0)]_{60}$	83%	4.6-6.4 keV	~65%	~4%

acquisition and analysis systems were completely automated. Both the sample and CCD camera staging were redesigned. We now have a more precise and compact system that allows users to mount and align samples in a few minutes. A newly designed robot allows automatic sample loader capability. The computer cluster was upgraded with 32 CPUs on a dedicated optical fiber 1 Gbit/s subnet. The total reconstruction time is 90 s for a 3D volume of 512^3 pixels and 420 s for a 1024^3 pixel volume. We are also investigating new cluster topologies to further improve these results. Combined with the dedicated reconstruction computer cluster and the higher flux delivered by the 2-BM DMM, these system innovations provide the scientific community with a fast, reliable, remotely controllable, easy-to-use 3D x-ray imaging tool with ~1 μm spatial resolution and ~1 mm field of view.

1.8.4 Integration of a Hard X-ray Microprobe and Six-Circle Diffractometer

X-ray microdiffraction combines conventional diffraction techniques with x-ray microbeam capabilities to achieve spatially resolved phase, crystallographic, and strain information about materials. We have completed the design and construction of a Fresnel-zone-plate-based hard x-ray microprobe (HXRM), and integrated it into a six-circle "kappa"

diffractometer for microdiffraction studies at the 2-ID-D beamline (Libera et al., 2002). The kappa geometry accommodates the HXRM in the tight region near the specimen, providing wider access to reciprocal space. The HXRM employs gold phase zone plates with focal lengths of 10 cm and 40 cm (at 8 keV) for high and moderate focusing power. The 10 cm and 40 cm zone plates have diameters of 150 μm and 250 μm, outmost zone widths of 0.1 μm and 0.25 μm, and focal efficiency of 18% and 25% for 8 keV x-rays, respectively. We measured photon fluxes of 1.0×10^{10} and 1.1×10^{11} ph/s/0.01% BW at their foci, corresponding to photon density gains of 15000 and 8000. A two-zone-plate stack was implemented in the HXRM to further improve focusing efficiency, especially at higher energies; gains as high as 3.5 were measured with 10 cm zone plates at 10 keV. Precise alignment of the two zone plates is determined by monitoring the resultant interference pattern (Fig. 1.28, left). The stability of the focal spot and sample position characterizes the performance of the instrument. The HXRM table is supported directly by the diffractometer at one end; a structural steel weldment reinforced with steel webs supports the other end on the same granite base (Fig. 1.28, right). The measured effective beam size is less than 250 nm (Xu et al., 2002).

1.8.5 Fabrication of X-ray Optics by Deep X-ray Lithography

Our deep x-ray lithography (DXRL) program has concentrated on producing 1-mm- to 1-cm- thick structures for advanced accelerator and x-ray instrumentation applications. The facilities, masks, preparation, and processing for 1-mm-thick PMMA photoresists developed so far allow us to fabricate various x-ray optical elements, such as refractive lenses, lobster-eye lenses, and x-ray collimating grids. Lobster-eye optics, square-packed arrays of square channels so-called for their similarity to the eyes of the macruran crustaceans, show great promise as the focusing optic in the next generation of x-ray all-sky monitors. We produced high-aspect-ratio lobster-eye optics using the LIGA process with a graphite substrate (Peele et al., 2001). In the medical field, conventional diagnostic mammography systems for breast cancer detection use ~28 kVp x-rays produced by a point source placed 60 cm above the image receptor, centered on the chest wall (Fig. 1.29, left). Without a collimating grid placed above the receptor to reduce the scattered radiation, the typical ratio of scattered-to-primary radiation at the receptor ranges from 0.3 to 1.0, reducing both the signal-to-noise ratio and contrast in diagnostic images. Our goal is the development of a collimating grid with: (1) an air core, (2) lamellar walls oriented to the x-ray source, (3) square-shaped lamellae with

~0.5 mm period, (4) lamellae thickness of 25 μm, and (5) an aspect ratio of wall height to wall thickness of ~100. In a cooperative agreement with Creatv Microtech, Inc., we developed a freestanding copper grid, $45 \times 50 \times 1$ mm^3 in size, with uniform, parallel, smooth, void-free walls, and an aspect ratio exceeding 40 (Fig. 1.29, right) using graphite substrates (Makarova et al., 2002).

1.8.6 Development of a Hard X-ray Nanoprobe at the APS

A new Center for Nanoscale Materials (CNM) is planned for Argonne National Laboratory. The scientific scope of the CNM embraces the fabrication and exploration of novel nanoscale materials that give rise to new properties and phenomena. A next-generation x-ray beamline at the APS will be a cornerstone of the characterization tools available for nanoscience at the CNM. The x-ray nanoprobe (Fig. 1.30) will be a second-generation hard x-ray probe facility with a spatial resolution of 30 nm, covering an
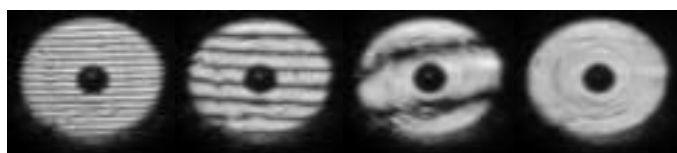

Fig. 1.28. Left: Interference patterns obtained with various transverse displacements of two stacked zone plates. The spatial frequency of the interference fringes becomes zero as the two zone plates are aligned. Right: HXRM and diffractometer in the 2-ID-D station. The x-ray beam enters from the left.

energy range from 3 keV – 30 keV. It will combine diffraction, x-ray fluorescence, and full-field imaging with absorption and phase contrast in a single instrument to study nanomaterials and nanostructures, with particular emphasis on the study of embedded structures. The nanoprobe, in its various operational modes, will allow real space mapping of (1) density and elemental composition through transmission, (2) crystallographic phase, strain, and texture through diffraction, (3) trace elements through fluorescence, (4) chemical states through spectroscopy, (5) magnetic domain structure through linear and circular dichroism, and (6) morphology through tomography. The nanoprobe will be a versatile tool that can be used, for example, to image and track domain evolution in ferroelectric and magnetic nanostructures, to observe strains in microelectronic interconnects, to measure composition and phase distributions in layered nanoparticles for catalysis, or to determine the position and chemical state of hybrid inorganic/organic nanoparticles interacting with biological systems.

1.9 High-Resolution X-ray Scattering

The High-Resolution X-ray Scattering (HRX) Group's activities are focused on developing x-ray optics and applications in nuclear resonant scattering, inelastic x-ray scattering, and other applications of high-resolution x-ray scattering techniques to fundamental measurements with resolution power exceeding 10^7 in the hard x-ray regime between 6-3 0 keV. The development emphasis is on mono-chromators, analyzers, detectors, software, and methodology.

Inelastic nuclear resonant scattering allows direct determination of partial phonon density of states in samples containing a suitable isotope with a low-energy nuclear transition with sub-meV energy resolution. **Coherent nuclear resonant scattering** allows determination of electronic and atomic structure around the probe atom through measurements of hyperfine interaction parameters in the neV energy scale. This is a particularly interesting area for nanoscale magnetism in thin films and multilayers, especially when combined with polarization-selective x-ray scattering techniques at nuclear resonance energy.
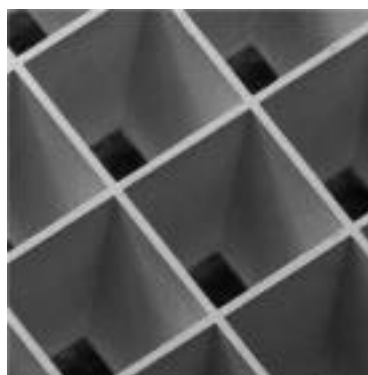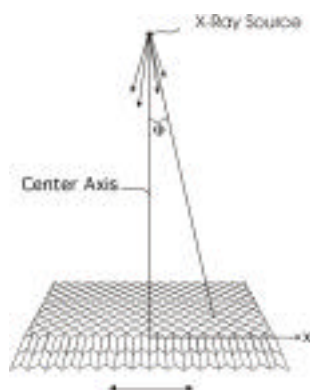
Fig. 1.29. Left: Ideal collimating grid with square septa oriented to a point x-ray source at 60 cm. Right: Copper septa are 25 μm thick and over 1,000 μm high (aspect ratio >40).
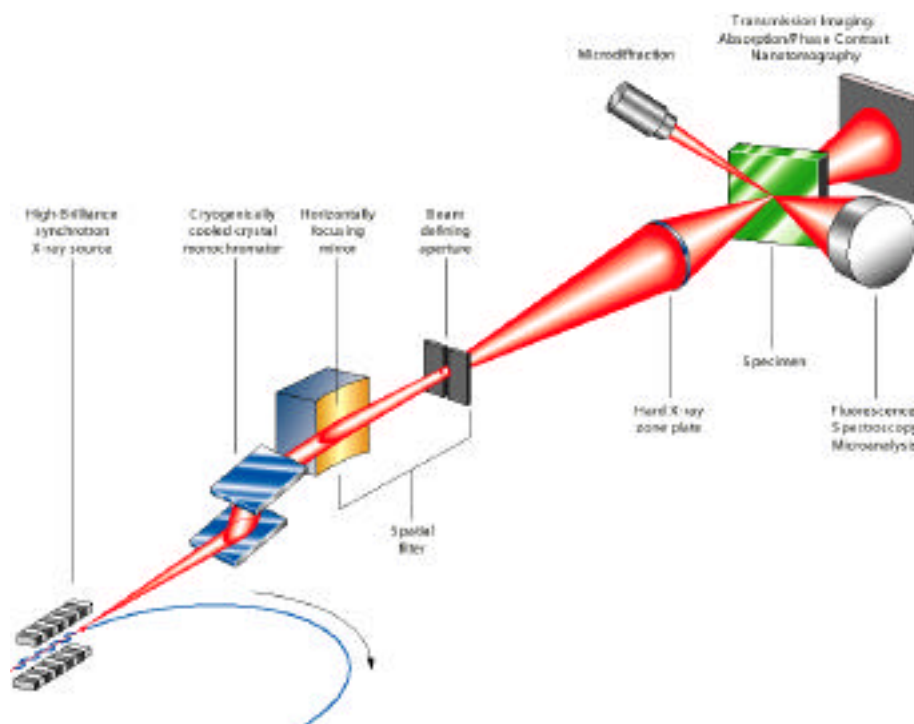
Fig. 1.30. Schematic of the scanning hard x-ray nanoprobe. Two collinear APS undulator A insertion devices provide a tunable, high-brilliance x-ray source. Fresnel zone-plate lenses serve as focusing and imaging optics with a spatial resolution of 30 nm. A spatial filter consisting of a focusing mirror and a beam-defining aperture provides spatially coherent illumination of the zone plates.

Inelastic x-ray scattering, on the other hand, enables measurement of phonon dispersion relations and form factors in single crystals, polycrystals, amorphous and liquid samples. The emphasis in nuclear resonant scattering is developing unique applications, like high pressure, biological materials, and thin films and multilayers. The emphasis in inelastic x-ray scattering is more on the spectrometer development, in terms of resolution, throughput, and accuracy.

Fundamental constant measurements are related to precision measurements of wavelengths and lattice constants with a precision exceeding current methods by two orders of magnitude. This may lead to establishment of new length standards at the Angstrom level and better definition of Avagdaro's constant. The applications are related to in-depth analysis of normal incidence diffraction (Sutter et al., 2001), x-ray Fabry-Perot interferometer (Sinn et al., submitted), use of LLL-interferometers for phase determination (Sturhahn, 2001), absolute wavelength measurements (Shvydko et al., 2000), and analysis of radiation from rotating frames (Röhlsberger et al., 2000; 2001) in the long pursuit of both μeV-resolved inelastic x-ray spectroscopy and measurement of lattice constant and thermal expansion coefficients of pure germanium isotopes (Hu et al., submitted).

The uniqueness of the HRX Group's effort comes from several sources: a) the ability to provide highly monochromatic and widely tunable crystal monochromators with resolution power exceeding 10^8 over a large energy range, b) having access to well-defined nuclear resonance energies with a resolution exceeding 10^{13}, and c) the infrastructure at the APS that enables development of bent crystal analyzers and monochromators.

1.9.1 Introduction

High-resolution nuclear resonant x-ray scattering (NRS) and momentum-resolved inelastic x-ray scattering (IXS) programs are designated as "strategic instruments," indicating their long-term development schedule and innovative scientific nature. This group was charged to develop instrumentation beyond the state-of-the-art for the specific scientific purpose of inelastic and nuclear resonant scattering. The energy range was limited to 6 – 30 keV to cover a half dozen suitable nuclear resonant isotopes and appropriate backscattering energies of silicon crystals used for analyzers. These are shown in Table 1.2. An optimized undulator with a period of 2.7 cm was chosen to cover this range within the first and third harmonics.

When the beamline was planned in 1993-95, state-of-the-art high-resolution monochromators were 5 meV at 14 keV and 15 meV at 24 keV. Within the first five years, this has been pushed to sub-meV levels between 10-30 keV, with a record resolution of $1.7\text{x}10^8$ at 24 keV, corresponding to 0.14 meV. Table 1.2 provides a comparison to highlight the progress at sector 3.

The current development in high-resolution monochromatization involves incorporation of more artificial channel-cut assemblies to allow new 4-crystal geometry to switch from (+ + - +) to (+ - - +), enabling 1-meV-level monochromatization at x-ray energies below 10 meV. Furthermore, feasibility tests are being performed to provide cryogenically cooled monochromators for increased throughput and additional energy stability for energies above 20 keV. Great progress has been made to provide efficient, high-resolution analyzers. All the necessary technology for dicing, gluing, and bending is now available in-house, and the consistent results obtained provide confidence for a future beamline. The IXS-CAT, currently under construction, derives most of its optics infrastructure from the developments that have taken place at sector 3.

For the IXS program, sector 3 staff had adopted a novel approach by employing "in-line" scanning monochromators and "dynamically bent" backscattering analyzers. This approach enabled the development of both NRS and IXS at the same beamline and provided the opportunity to explore newer applications of high-resolution x-ray scattering in the areas of x-ray metrology, x-ray interferometry, and exact backscattering. Furthermore, we have quickly adopted several key developments in other areas of x-ray optics. These include x-ray focusing using Kirkpatrick-Baez (K-B) mirrors and the use of a diamond phase plate for the production of circularly polarized light with switchable helicity.

At sector 3, development of every new instrument coincided with their scientific applications. Higher resolution micro-focused beams for high-pressure applications, high-resolution in-line monochromators for multilayer and thin films, a sub-meV monochromator for protein dynamics, high-resolution circularly polarized beams for spin structure determi-

Table 1.2. Progress made in high-resolution monochromatization since the commissioning of beamline 3-ID. The isotopes refer to stable Mössbauer nuclei, and Si reflections refer to exact backscattering planes used as an analyzer for the momentum-resolved IXS spectrometer. Only the highest resolution achieved at a given energy is listed.

Energy (keV)	ΔE (meV) 1996	ΔE (meV) 2001	Purpose
9.4	-	1	^{83}Kr -resonance
14.4	5	0.6	^{57}Fe - resonance
21.5	-	0.6	Si(18 6 0) back reflection and ^{151}Eu resonance
23.88	15	0.14	^{119}Sn resonance
25.5	-	0.5	Si(13 13 13) back reflection and ^{161}Dy resonance

nation in magnetic multilayers, an in-line IXS spectrometer for structure determination of levitated liquids at temperatures exceeding 2,500K. In some cases, the developments were requested by users: the monochromator for ^{83}Kr at 9.4 keV, or the 1 meV overall resolution IXS spectrometer for IXS-CAT. In many other cases, it was a classic case of "supply-induced demand," namely presenting the potential to the scientific community through talks, at conferences, workshops, university colloquia, papers, and private communications. Four PhD students (P. Abbamonte, J. Sutter, M. Hu, and A. Alatas) completed their thesis research entirely at sector 3, and currently three others are pursuing their degree at the APS as they permanently reside here. Many individual National Science Foundation (NSF), Department of Energy (DOE), and National Institute of Health (NIH) proposals were granted based on the capabilities of sector 3 spectrometers. This intense outreach effort resulted in galvanizing the scientific community to generate two successful large-scale proposals to DOE and NSF to build a new beamline, IXS-CAT, at the APS.

The scientific program at sector 3 can be summarized as follows:

1) **Nuclear resonant scattering**
2) **Momentum-resolved inelastic x-ray scattering**
3) **Fundamental measurements**
4) **Technical developments**

These programs are complemented by rigorous x-ray optics and instrumentation programs, as well as pursuit of new opportunities in applications of high-resolution x-ray scattering.

1.9.2 Nuclear Resonant Scattering

The HRX Group introduced this particular scientific application in 1995, and we have maintained our worldwide leadership in this field to this date. In this period, the technique has been applied to Kr, Fe, Eu, Sn and Dy isotopes in the areas of **geophysics** (high pressure), **biophysics** (protein dynamics, model porphyrins), **material science** (thin films, multilayers, order-disorder phase transformations, nanomaterials, magnetism), **condensed matter physics** (phase transitions in correlated electron systems and phonon-

magnon coupling), and **chemistry** (Kr-intercalated clatrathes). We have organized international scientific workshops in 1997 at Argonne National Laboratory and in 2001 at ESRF. We are also scheduled to organize the next International Inelastic X-Ray Scattering Conference (IXS-2004).

High-Pressure Applications

The geophysics community has received this program very well worldwide, and we are now trying to expand its reach to the solid-state physics community as well. Along these lines, the observation of magnon-

phonon coupling through a magnetic phase transition driven by high pressure in FeO (wustite) is a good example, as shown in Fig. 1.31 (Struzhkin et al., 2001).

The new direction we are pursuing is to extend high-pressure measurements of phonon density of states to high temperatures (exceeding 2000K). This will allow mimicking of the earth's mantle and inner core, and thus the thermodynamic properties of perovskites and spinels can be deduced.
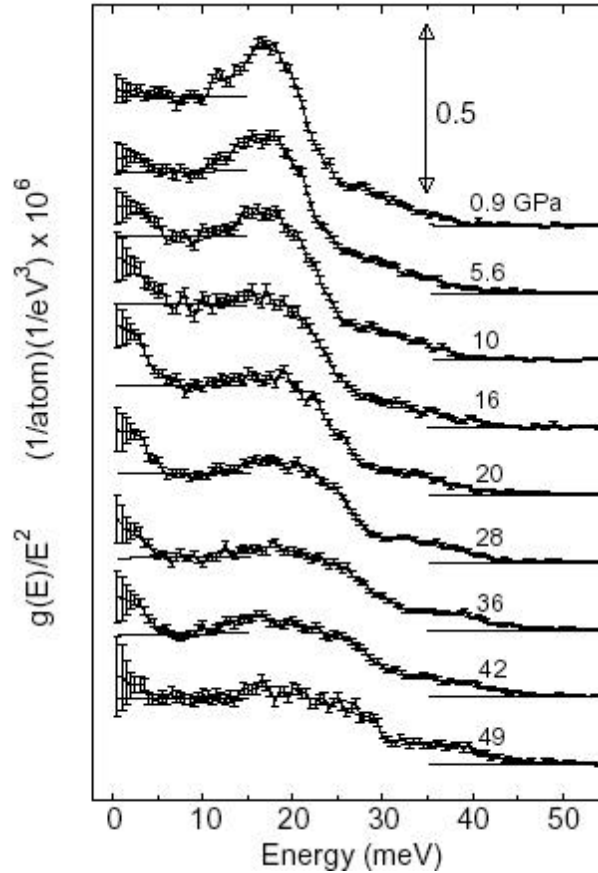
Fig. 1.31. The density of states of FeO, scaled with square of energy, as a function of pressure. The deviation from parallel lines in the low-energy region is most pronounced as FeO goes through a magnetic phase transition. This deviation from classical Debye behaviour is attributed to phonon-magnon coupling.

Biophysics Applications

The functional dynamics of proteins is an area that can be studied via vibrational modes of iron located at the center of heme molecules. Recent studies performed on myoglobin photolysis, in which CO molecules can be photolyzed with exposure to laser light, indicated the feasibility of measuring the change in the displacements of Fe with CO addition (Sage et al., 2001). In an attempt to quantitatively understand the vibrational density of states, these studies have been extended to model compounds, and single-crystal studies on these model compounds proved the potential to unambiguously differentiate between in-plane and out-of-plane vibrational modes. Figure 1.32 shows the analysis of vibrational modes in (nitrosyl) iron (II) tetra-phenylporphyrin (Rai et al., 2002).
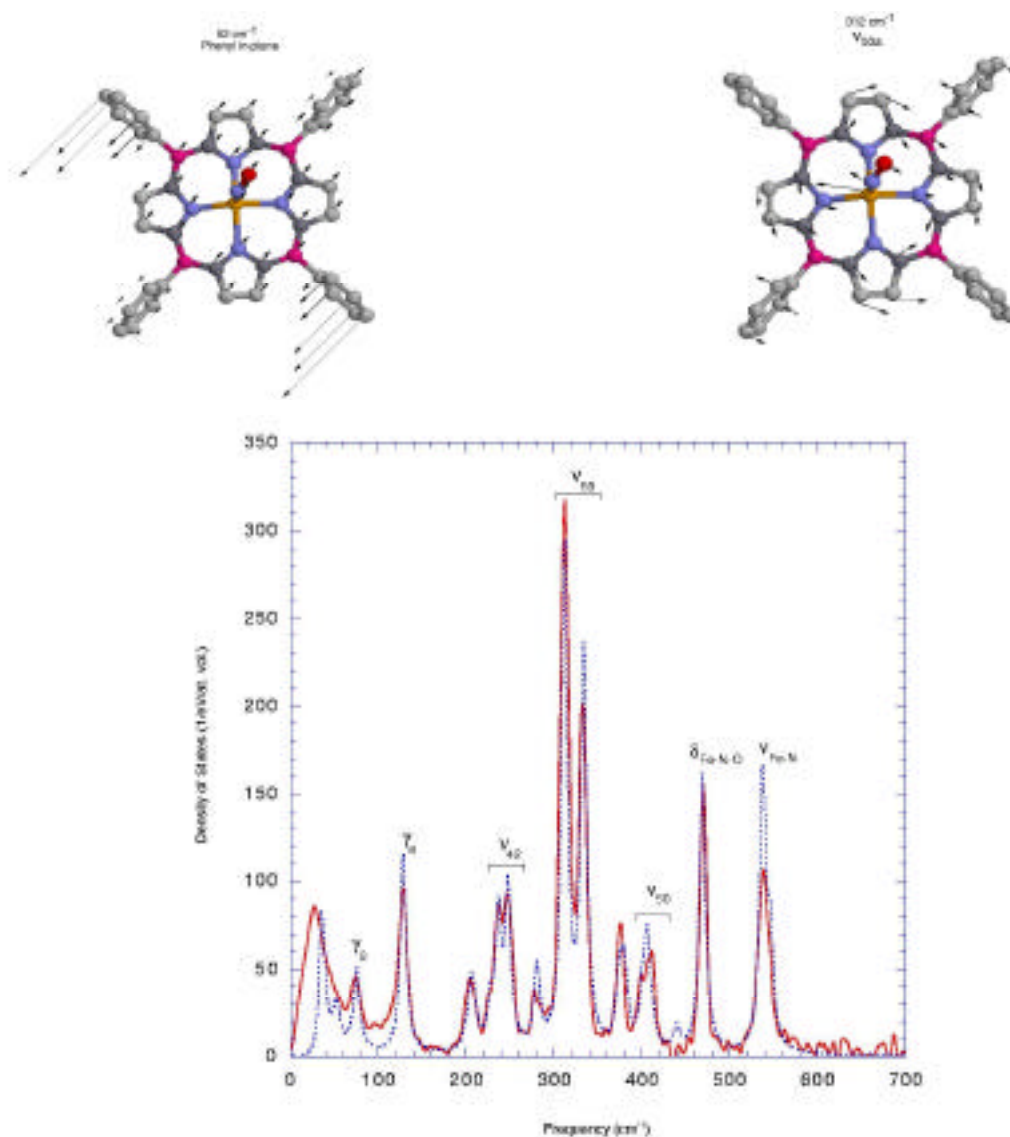
Fig. 1.32. Atomic displacements, their magnitude, direction and frequency measured through the iron atom in the center of the heme group.

Materials Science Applications

The measurement of vibrational properties from low-dimensional systems like thin films and multilayers has been extended to isotopically decorated layers, in which ^{57}Fe is selectively deposited at the interface or inside layers. Also, vibrational properties of amorphous layers in $Fe_{1-x}Tb_x$ and $Fe_{1-x}Y_x$ over a large composition range ($18 < x < 80$) have been studied. The emergence of soft phonon modes below 5 meV with increasing concentration of rare-earth element is interpreted as "boson peak," which needs to be understood in terms of a general explanation. Similar studies have been extended to Sn/Si multilayers (Roldan Cuenya et al., 2001), see Fig. 1.33.

1.9.3 Momentum-Resolved Inelastic X-ray Scattering

The inelastic spectrometer at the 3-ID-C station became available to outside users in 2000, and since then it has attracted a number of users from the materials physics and biology areas. Since this spectrometer is relatively new, a number of significant spectrometer improvements are still
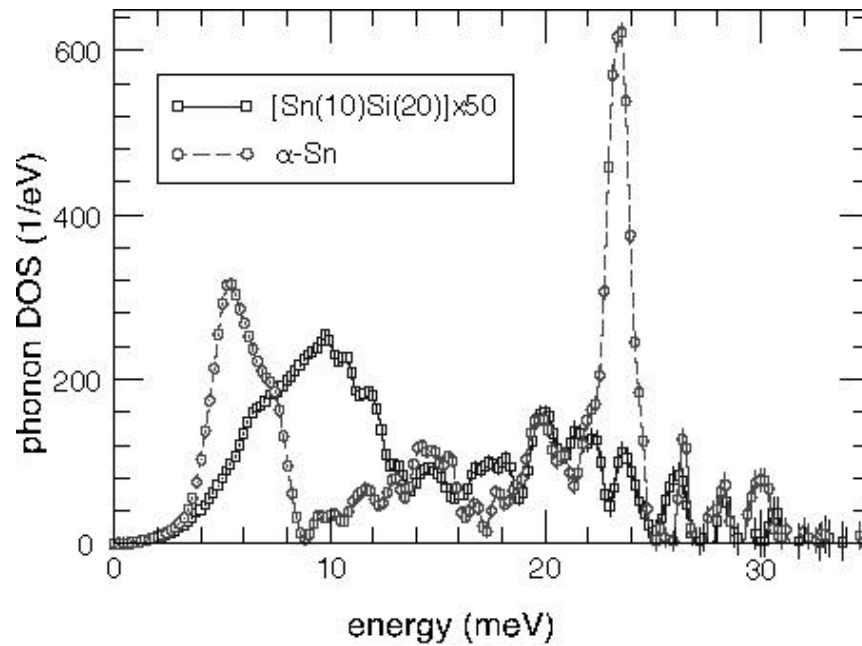
Fig. 1.33. The phonon density of states of -Sn and a Sn/Si multilayer. The structure and vibrational dynamics of room-temperature-grown nanoscale Sn/amorphous (a)Si multilayers have been studied by ^{119}Sn nuclear-resonant inelastic x-ray scattering (NRIXS) of synchrotron radiation. With increasing Sn-layer thickness, the formation of -Sn was observed, except at the Sn/Si interfaces, where a 10-Å-thick metastable pure amorphous a-Sn-like layer remains stabilized. By means of NRIXS, we have measured the Sn-projected vibrational density of states (VDOS) in these multilayers, in particular, at the interfaces and in 500-Å-thick epitaxial a-Sn films on InSb as a reference. Further, the Sn-specific Lamb-Mössbauer factor (f-factor), mean kinetic energy per atom, mean atomic force constant, and vibrational entropy per atom were obtained.

underway. These are incorporation of dynamically bent analyzers, increasing the number of analyzers from 1 to 4, and increasing the momentum transfer range from 3 to 5 Å^{-1}. In addition, changes are being implemented in the station to accommodate a containerless laser melting setup for high-temperature liquid studies (exceeding 2500K) and suitable sample mounting for single-crystal studies. Also, for development of the high-energy-resolution inelastic x-ray scattering (HERIX) spectrometer of IXS-CAT, a prototype 1 meV spectrometer has been tested, and an overall resolution of 1.04 meV has been obtained. This work will continue in the coming two years to build a high-throughput analyzer to be installed at the IXS-CAT HERIX spectrometer.

Microscopic Dynamics in Liquid Alumina

The properties of high-temperature oxide melts are of considerable geophysical interest, e.g., for modeling the earth's mantle, but are also important to a variety of technological problems like nuclear waste confinement. However, access to microscopic transport properties is often difficult to obtain with conventional techniques like ultrasound or viscosimetry because of the high temperatures and chemical reactivity of the oxide melts. Here we present data obtained with IXS on a liquid aluminum oxide sample levitated on a gas stream and heated by an infrared laser. The data set shows up to 6 nm^{-1} well-defined side peaks corresponding to a longitudinal phonon-like excitation in the liquid (Fig. 1.34). From the positions and the widths of these peaks, the high-frequency sound velocity and sound damping can be determined up to 2800°C (Sinn et al., in press), see Fig. 1.34.
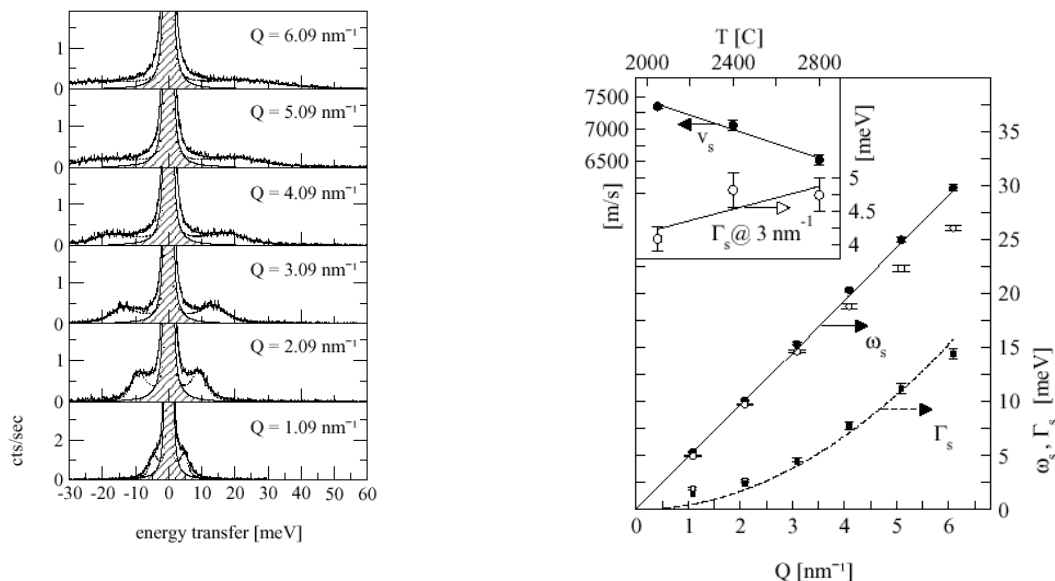

Fig. 1.34. Left: Inelastic x-ray spectra on liquid alumina at different momentum transfers. Right: Dispersion relation and damping obtained from the brillouin peaks. Inset: Temperature dependence of sound velocity and damping.

Liquid Mercury

Among the simple liquid metals, liquid mercury is the only one for which the critical point can be reached in a steady-state laboratory setup. In the vicinity of the critical point, the system undergoes a metal-to-nonmetal transition, which will affect the dynamics of the system dramatically towards a gas-like behavior with dimer formation. The persistence of these dimers in the liquid state has been the subject ofspeculation for some time. Due to the unfavorable cross section, mercury is difficult to investigate with neutrons. With x-rays, the most prominent problem is the high photoabsorption. In this measurement, we prepared a 20-µm-thick film between two sapphire crystals and measured in transmission geometry S(Q,) at different momentum transfers (see Fig. 1.35). Besides a quasi-elastic line, phonon-like excitations
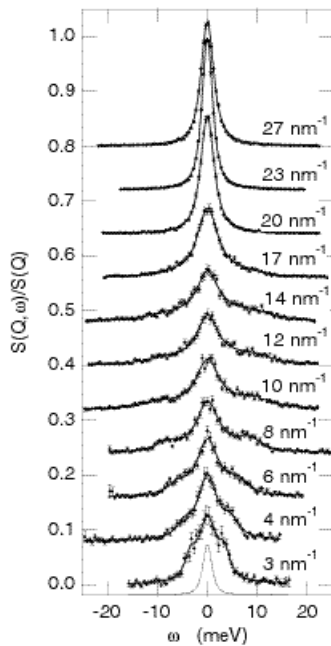
Fig. 1.35. Inelastic spectra of liquid mercury at different momentum transfers. The phonon-like excitations are visible as shoulders to the central peaks at small momentum transfers.

can be clearly resolved at low momentum transfers. For the data collected at room temperature, no indication of dimer formation could be found in the inelastic spectra (Hosokawa et al., in press).

1.9.4 Fundamental Constant Measurements and Interferometry

New applications for high-resolution x-ray scattering is a topic constantly pursued. The applications are related to in-depth analysis of normal incidence diffraction (Sutter et al., 2001), x-ray Fabry-Perot interferometer (submitted to Nature), use of LLL-interferometers for phase determination in nuclear forward scattering, and correct restoration of energy spectrum from the measured time spectrum (Sturhahn, 2001), absolute wavelength measurements (Shvydko et al., 2000), analysis of radiation from rotating frames (Röhlsberger et al., 2000; 2001), in the long pursuit of µeV-resolved inelastic x-ray spectroscopy, and measurement of lattice constant and thermal expansion coefficients of pure germanium isotopes (M. Hu et al., submitted) using normal incidence diffraction technique pioneered at 3-ID.

1.9.5 Technical Advances

The progress in scientific activities is directly coupled to the progress in technical capability developments. Along these lines, we can summarize the achievements in monochromators, analyzers, detectors, software development and methodology as follows.

Monochromators

The HRX group has been a recognized world leader in high-resolution monochromator development since 1992. Our emphasize is high-throughput, high-energy-resolution monochromatization for spectro-
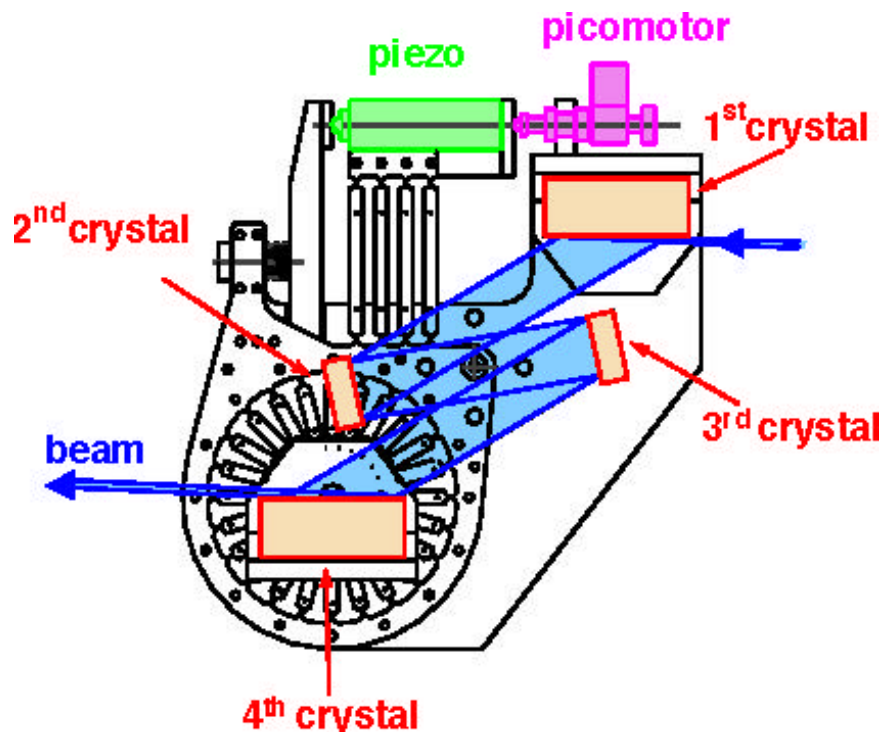
Fig. 1.36. A nested monochromator design, in which (++-+) geometry is used, and crystals 1 and 4 are linked the artificially, while crystals 2 and 3 were naturally channel cut. With this approach, it is possible to reach sub-meV above 20 keV, and, by cryogenic cooling, the throughput can be increased further. This is the current monochromator used for the 2 meV IXS spectrometer, 1 meV IXS spectrometer, 0.6 meV monochromator for ^{151}Eu, and 0.5 meV monochromator for ^{161}Dy nuclear resonance spectrometers.

scopy purposes. This program draws its strength entirely from the in-house talent and capabilities of XFD. In the last two years, the approach taken has been to exploit the artificial channel-cut technology (Shu et al., 2001) and optimization routines developed in crystal asymmetry and geometrical sequencing, for example, as shown in Figs. 1.36 and 1.37.

Analyzer Development
For momentum-resolved ineleastic x-ray spectroscopy, four highly efficient x-ray analyzers, which provide an energy resolution of about one meV, are essential. Typically, faceted silicon crystals in extreme backscattering geometry are used. To increase the efficience of these kind of

ana1yzers, we developed a new way of cutting the silicon with a high-speed diamond saw. A piece of 4-mm-tick silicon is cut half way through with a relatively thick blade (300 μm) and then glued with the cut side to a flat glass wafer. Finally, the silicon is diced from the top with a fine blade (50 μm), leaving a substantial higher fraction of the area on top as compared to a one-way cut with a thicker blade that would be required for this cut depth (Fig. 1.38). The resulting "mushroom"-like structure is also favorable for stress release from the glued backside. The flat glass wafer is then bent by a two-dimensional bending device to the desired radius of about 6 m. With this new cutting technique and the more precise

(a)
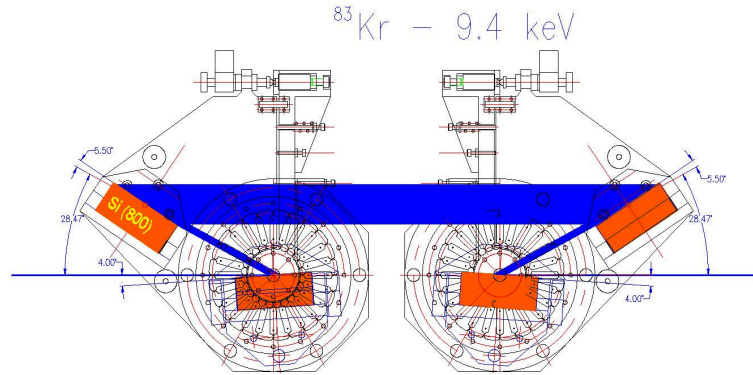
(b)
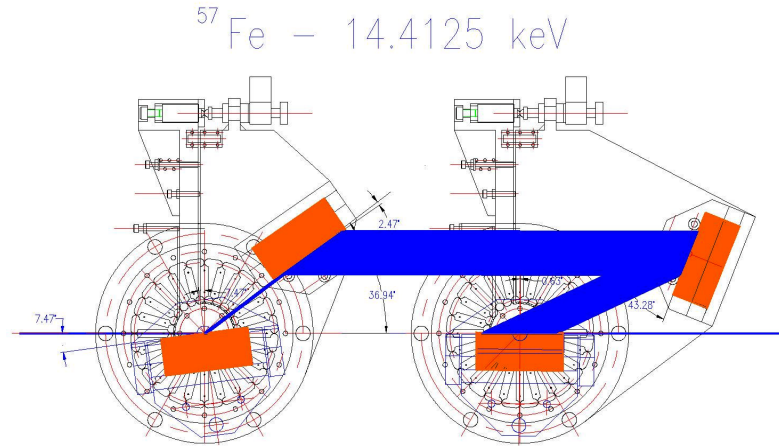
Fig. 1.37. The symmetric design of a new monochromator with (+-+-) geometry is used for (a) ^{83}Kr resonance at 9.4 keV, and (b) for ^{57}Fe at 14.4125 keV, both with a bandpass of 1 meV. The throughput is maximized by adjusting the asymmetry angles of the crystals, which are then linked with high-precision, high-stiffness links and thus called "artificial channel-cut." Here, the first two crystals and the last two crystals are linked artificially, and the two assemblies are treated as two channel-cut crystals placed in dispersive geometry against each other. This monochromator is used in high-pressure ^{83}Kr lattice dynamics measurements and will be used for future ^{57}Fe isotope-based studies, since the exiting beam can be further focused using a Kirkpatrick-Baez type mirror.

bending, the efficiency of the analyzer was more than doubled (Sinn et al., in press).

Detectors

Nanosecond time-resolved detectors are at the core of the nuclear resonant scattering program. The HRX Group embraced the development of avalanche photodiode (APD) detectors very early. There is a need for high efficiency and large area detectors for different reasons. For example, for NRIXS measurements at ^{57}Fe, the 6.4 keV fluorescence photons can be best detected with thin APDs covering a large solid angle, while experiments with ^{119}Sn at 24 keV need highly efficient detectors. The HRX Group has been collaborating with Perkin-Elmer engineers to develop these type of detectors and also with engineers and scientists in Hamburg University for fast, low-noise, high-gain cascade pre-amplifiers. The fruits of these activities over the last two years will be available for users of the 3-ID beamline next year; these detectors (Figs. 1.39 and 1.40) are currently under commissioning at the beamline. We expect the overall data efficiency to improve by a factor of three once the detectors and the data acquisition system are integrated.

Fig. 1.38. Schematics of the analyzer bender (top). The newly developed two-sided cutting technique allows a larger reflecting area on the top at a given thickness of the silicon (bottom figures).

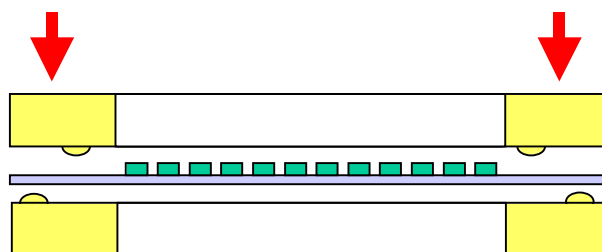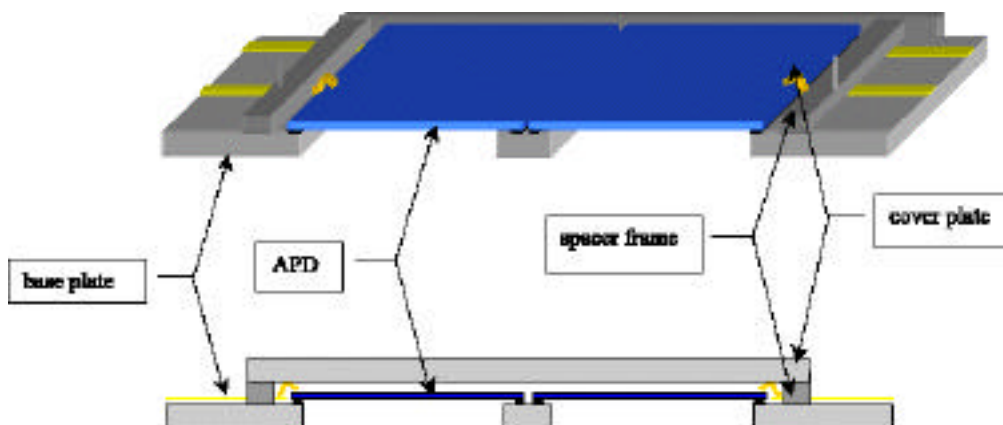Fig. 1.39. A 4-element large-area detector, covering 20 x 20 mm, made from four independently activated square diodes, with 10 mm size.
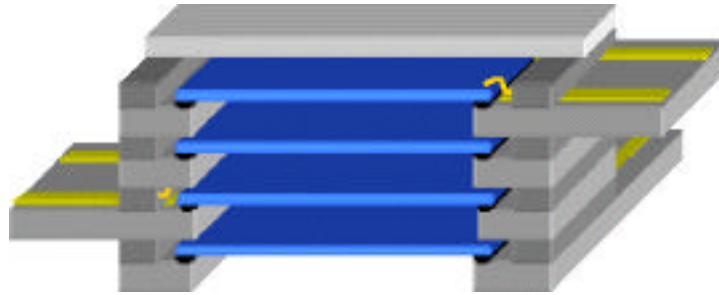
Fig. 1.40. A 4-element stacked-detector developed for high efficiency above 10 keV.

1.10 Polarization Studies

1.10.1 Introduction

The primary mission of the polarization studies program is to provide users with a high-brilliance, variably polarized x-ray beam. The polarized beams in sector 4 are produced by two separate undulators. To briefly review the main operational features, sector 4 has two branch lines, one for the "intermediate" (0.5 – 3 keV) and the other for the "hard" (> 3 keV) energy range. Variable polarization states are provided in the intermediate x-ray regime by a specialized circularly polarized undulator (CPU), while a planar undulator in combination with crystal optics has been used above 3 keV. A novel concept of spatially separating the beams from the insertion devices was successfully implemented for the first time at any synchrotron facility. The undulator axes are placed at a small angle (270 µrad) with respect to each other. A dipole electromagnet between the devices introduces the angular deviation of the electron beam, so 30 m away, in the first optics enclosure (FOE), the two beams are separated by 8 mm. This is sufficient to use two horizontally deflecting mirrors in the

FOE to further separate the beams and deflect the intermediate energy x-ray beam down the beam pipe. This design enables simultaneous operation of both branch lines and thus more efficient utilization of the delivered beam. At the APS its success has been embraced in the design of several upcoming new beamlines (GM/CA-CAT, SER-CAT, SGX-CAT).

Since the last XFD Progress Report all the construction activities were completed. The beamlines were declared operational on July 15, 2001. Commissioning activities commenced with a vigorous schedule with the aim to achieve designed performance specifications by July 15, 2002. The bulk of the commissioning activities were directed towards the liquid-nitrogen-cooled double-crystal monochromator (DCM) and the torroidal mirror on the hard x-ray branch, and on the CPU and deflecting mirrors on the intermediate x-ray branch. By December 2001, the DCM operated according to theory, delivering 5×10^{13} photons/sec at 10 keV with Si (111) crystals. The torroidal mirror now focuses that flux to a spot size of 200 µm by120 µm in the horizontal and vertical directions, respectively. The CPU is currently commissioned to operate in the circularly polarized mode with a switching

frequency of several minutes. The goal is to increase this frequency to 2 Hz. The degree of circular polarization was measured to be greater than 95% with a flux of 1×10^{13} photons/sec at 800 eV.

During the intense commissioning activities, whenever possible, cutting-edge experiments were simultaneously pursued. This approach resulted in publication of a *Physical Review Letter* article, "Enhanced interfacial magnetism in a Gd/Fe multilayer" in a record short time (Haskel et al., 2001). Concurrently, the emphasis on user support was given high priority as well, and, by July 15, 2002, already 28% of the beam time on the intermediate branch was awarded to independent investigators.

The development of state-of-the-art instrumentation and techniques using variable polarization resulted in several important contributions. They are described below and include probing magnetic interfaces in Fe/Gd with circularly polarized x-rays, measurement of magnetic ordering in $SmNi_2Ge_2$, magnetic characteristics of transition-metal/semiconductor structures and, finally, study of the oxidation process in a class of magnetic tunnel junctions.

1.10.2 Probing Magnetic Interfaces with Circularly Polarized X-rays

Understanding chemical and magnetic properties of interfaces in layered systems is of great scientific and technological interest. For example, chemical interfacial roughness affects spin-polarized transport and related giant magneto-resistance effect in spin valves (Schad et al., 1998; Bae et al., 2000). The goal of this work is to quantify fundamental properties of buried magnetic interfaces, including the strength and extent of interlayer exchange coupling and magnetic roughness (Haskel et al., 2001). This quantitative information was obtained

by performing both x-ray resonance exchange scattering (XRES) (Hannon et al., 1988) and x-ray magnetic circular dichroism (XMCD) measurements on a Gd/Fe multilayer. The markedly different Curie temperatures of Gd (293K) and Fe (1024K) allow us to distinguish Gd "bulk" and interfacial regions by tuning the sample temperature. More generally it allows investigating proximity effects between low and high Tc ferromagnets at the atomic scale.

The origin of the magnetic sensitivity of the XRES and XMCD signals arises from the same fundamental process illustrated in Fig. 1.41. By tuning the x-ray energy to near a spin-orbit split absorption edge (resonance), angular momentum is transferred from the circularly polarized (CP) x-rays to the spin of the excited photoelectron with opposite x-ray helicities resulting in equal but opposite signs of spin polarization. The imbalance at the Fermi level in the density of unoccupied states between spin-up and -down states of a ferro (ferri)-magnetic material results in different absorption (scattering) cross sections for opposite helicities of incoming x-rays giving a measure of element-specific net magnetic moments.
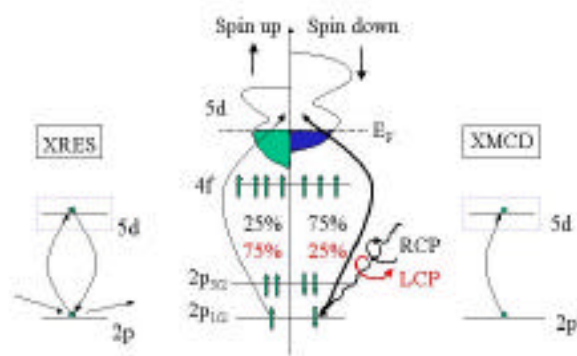

Fig. 1.41. Origin of magnetic sensitivity in the XRES (scattering) and XMCD (absorption) techniques.

Fig. 1.42. Experimental setup.

Fig. 1.43. Specular reflectivity curves across six multilayer Bragg peaks near the Gd L_2 edge (E=7929 eV) at T=300K. Top inset shows scattering geometry and applied field direction. Bottom inset shows derived interfacial magnetic structure (all units Å) along with the fit to the data (red line).

The experiment, shown schematically in Fig. 1.42, was performed at the 4-ID-D insertion device beamline. A diamond quarter-wave plate is used to convert the x-rays' linear polarization into circular. The sample and a small permanent magnet (B= 2.1 kGauss) were placed inside a closed cycle He refrigerator mounted on the circle of a diffractometer. The applied field was oriented parallel to the sample's surface and in the scattering plane. X-ray resonance magnetic reflectivity (Sinha et al., 1988; Osgood III et al., 1999; Nelson, 1999), a special case of XRES, measures the difference cross section in the specular reflectivity of left- and right-CP x-rays. The difference in absorption coefficient between opposite helicities is measured by XMCD. The absorption was measured monitoring the Gd L fluorescence yield.

Figure 1.43 shows specular reflectivity curves as obtained by adding (top) and subtracting (bottom) scattered intensities for opposite helicities of the incoming CP radiation. The sum yields the "charge" reflectivity curve related to interference between waves scattered from charge density variations; the difference is due to interference between waves scattered from charge *and* magnetic density variations. Magnetization density profiles in the Gd layers were parameterized through variations in magnetic scattering factors and refined in a nonlinear least squares fitting of

the Born approximation cross section to the data. Best fits at 300K (Fig. 1.43) show that Gd is paramagnetic except for a 4.1(7) Å region that remains magnetized near the Gd/Fe interface. This magnetization is induced by a strong antiferromagnetic (AF) interaction with the magnetically ordered Fe layer, in agreement with calculations by Camley (1989). The size of this region measures the spatial extent of the AF interaction at the interface and explains why Gd dominates the magnetization even above its bulk T_c.

The XMCD measurements are shown in Fig. 1.44. These data confirmed the size of the ordered Gd region obtained from the fit of the XRES spectra. At 300K, the Gd layers retain 20% of their saturation magneti-zation, consistent with the magnetic
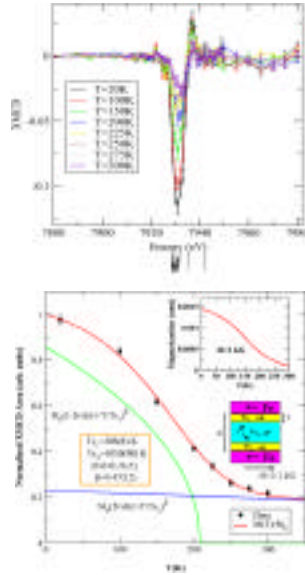
Fig. 1.44. XMCD data (top) and integrated area (points, bottom) at the Gd L_2 edge. Top inset in bottom figure shows SQUID magnetization data.

reflectivity result of 17% of the layer's volume remaining magnetized. The XMCD intensities are fitted as a superposition of interfacial and "bulk" regions with same saturation magnetization M_0 but variable T_c and volume fractions. The fit (red line) was convoluted with a Gaussian to account for disorder in the sputtered layers. Modeling gives 5.2±1.2 Å for the magnetized region at 300K with an estimated T_c=1050(90)K. This T_c quantifies the strength of the AF interaction at the Gd/Fe interface; i.e., J_{AF} J_{Fe} 1000K. An enhanced T_c of 800K was previously reported for one monolayer of Gd on a Fe(100) substrate (Taborelli et al., 1986).

In summary, we were able to quantify with high accuracy fundamental parameters characterizing a buried magnetic interface in a layered system. This includes the spatial extent and strength of interfacial exchange

coupling and interfacial magnetic roughness. Future work will be aimed at gaining a more complete understanding of the interfacial electronic and atomic structure. Spin-dependent x-ray absorption fine structure and XMCD combined with the x-ray standing wave technique should provide further insight into this question.

1.10.3 Fermi-Surface Nesting and Magnetic Ordering in SmNi$_2$Ge$_2$

It is not very common in solid-state physics to find an entire family of complex materials whose microscopic properties can be explained in terms of a few simple concepts. Rare-earth nickel germanides, however, do form such an isostructural group. Most of the moment-bearing members of this family undergo phase transitions at low temperatures below which the magnetic moments of the rare-earth ions spatially order in delicate arrangements. These intermetallics have a rather complicated tetragonal structure. As a result, the electronic structure of these compounds is quite intricate, and their magnetic ground state is determined by a subtle balance of various interactions, such as the long-range indirect exchange and single-ion crystal electric field effects. For almost all of the members of this group, the magnetic ordering wave vector has a fixed symmetry (along c*) and is incommensurate to the lattice. Despite these complexities, calculations of electronic susceptibility can pinpoint the origin of this behavior. A pronounced topological nesting of the Fermi surface has been found to exist in these materials that fixes the magnetic wave vector to be of the form q=(0, 0, qz=2k$_F$), where k$_F$ is the Fermi wave vector. The wave vector typically ranges between 0.75-0.81 r.l.u. (Islam et al., 1999; Islam, 1999). The primary objective of this experiment is to study the magnetic structures of the Sm-

member (SmNi$_2$Ge$_2$), which have not been studied before, to see if they are consistent with the Fermi-surface nesting picture or not.

X-ray resonant exchange scattering (Hannon et al., 1988; Gibbs et al., 1988) provides a unique tool in determining the properties of such complex magnetic structures. In particular, its high reciprocal-space resolution, the ability to study very small-volume samples, and its element specificity provide information inaccessible via neutron measurements. Furthermore, XRES can be used to study neutron opaque compounds, such as the Sm compound studied in this experiment.

A rectangular crystal with dimensions 2.5×0.9×0.3 mm^3, cut with a face perpendicular to [0,0,1] was used for this study. SmNi$_2$Ge$_2$ orders antiferromag-netically at T_N=17.9K and exhibits planar anisotropy above T_N. Another transition at T_t = 11.8K is also clearly observed (Bud'ko et al., 1999). The XRES measurements were performed on the 1-BM-C bending-magnet beamline. The incident photon energy was tuned to the L$_{II}$ edge (7.312 keV) of Sm in order to use the resonant enhancement. The (0, 0, 6) reflection from a flat pyrolytic graphite crystal was used as the polarization analyzer. Integrated intensity were measured using a Ge solid-state detector, and the sample was cooled in a closed-cycle He refrigerator.

According to the nesting picture, the magnetic modulation vector is expected to lie along **c***, with a **q**$_z$ value in the range mentioned above. A reciprocal lattice scan, at 8.0K, revealed superlattice peaks with a wave vector at **q**$_z$ (0, 0, 0.79). Figure 1.45 (left panel) shows an energy scan through the satellite peak at (0, 0, 4.79).
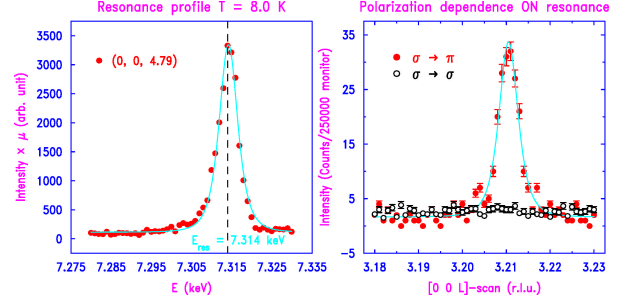
Fig. 1.45. Left: Energy scan through the Sm L$_{II}$-edge of superlattice peak. Right: Polarization analysis.

A strong resonant enhancement that occurs a few eV above the absorption edge, at 7.314 keV, with an enhancement factor of ~35 relative to the background ~25 eV below the edge. Polarization analysis (Fig. 1.45, right panel) revealed that the incident linear polarization perpendicular to the scattering plane (polarization) is completely rotated into the scattering plane (polarization). The resonance and polarization properties indicate that the superlattice peak is magnetic in origin (Hannon et al., 1988; Gibbs et al., 1988; Hill & McMorrow, 1996).

Figure 1.46 summarizes the temperature dependence of the ordered phases. The integrated intensity of the magnetic peak (top panel) remains nearly temperature independent below T_t, suggesting saturation of the ordered Sm moments. Above T_t, the intensity decreases monotonically and disappears above T_N. The lower panel shows the variation of the magnetic wave vector with T. In the phase below T_N but above T_t, the modulation vector changes continuously with T approaching ~0.775 r.l.u. near T_N, indicating the *incommensurate* nature of the ordering, consistent with the Fermi-surface nesting picture. Below T_t, however, the structure is characterized by a temperature-
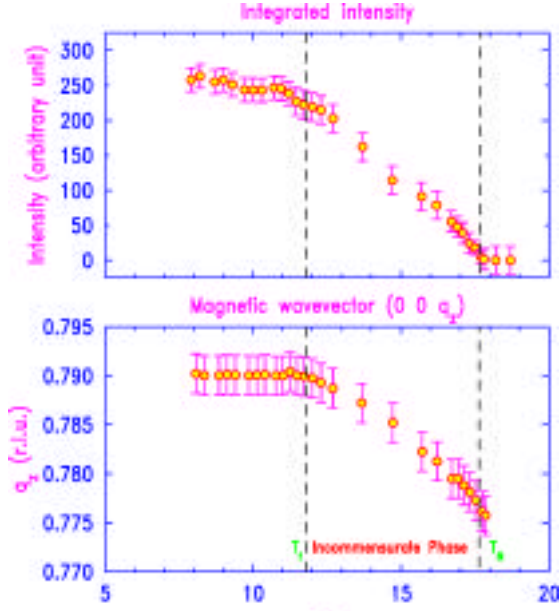
Fig. 1.46. Temperature dependence of the integrated intensity (upper) and position (lower) of the magnetic peak.

Fig. 1.47. Possible spin wave structures.

independent q = (0, 0, 0.79±0.002), suggesting a long-period ordered phase. The temperature at which q_z reaches this value is identified as T_t with a concomitant near saturation of the intensity, which is 11.8±0.2K.

The anisotropy of moment directions was also studied by measuring the intensity of a number of magnetic peaks. The intensity variation as a function of q suggested that the ordered Sm moments are essentially confined to the tetragonal basal plane. Although near T_N, the moments are free to rotate in the basal plane forming a helix (Fig. 1.47, left side) since the in-plane anisotropy is negligible, below T_t the moments may lock in along some crystallographic direction within the plane (Fig. 1.47, right side).

In summary, the primary result of this work is that the magnetic structures of the Sm-member of the RNi$_2$Ge$_2$ series conform to the topological nesting of the Fermi surface. SmNi$_2$Ge$_2$ orders in an *incommensurate* antiferromagnetic structure characterized by q=(0, 0, q_z). The value of q_z is T-dependent and approaches ~0.775 r.l.u. near T_N = 17.8±0.2K. The ordered moments are confined to the basal plane, as is in the case of a basal-plane helix or a plane wave.

1.10.4 Magnetic Characteristics of Transition-Metal/Semiconductor Structures

With the advent of spin-based electronics ("spintronics") the integration of thin magnetic layers with semiconductors is a priority (Prinz, 1995). The physics behind spintronics relies on the ability to inject spin-polarized currents into magnetic heterostructures. One such system that has shown very promising results is based on III-V materials (Kikkawa & Awschalom,

1999). It has been observed that spin injection into semiconductor quantum wells can retain spin coherence over length scales of 100 µm. This is several orders of magnitude more than is capable for transition-metal-based devices. The current magnetic semiconductors however suffer from low spin polarization and ordering temperatures. Transition metals are more favorable but are potentially incompatible with semiconductors (Xu et al., 1999) since alloying at the semiconductor/transition metal interface results in the formation of a magnetically dead layer and strongly modified magnetic anisotropy (see Fig. 1.48).

To date the detailed nature of the dead layer and anisotropy are not well understood. Using a combination of polarized soft x-ray techniques (XMCD and XRMS), a study has been initiated to understand the fundamental contributions to the magnetic characteristics of growing transition metals Fe, Co and Ni on Ge and GaAs. The samples were grown by molecular beam epitaxy at the University of Arizona. The high quality of the sample growth was monitored during growth with RHEED. The transition metals have been grown in a wedge format ranging in thickness from 0 Å to 50 Å and capped with a 35 Å Au protective layer. This sample provides continuous access to the whole thickness range which is necessary for a precise mapping of the onset of magnetic order.
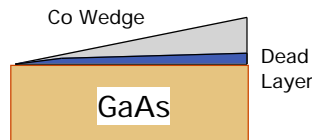
Fig. 1.48. An illustration of the magnetic dead layer that forms at the interface inhibiting such spin-injecting devices.

The XMCD technique is specifically powerful within this arena because of the accessibility to the 3d states of the transition metals (Thole et al., 1992). Figure 1.49 indicates the separate absorption spectra taken with opposite magnetic field directions. The resultant difference is the XMCD signal. XMCD is both element and site specific and has the ability to separate the constituent parts of the total magnetic moments into the spin and orbital contributions (Thole et al., 1992). This offers the possibility to assess the theoretical efforts of developing magnetic anisotropic energy models currently describing ultrathin transition magnetic materials on semiconductor substrates (Cabria et al., 2000).
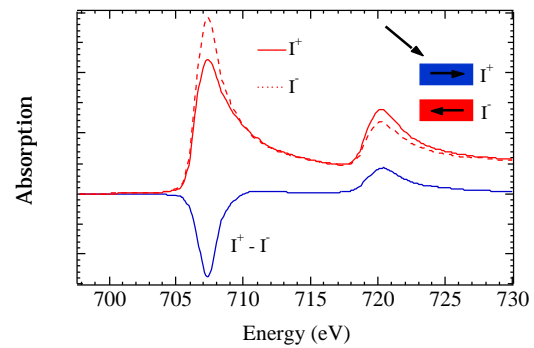
Fig. 1.49. Polarization dependent absorption spectrum measured at the Fe L edge. This contrast is a powerful tool for element by element magnetic analysis. The inset shows the orientation of photon helicity and magnetization for each measurement.

Results for the Co wedge on GaAs at both 300K and 90K are shown in Fig. 1.50 as a function of Co thickness. The onset of order is seen by a nonzero XMCD signal at 8 Å Co (4 monolayers). The intensity grows with increasing Co material but is not linear. Figure 1.51 indicates the rate of signal change with respect to Co thickness at both 300K and 90K. There is a significantly different rate of dichroism change at lower
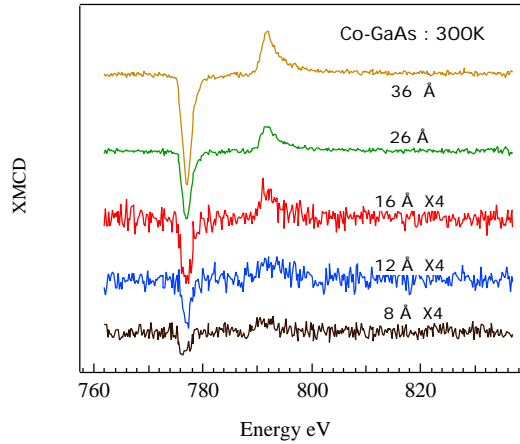
Fig. 1.50. Series of XMCD with total electron yield at 300K with different Co coverages. The XMCD signal shows the onset of magnetic order at 4 monolayer (ML) coverage.

Fig. 1.51. Thickness dependence of Co grown on GaAs. Note how the onset drops to 2.4 ML at 90K. More detailed analysis of the spin and orbital moments will provide insight into the thickness dependence.

Co coverage. This indicates an interface environment with a lower T_C. Primarily, dichroism at such low coverages has not been seen or the magnetic character been investigated to such degree. Here we see effects of the dead layer at very low coverages. Interestingly, the onset of dichroism shifts to lower Co coverage at lower temperatures, from ~4 monolayers (ML) at room temperature to ~2.6 ML at 90K.

Figure 1.52 shows a typical rocking curve spectra taken with 20 Å of Co. The spectrum is composed of two primary parts, the specular and diffuse signals. The ratio of which give an understanding of the physical and related magnetic roughness at the interface. Analysis of the sum and XMCD signals provides a measure of the chemical and magnetic perpendicular roughness ( ) near 2 Å. The narrow width indicates a long-range order in the plane of the film.

Application of the aforementioned techniques on such high-precision samples offers unprecedented information about the intrinsic characteristics of transition metals on semiconductors. Understanding the fundamental issues pertaining to such interfaces may refuel interest in such spin-injection devices.
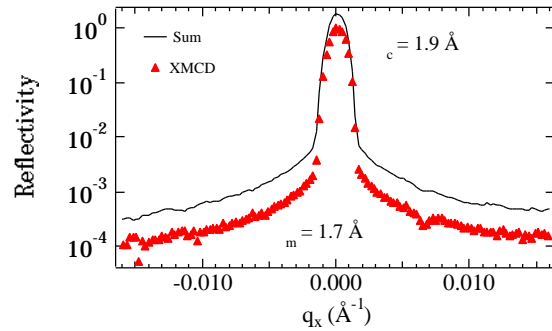
Fig. 1.52. X-ray resonant magnetic diffuse scattering at the Co L_3 edge. Analysis of the sum and XMCD signals provides a measure of the chemical and magnetic perpendicular roughness ( ). The narrow width indicates a long-range order in the plane of the film.

1.10.5 Linking the Oxidation Process with Magnetic Properties of Magnetic Tunnel Junctions

With the discovery of large spin-dependent tunneling in structures consisting of two ferromagnetic layers separated by a thin (~10 Å) insulating spacer (Moodera et al., 1995), new possibilities are evident for a variety of spin-based electronic devices. This system has potential applications from sensors to nonvolatile magnetic random access memory (MRAM), but many facets of the underlying structure and its impact on device physics are not well understood. Aluminum oxide (Al_2O_3) is the most widely used insulating spacer and is formed by the thermal or plasma oxidation of Al metal after deposition. Oxidation o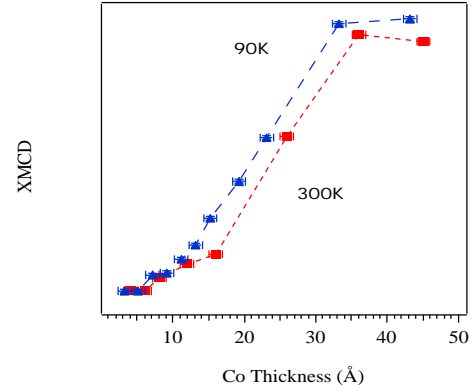f thin layers in proximity to transition-metal-based ferromagnets always leads to the potential for oxide formation in neighboring layers (Keavney et al., 2001; Seve et al., 2001). The goal of this study is to use the element- and interface-specific capabilities to track the oxidation process and changes due to thermal annealing.

A series of wedge-shaped structures were prepared by the Physical Sciences Research Laboratories at Motorola. Samples are grown using ion beam deposition, and the structure is shown in Fig. 1.53. The Al layer is deposited as a wedge from 5 - 9 Å and is plasma oxidized before deposition of the top NiFeCo layer. It is expected that in the region < 9 Å the bottom layer will show a linear progression of the oxide into the CoFe layer, but, as described in the text below, the real structure is quite different.

As the plasma oxidation is initiated, it proceeds along the following course. For the 9 Å end of the wedge, a stable film of Al_2O_3
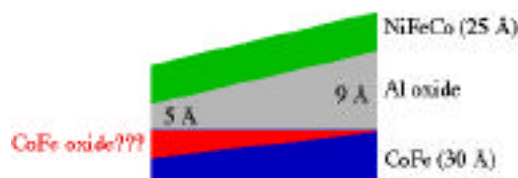
Fig. 1.53. Diagram of magnetic tunnel junction trilayer sample, which has been oxidized for an optimal Al oxide thickness of 9 Å.

is formed (see Fig. 1.54). The Al K-edge absorption is consistent with formation of a polycrystalline oxide layer. In the range of 9-7 Å, the Al K-edge spectra evolves to a metastable state consistent with the presence of excess oxygen in the layer and remains unchanged for all thickness < 7 Å. While the Al is still in a 3^+ oxidation state, the interstitial oxygen modifies the 3p density of unoccupied states (see Fig. 1.54). The trapping of excess oxygen in the Al layer reduces the oxide in the CoFe layer and only for an Al thickness < 7 Å does a large oxide component appear in the bottom layer (see Fig. 1.55).
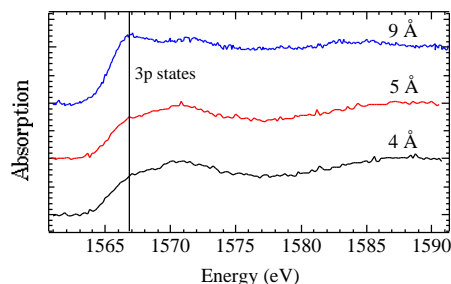
Fig. 1.54. Al K edge x-ray absorption spectra as a function of oxide thickness. The main feature denote by the line is related to the 3p density of unoccupied states. In the region of 9-7 Å this feature decreases in intensity as interstitial oxygen modifies the band structure.
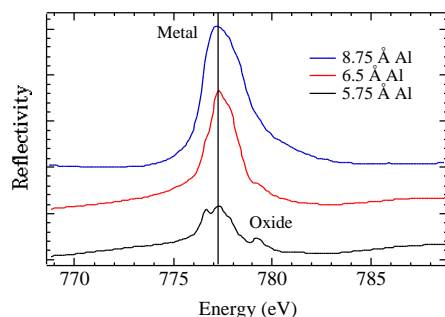
Fig. 1.55. X-ray resonant reflectivity at the Co L_3 edge. The features clearly indicate the oxidation of the CoFe underlayer at the thin end of the Al oxide wedge.

Fig. 1.56. Element-specific hysteresis measured at the Ni L_3 edge. This determines directly the field response of the top NiFeCo magnetic layer. Clearly the annealing process has a dramatic effect on the magnetic switching.

Determination of element-specific magnetic properties is accomplished using XMCD (Chen et al., 1995). The absorption and reflectivity from the sample is directly dependent on the orientation of the elements magnetic moment with respect to the helicity of the incident photon beam. This technique can be used to either monitor magnetic response to an applied magnetic field or more detailed analysis of the energy-dependent XMCD to determine spin and orbital magnetic moments. For this system, the most interesting aspect is the magnetic hysteresis of the two layers. The bottom layer is exchanged biased by an underlying IrMn antiferromagnet. Before the annealing to 200ºC in a 100 Oe applied field, the hysteresis consists of a large saturation field (1 kOe) and small remanent moment (10% of saturation). After annealing, the CoFe layer has 100% saturation at zero field and large exchange bias. The hysteresis of the top NiFeCo layer is shown in Fig. 1.56. Annealing the sample results in a dramatic decrease of the coercivity from 65 G to 19 G and slight shift of the loop to negative field direction. The coercive field is constant across the entire edge, but the coupling field varies due the changing dipolar coupling to the CoFe underlayer.

One of the major questions is the change in the structure after the field anneal. Are changes in the magnetic response due to structural or magnetic changes? Measurements of the x-ray magnetic resonant diffuse scattering (Freeland et al., 1999; Haskel et al., 2001) allow the determination of chemical and magnetic interface structure in a layer-by-layer fashion. Scattering at the Mn, Co, and Ni L_3 edges, provide element (and therefore layer) specific information. A Ni rocking curve measured at a $q_z = 0.3$ Å^{-1} is shown in Fig. 1.57. Analysis of the rocking curves show that the preanneal structure is characterized by a conformal roughness (= 3 Å and = 300 Å) propagating through the whole structure. After the anneal, there is no change, indicating that the structure is stable under these conditions and all magnetic changes are due solely to dipolar fields from the alignment of the random domains on the IrMn exchange bias layer.
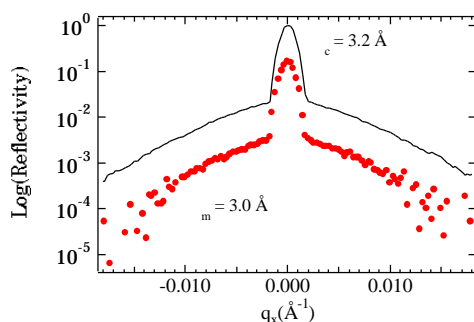
Fig. 1.57. X-ray resonant magnetic diffuse scattering at the Ni L_3 edge (852 eV). The chemical scattering (solid line) is connected to the structure of the chemical interface while the magnetic diffuse (red dots) is related to chemical and magnetic disorder.

1.11 References

A. Allen, J. Ilavsky, G. G. Long, J. S. Wallace, C. C. Berndt, and H. Herman, *Acta Mater.* **49,** 1661-1675 (2001).

S. Bae, J.H. Judy, W.F. Egelhoff Jr., and P.J. Chen, *J. Appl. Phys.* **87**, 6980 (2000).

M.J. Bedzyk, G.M. Bommarito, and J.S. Schildkraust, *Phys. Rev. Lett.* **62** (1989).

P. Bosecke and O. Diat, *J. Appl. Crystallogr.* **30**, 867-871 (1997).

W. Bras and A. J. Ryan, *J. Appl. Crystallogr.* **30,** 816-821 (1997).

S.L. Bud'ko, Z. Islam, T.A. Wiener, I.R. Fisher, A.H. Lacerda, and P.C. Canfield, *J. Magn .Magn. Mat.* **205**, 53 (1999).

I. Cabria, H. Ebert and A. Ya. Perlov, *Europhys. Lett.* **51**, 209 (2000).

R.E. Camley, *Phys. Rev. B* **39**, 12316 (1989).

C.T. Chen, Y.U. Idzerda, H-J. Lin, N.V. Smith, G. Meigs, E. Chaban, G.H. Ho, E. Pellegrin and F. Sette, *Phys. Rev. Lett.* **75**, 152 (1995).

Y.S. Chu, C. Liu, D.C. Mancini, F. De Carlo, A.T. Macrander, B. Lai, and D. Shu, *Rev. Sci. Instrum.* **73**, 1485 (2002).

D.H. Cole, K.R. Shull, L. Rehn, and P. Baldo, *Macromolecules* **32**, 771 (1999)

C.B. Collins, F. Davanloo, M.C. Iosif, R. Dussart, J.M. Hicks, S.A. Karamian, C.A. Ur, I.I. Popescu, V.I. Kirischuk, J.J. Carroll, H.E. Roberts, P. McDaniel, and C.E. Crist, *Phys. Rev. Lett.* **82**, 695 (1999).

F. DeCarlo, P. Albee, Y.S. Chu, D.C. Mancini, B. Tieman, and S.Y. Wang, *SPIE Proc. Vol.* **4503** (2002) p. 1.

D.E. Eastman, C.B. Stagarescu, G. Xu, P.M. Mooney, J.L. Jordan-Sweet, B. Lai, and Z. Cai, *Phys. Rev. Lett* **88**, 156101 (2002).

P.G. Evans, E.D. Isaacs, G. Aeppli, Z. Cai, B. Lai, *Science* **295**, 1042 (2002).

J.W. Freeland, K. Bussmann, Y.U. Idzerda, and C.-C. Kao, *Phys. Rev. B* **60**, R9923 (1999).

D. Gibbs, D.R. Harshman, E.D. Isaacs, D.B. McWhan, D. Mills, and C. Vettier, *Phys. Rev. Lett.* **61**, 1241 (1988).

J.P. Hannon, G.T. Trammell, M. Blume, and D. Gibbs, *Phys. Rev. Lett.* **61**, 1245 (1988).

D. Haskel, G. Srajer, J.C. Lang, J. Pollmann, C.S. Nelson, J.S. Jiang, S.D. Bader, *Phys. Rev. Lett.* **87**, 207201 (2001).

J.P. Hill and D.F. McMorrow, Acta. Crystallogr. A **5**, 236 (1996).

S. Hosokawa, H. Sinn, F. Hensel, A. Alatas, E. E. Alp, and W.C. Pilgrim, *J. Non-Cryst. Solids*, in press

Z.W. Hu, B. Lai, Y.S. Chu, Z. Cai, D.C. Mancini, B.R. Thomas, and A.A. Chernov, *Phys. Rev. Lett.* **87**, 148101 (2001).

M. Hu, et al., submitted to *Phys. Rev. Lett.*

J. Ilavsky, A. Kulkarni, T. Dobins, F. DeCarlo, H. Herman, and G. Long, *Proc. MRS2002 Conferenc*e, submitted.

Z. Islam, Ph. D. Thesis, Iowa State University (1999).

Z. Islam, C. Detlefs, C. Song, A.I. Goldman, V. Antropov, B.N. Harmon, S.L. Bud'ko, T. Wiener, P.C. Canfield, D. Wermeille, and K.D. Finkelstein, *Phys. Rev. Lett.* **83**, 2817 (1999).

D.J. Keavney, S. Park, C.M. Falco, and J.M. Slaughter, *Appl. Phys. Lett.* **78**, 234 (2001).

J.M. Kikkawa and D.D. Awschalom, *Nature* **397**, 139 (1999).

A. Kulkarni et al., unpublished

B. Lai, J. Maser, T. Paunesku, and G.E. Woloschak, *Intl. J. Rad. Bio.* **78**, 749 (2002); *Synchrotron Rad. News* **15**, 18 (2002).

W-K. Lee, K. Fezzaa, J. Wang, *Proc. ASME,* ICE-Vol. **37-1**, 11-14 (2001).

J. Libera, Z. Cai, B. Lai, and S. Xu, "Integration of a hard-ray microprobe with a diffractometer for micro-diffractrion," *Rev. Sci. Instrum.* **73**, 1506 (2002).

A.G. MacPhee, M.W. Tate, C.F. Powell, Y. Yue, M.J. Renzi, A. Ercan, S. Narayanan, E. Fontes, J. Walther, J. Schaller, S.M. Gruner, J. Wang, *Science* **295**, 1261 (2002).

O.V. Makarova, C.-M. Tang, D.C. Mancini, N. Moldovan, R. Divan, D.G. Ryding, R.H. Lee, *Tech. Digest*, IEEE MEMS, Las Vegas (2002), pp. 400-402.

P.J. McMahon, A. G. Peele, D. Paterson, J. Lin, T.H.K Irving, I. McNulty, and K. A. Nugent, submitted to *Phys. Rev. Lett.*

J.S. Moodera, L.R. Kinder, T.M. Wong, and R. Meservey, *Phys. Rev. Lett.* **74**, 3273 (1995).

C.S. Nelson, Ph.D Thesis, Northwestern University (1999).

R.M. Osgood III, S.K. Sinha, J.W. Freeland, Y.U. Idzerda, and S.D. Bader, *J. Magn. Magn. Mater.* **198-199**, 698 (1999).

D. Paganin and K.A. Nugent, *Phys. Rev. Lett.* **80**, 2586 (1998).

L.G. Parratt, *Phys. Rev.* **95**, 359 (1954).

G. Parry, in *Laser Speckle and Related Phenomena*, ed. J.C. Dainty (Springer-Verlag, New York, 1984), Chap. 3.

D. Paterson, B.E. Allman, P.J. McMahon, J. Lin, N. Modovan, K.A. Nugent, I. McNulty, C.T. Chantler, C.C. Retsch, T.H.K. Irving, and D.C. Mancini, *Opt. Commun.* **195**, 79 (2001).

A.G. Peele, T.H.K. Irving, K.A. Nugent, D.C. Mancini, T.R.Christenson, R. Petre, S.P. Brumby, and W.C. Priedhorsky, *Rev. Sci. Instrum.* **72**, 1843 (2001).

G.A. Prinz, *Physics Today*, April, 58, (1995)

A. Rahmim, S. Tixier, T. Tiedje, S. Eisebitt, M. Lörgen, R. Scherer, W. Eberhardt, J. Lüning, and A. Scholl, *Phys. Rev.* **B65**, 235421 (2002).

B.K. Rai, S.M. Durbin, E.W. Prohofsky, J.T. Sage, G.R.A. Wyllie, W.R. Scheidt, W. Sturhahn, E.E. Alp, *Biophys. J.* **82**, 2951 (2002)

C.C. Retsch and I. McNulty, *Phys. Rev. Lett.* **87**, 077401 (2001).

R. Röhlsberger, T.S. Toellner, W. Sturhahn, K.W. Quast, E.E. Alp, A. Bernhard, E. Burkel, O. Leupold, and E. Gerdau, *Phys. Rev. Lett.* **84**, 1007 (2000).

R. Röhlsberger, K.W. Quast, T.S. Toellner, P.L. Lee, W. Sturhahn, E.E. Alp, E. Burkel, *Phys. Rev. Lett.* **87**, 047601 (2001).

B. Roldan Cuenya, W. Keune, W. Sturhahn, T.S. Toellner, and M.Y. Hu, *Phys. Rev. B* **64**, 235321 (2001).

J.T. Sage, S.M. Durbin, W. Sturhahn, D.C. Wharton, P.M. Champion, P. Hession, J. Sutter, E.E. Alp, *Phys. Rev. Lett.* **86**, 4966 (2001).

R. Schad, P. Belien, G. Verbanck, K. Temst, V.V. Moshchalkov, Y. Bruynseraede, D. Bahr, J. Falta, J. Dekoster, and G. Langouche, *Europhys. Lett.* **44**, 379 (1998)*;*

L. Seve, W. Zhu, B. Sinkovic, J.W. Freeland, I. Coulthard, W.J. Antel, Jr., and S.SP. Parkin, *Europhys. Lett.* **55**, 439 (2001).

D. Shu, T.S. Toellner, and E.E. Alp, *Nucl. Instrum. Methods A* **467-468**, 771 (2001).

K.R. Shull and A.J. Kellock, *J. Poly. Sci., Polym. Phys.* **33**, 1417 (1995).

Y.V. Shvydko, M. Lerche, J. Jäschke, M. Lucht, E. Gerdau, M. Gerken, H.D. Rüter, H.-C. Wille, P. Becker, E.E. Alp, W. Sturhahn, J. Sutter, T.S. Toellner, *Phys. Rev. Lett.* **85**, 495 (2000).

D.P. Siddons, C. Riekel, and J.B. Hastings, *J. Appl. Crystallogr.* **23**, 401-405 (1990).

S.K. Sinha, E.B. Sirota, and S. Garoff, *Phys. Rev. B* **38**, 2297 (1988).

H. Sinn, N. Moldovan, A.H. Said, and E.E. Alp, *Proc. SPIE*, in press.

H. Sinn, B. Glorieux, L. Hennet, A. Alatas, M. Hu, E.E. Alp, F.J. Bermejo, D.L. Price, M.L. Saboungi, submitted to *Nature.*

S.R. Stock, T. Dahl et al., *Advances in X-ray Analysis*, in press.

S.R. Stock, K. Ignatiev, T. Dahl, J. Barss, A. Veis , K. Fezzaa, W.K. Lee, and F. DeCarlo, submitted to the *J. Microscopy Short Communications.*

V.V. Struzhkin, H-K. Mao, J. Hu, M. Schwoerer-Böhning, J. Shu, R.J. Hemley, W. Sturhahn, M.Y. Hu, E.E. Alp, P. Eng, G. Shen, *Phys. Rev. Lett.* **87**, 255501 (2001).

W. Sturhahn, *Phys. Rev. B* **63**, 094105 (2001).

J.P. Sutter, E.E. Alp, M.Y. Hu, P.L. Lee, H. Sinn, W. Sturhahn, T.S. Toellner, G. Bortel, R. Colella, *Phys. Rev. B* **63**, 094111 (2001).

M. Taborelli, R. Allenspach, G. Boffa, and M. Landolt, *Phys. Rev. Lett.* **56**, 2869 (1986).

B.T. Thole, P. Carra, F. Sette, and G. van der Laan, *Phys. Rev. Lett.* **68**, 1943 (1992).

J. Wang, M.J. Bedzyk, T.L. Penner, and M. Caffrey, *Nature* **354**, (1991).

M.W. Westneat et al., *SICB 2002 Annual Meeting*, p. 439 (2002).

S. Xu, B. Lai, Z. Cai, and D. Shu, *Rev. Sci. Instrum.* **73**, 1599 (2002).

Y.B. Xu, E. T. M. Kernohan, D. J. Freeland, A. Ercole, M. Tselepi, and J. A. C. Bland, *Phys. Rev. B* **58**, 890 (1999).

Y.K. Yoo, T. Ohnishi, G. Wang, F. Duewer, X.-D. Xiang, Y.S. Chu, D.C. Mancini, Y.-Q. Li, and R.C. O'Handley, *Intermetallics* **9**, 541 (2001).

2 USER TECHNICAL SUPPORT

2.1 Insertion Devices

Since the last *Experimental Facilities Division/User Program Division Technical Progress Report* (ANL/APS/TB-38, 2000), the Insertion Device Group (newly renamed the Magnetic Devices Group) has begun to deal with radiation damage to insertion devices (IDs). As routine use of top-up mode began, a decrease in the field strength of permanent magnets in the IDs with the highest dose rate is being seen. Significant damage levels are so far limited to sector 3, where the first small-aperture vacuum chamber downstream of injection is located. Devices from that and other sectors are being removed, retuned, and reinstalled during the shutdowns, both to keep the sector 3 users provided with acceptably operating IDs and to assess the damage elsewhere. Planned new dosimetry techniques have now been implemented, and additional shielding is being added.

A prototype for the undulators that will be built for the LCLS project has been assembled and is undergoing tuning and testing at APS. One goal is to search for possible economies in the production of the 33 undulators that will be needed for the Linac Coherent Light Source (LCLS).

Improvements have also been made to the ID magnetic measurement facility. Control systems have been updated with new hardware to replace obsolete components, and the software has been rewritten. An advantage of the new hardware is a significant reduction in the electronic noise levels, by eliminating the long wires to the motors, which contributed much of the noise in the Hall probe readings.

2.1.1 Dosimetry

At the APS concern for radiation damage of the IDs and other critical components has led to systematic dose monitoring at those components.

The IDs are subjected to a harsh radiation environment that can lead to radiation-induced demagnetization. This radiation environment is primarily composed of gamma rays, x-rays, electrons and neutrons.

Systematic dose monitoring on the IDs is used to determine the dose distribution profiles around the storage ring and the FEL, and regions where the probability of damage is highest. Integrated doses on the IDs also provide information on the magnitude of the damage threshold.

In addition, other critical components around the facility (such as CCD cameras, encoders, motors and cables) suffer from radiation aging. Integrated radiation dose measurements for these components give an indication of their radiation sensitivity and their lifetime in the APS radiation environment.

A dosimetry system would ideally exhibit radiation energy and radiation quality independent response in the radiation environment of interest. An additional requirement is a broad useful dose range. However, due to the broad spectrum of radiation energies, multiple radiation qualities, and very broad dose ranges around synchrotron facilities such a requirement can only be partially satisfied.

To date, dose monitoring at APS has been performed with LiF and $Li_2B_4O_7$:Mn TLDs

(thermoluminescent dosimeters) and radiachromic films. In addition, in 2002 a new high dose dosimetry technique has been added: alanine electron paramagnetic resonance (EPR) dosimetry. All these dosimetry techniques are tissue equivalent.

Alanine is an amino acid where the disrupted molecular bonding due to ionizing radiation gives rise to free radicals. The number of free, stable radicals is a function of the absorbed dose. The radical concentration can then be analyzed with EPR. Alanine dosimetry exhibits equivalent response for photons and electrons, and negligible temperature and humidity coefficients. In addition, it exhibits energy independent response above approximately 100 keV; however, dose underestimation occurs for photon energies below that value.

The EPR spectrometer is an e-scan Bruker analyzer that is suitable for both pellet and film alanine dosimetry and capable of providing dose measurements from 1 krad to 20 Mrad. The dosimeters used currently at the APS are alanine films with a saturation point equal to 50 Mrad.

Dosimetry measurements on the IDs have, so far, been performed on the upstream (US) and downstream (DS) ends of the devices. An effect on the absorbed doses is from the gap-size history during ID operation; maximum gap reduces the synchrotron background while it also allows for potential scattering of bremsstrahlung radiation in less critical directions. Currently the minimum gap on most IDs is 11 mm while the maximum gap is equal to 180 mm.

The US doses are also being affected by the absence or presence of shielding upstream of the IDs; a few IDs are not shielded due to space constraints. In addition, the absorbed doses are affected by nonuniformities in the vacuum and temperature profiles around the storage ring, and the current present in the ring. The storage ring lattice being used also affects the dose. Lattices with short lifetimes can be and are used during top-up operation; the short lifetime means a higher dose.

The TLD–800's ($Li_2B_4O_7$:Mn TLD's) were inserted in the storage ring for the first time during the run 2001-3 (Fig. 2.1) During that run they registered doses over 1 Mrad at the DS ends of many IDs, with the highest doses at the IDs in sector 3, APS27#2 and U27#12. The useful dose range of the TLD-800 extends up to approximately 10^7 rad.

Alanine dosimeters were inserted for the first time in the storage ring in 2002. The absorbed doses during run 2002-2 are shown in Fig. 2.2. High absorbed doses were again recorded on the IDs in sector 3. This is primarily due to an increased probability for non-gas bremsstrahlung following recent installation of a smaller aperture ID vacuum chamber in that sector. The recorded doses are higher in the DS end of the devices. The DS doses remained below approximately 1 Mrad while the US doses remained below approximately 100 krad on most other IDs.

To date, the potential for radiation damage appears to be highest in sector 3. Due to the radiation-induced demagnetization already observed in both U27#12 and APS27#2, those alanine dosimeters are now being replaced as often as machine intervention schedules allow so that changes to the dose rate can be detected more promptly. Dosimeters in the other sectors are being replaced at the end of each run (i.e., at approximately 3 month time intervals).

Additional shielding is being inserted in sector 3 in an attempt to reduce the dose to the IDs. In addition, temperature is being

monitored along the length of the IDs that suffered radiation-induced demagnetization.

During upcoming shutdowns IDs will be removed from the storage ring and checked for potential radiation damage. The IDs will be selected based partly on integrated dose results. In addition, IDs where significantly high absorbed doses were observed during one run (such as U33#30 in sector 22, Fig. 2.2) will also be examined for potential radiation damage.

The contribution to the total absorbed dose from synchrotron radiation, bremsstrahlung radiation and the associated photoneutron component need also to be evaluated for a better interpretation of the dosimetry results. Such calculations are planned for the APS radiation environment. In addition, the simultaneous use of different dosimetry techniques can potentially provide a better characterization of the radiation field and dose profile around the facility.

The response of the dosimeters at cryogenic temperatures is also of interest due to the potential addition of superconducting cavities at the APS. The response of alanine dosimeters in this temperature regime is quite well known. The relative response of the dosimeters at cryogenic temperatures for the dosimeters currently being used at the APS is being examined.

Future dosimetry plans also involve dosimetry intercomparison studies between APS and other accelerator facilities.

Routine dose monitoring on the IDs at the APS is critical; however, the primary focus of the radiation damage studies is a better understanding of the damage process so that efficient techniques can be developed to prevent the damage.
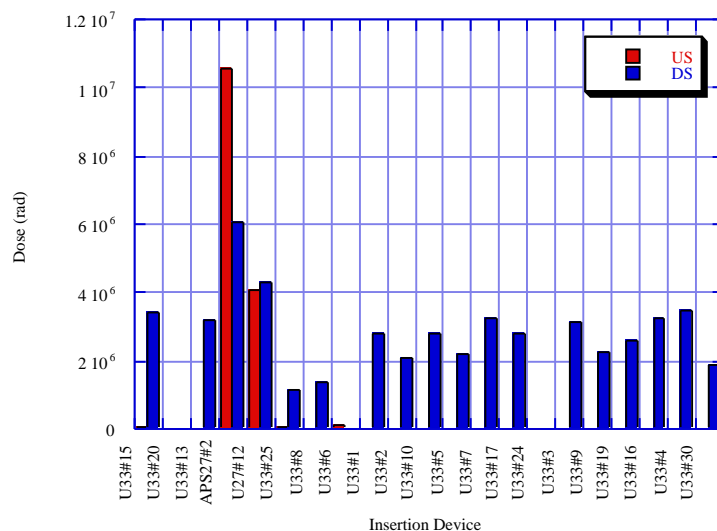
Fig. 2.1. Absorbed dose on the IDs recorded by TLD-800 dosimeters during run 2001-3.
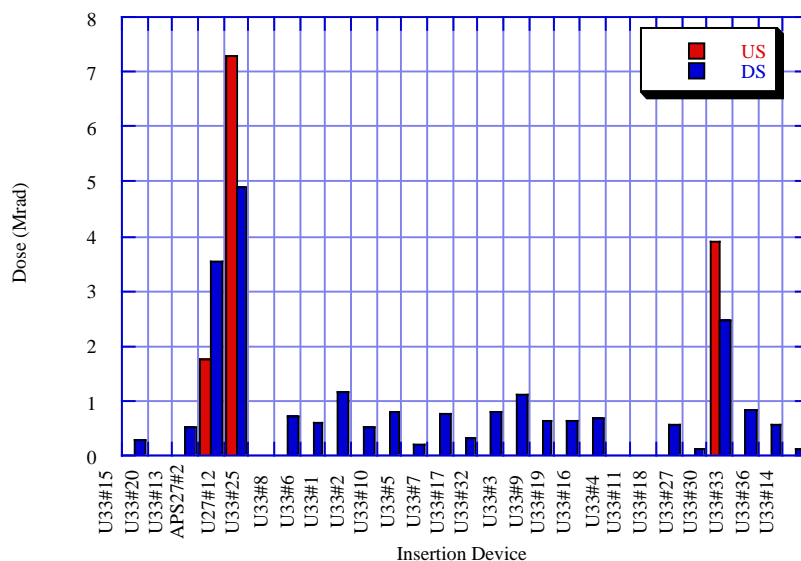
Fig. 2.2. Absorbed dose on the IDs recorded by alanine dosimeters during run 2002-2.

2.1.2 Radiation-Induced Damage to IDs

Damage has now been observed in a few IDs at the APS. During the August-September 2001 run, the APS was run in top-up mode for much of the run. In addition, a new low-emittance lattice was being used, and the injection efficiency had not yet been optimized for these new conditions. The smallest aperture in the ring is a 5-mm-aperture insertion device vacuum chamber, and the first such chamber after the injection point is located in sector 3. It is suspected that much of the beam that was lost during injection was lost there. Abnormally high doses were recorded by radiation dosimeters placed on the upstream and downstream end of the IDs in that sector. This prompted the removal of these devices from the storage ring during the December-January shutdown to check them for radiation damage.

As can be seen in Figs. 2.3 and 2.4, radiation-induced demagnetization was observed for both IDs, with the damage being more pronounced for the downstream U27#12. The performance of both devices was significantly impaired.

Monitoring of the dose to these devices continued during the Jan.-Apr. 2002 run, and the dose continued to be high, particularly for the downstream device. During the May 2002 shutdown, the downstream device, U27#12, was again removed to be rechecked, and more damage was found, as can be seen in Fig. 2.5.

Fig. 2.3. Magnetic field changes in the downstream undulator in sector 3, U27#12, at 10.5 mm gap. The top panel shows the peak magnetic field under each pole as measured in June 1997 (before the device was installed) and in Dec. 2001. The damage is small at the upstream end on the right. The bottom panel shows the difference in the magnetic field. (The data for the weaker end poles are omitted.)

61

Fig. 2.4. Magnetic field changes in the upstream undulator in sector 3, APS27#2, at 11.5 mm gap. The top panel shows the peak magnetic field under each pole as measured in March 2000 (before the device was installed) and in Dec. 2001. The damage is larger at the upstream end (on the right), in contrast to the damage to the downstream undulator. The bottom panel shows the difference in the magnetic field. (The data for the weaker end poles are omitted.)
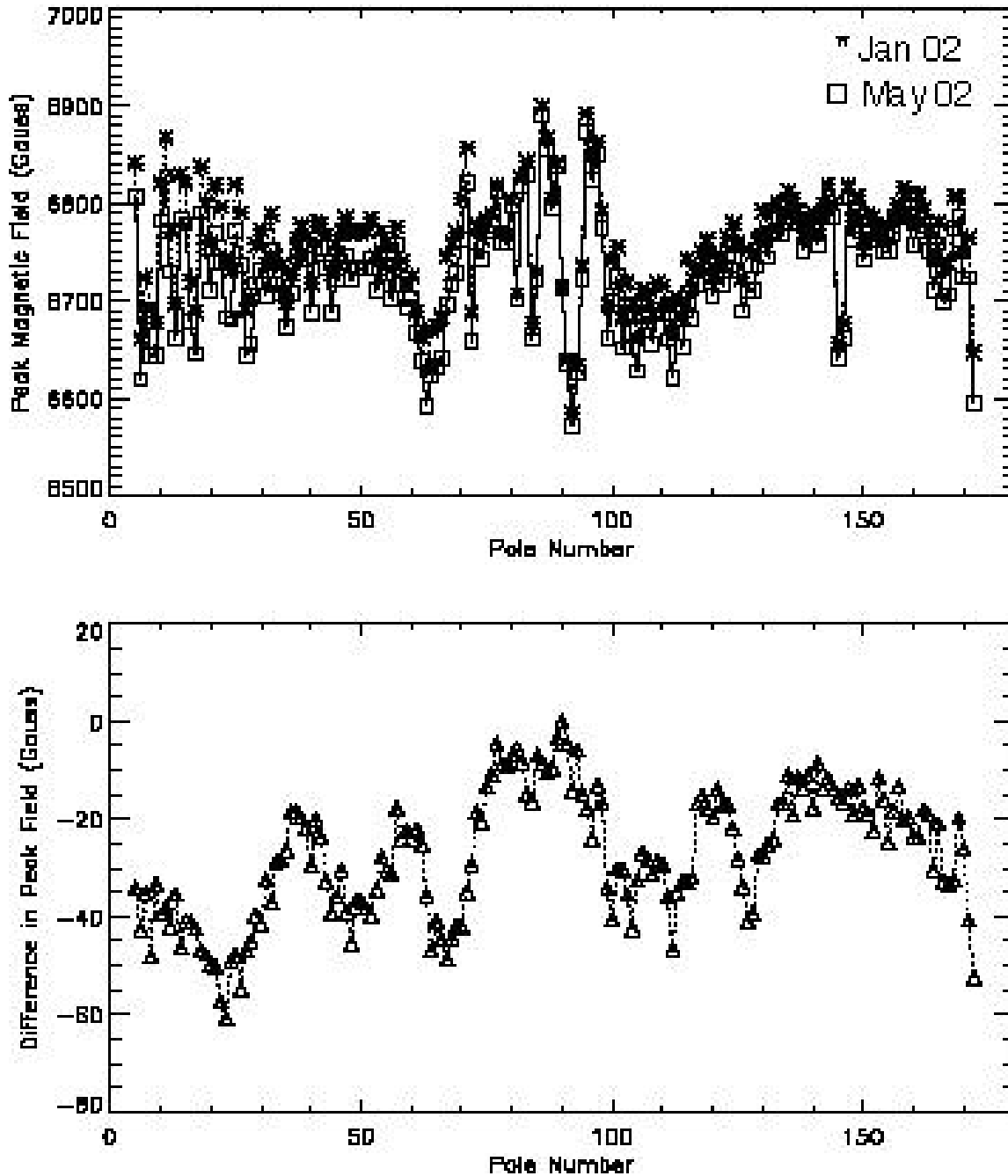
Fig. 2.5. Magnetic field changes in the downstream undulator in sector 3, U27#12, at 10.5 mm gap. The top panel shows the peak magnetic field under each pole as measured in Jan. 2002, after the device had been retuned, and in May 2002. The bottom panel shows the difference in the magnetic field. (The data for the weaker end poles are omitted.) The damage is less than that found previously, but clearly damage is continuing.

63

Two other IDs were also removed in May 2002 for checking. One was found to be slightly damaged, as can be seen in Fig. 2.6. The other does not show radiation damage (Fig. 2.7), though there is a uniform increase in the strength of the magnetic field. This uniform change in the field can be attributed either to the fact that a smaller Hall probe was used that averages the peak field over a smaller area, thereby giving a higher peak reading, or to backlash in the gap-setting mechanism that was not properly removed.
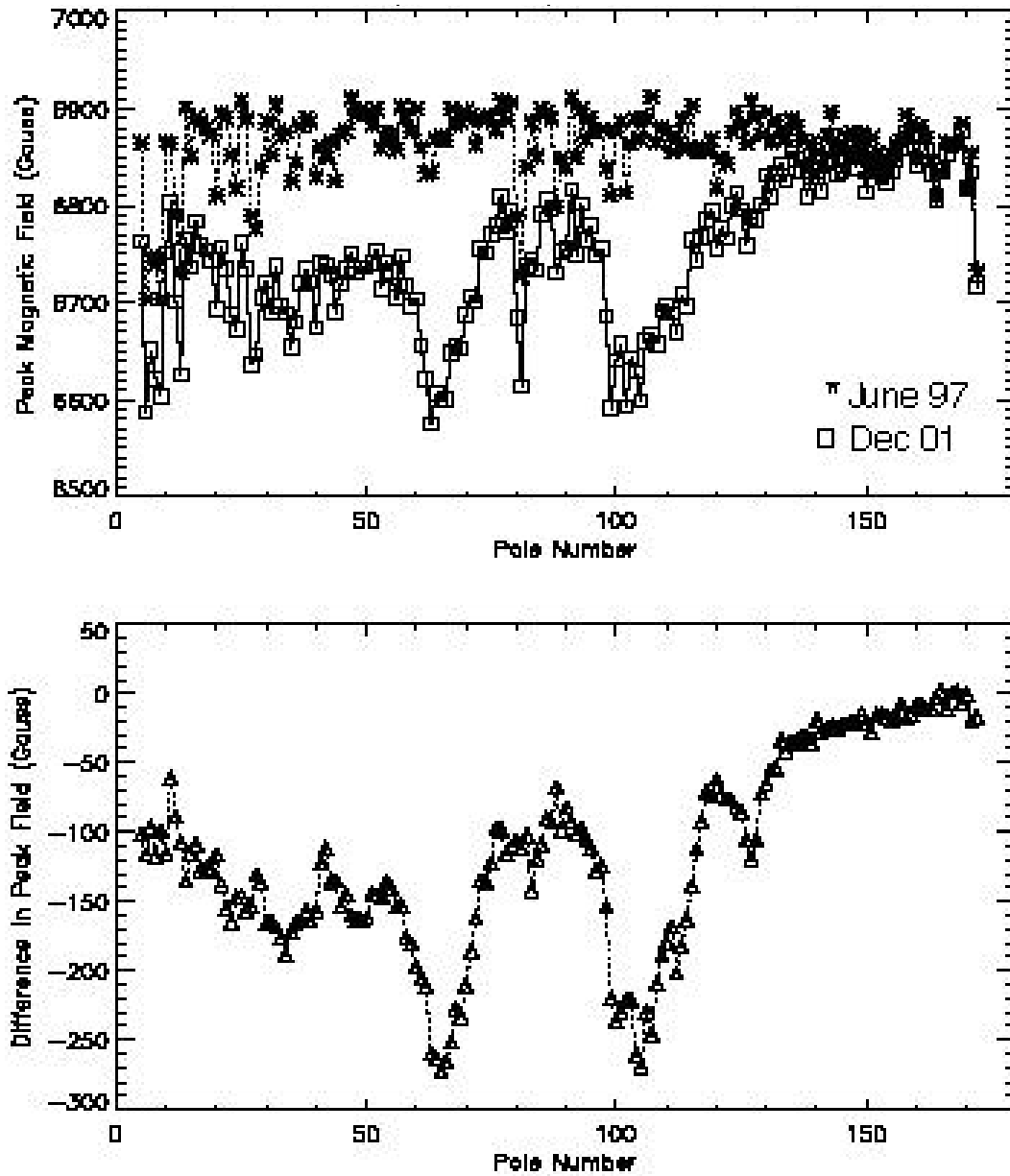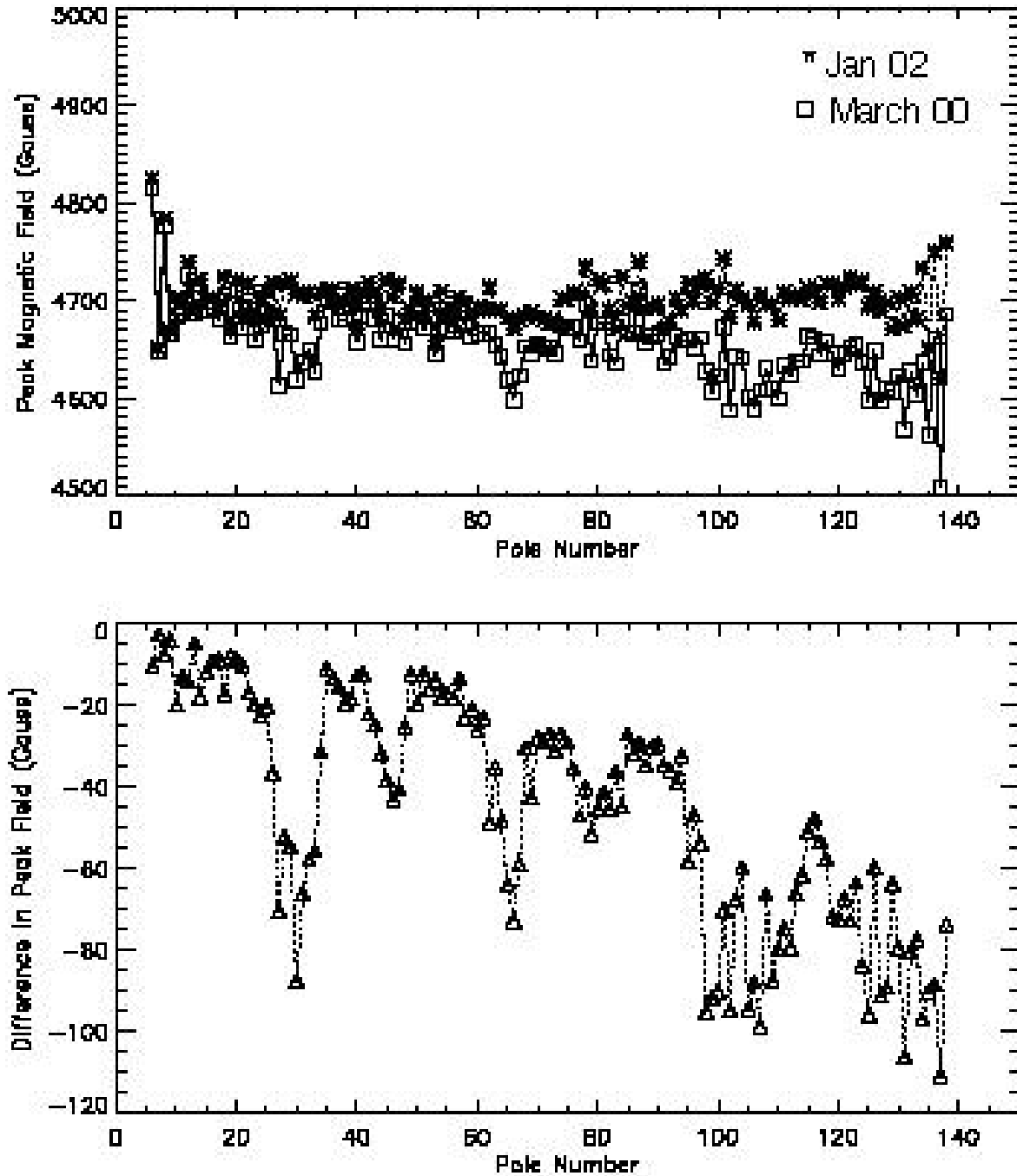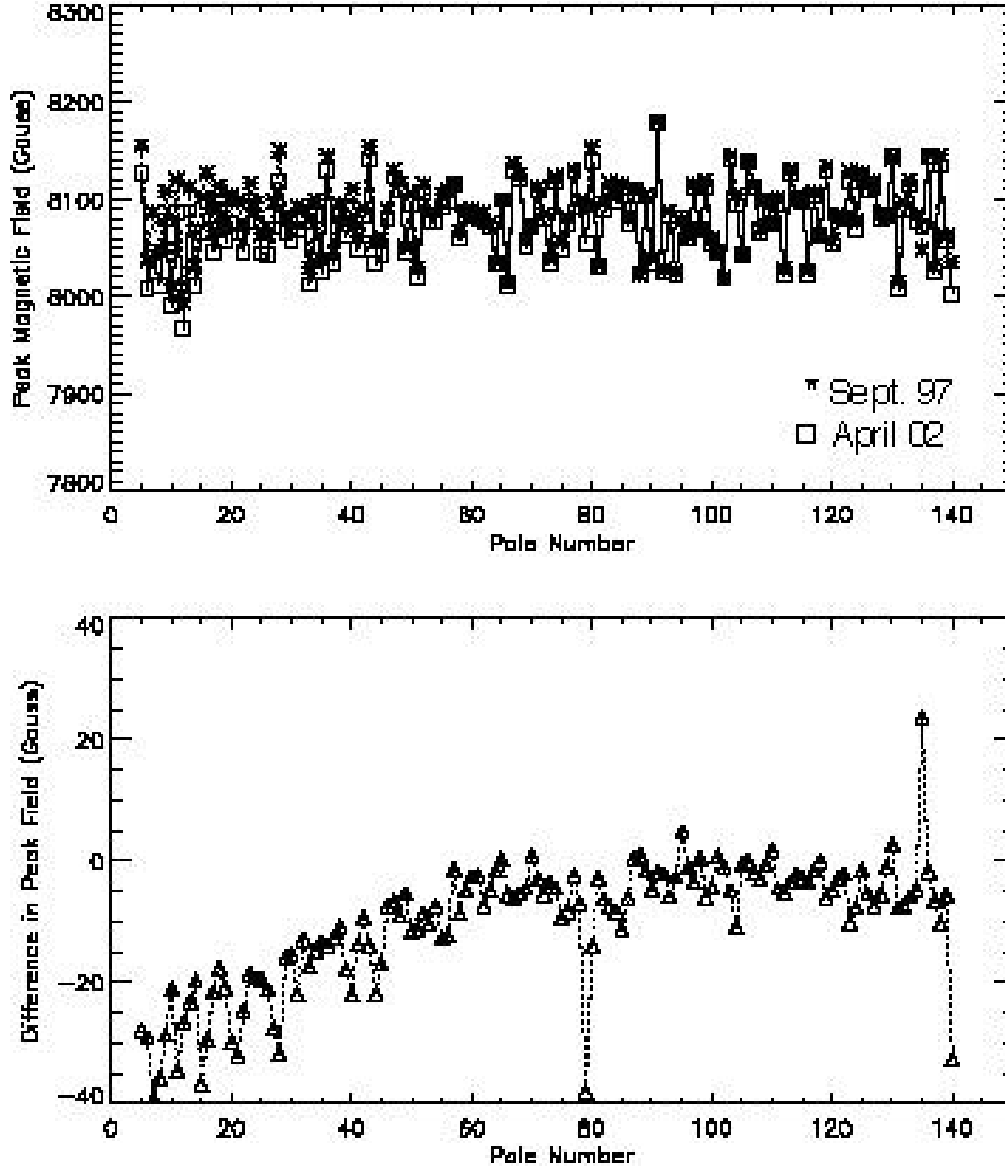

Fig. 2.6. Magnetic field changes in the downstream undulator in sector 1, U33#15, at 11.5 mm gap. The top panel shows the peak magnetic field under each pole as measured in Sept. 1997 and in April 2002. The bottom panel shows the difference in the magnetic field. (The data for the weaker end poles are omitted.) A slight decrease in field strength can be seen at the left, the downstream end.
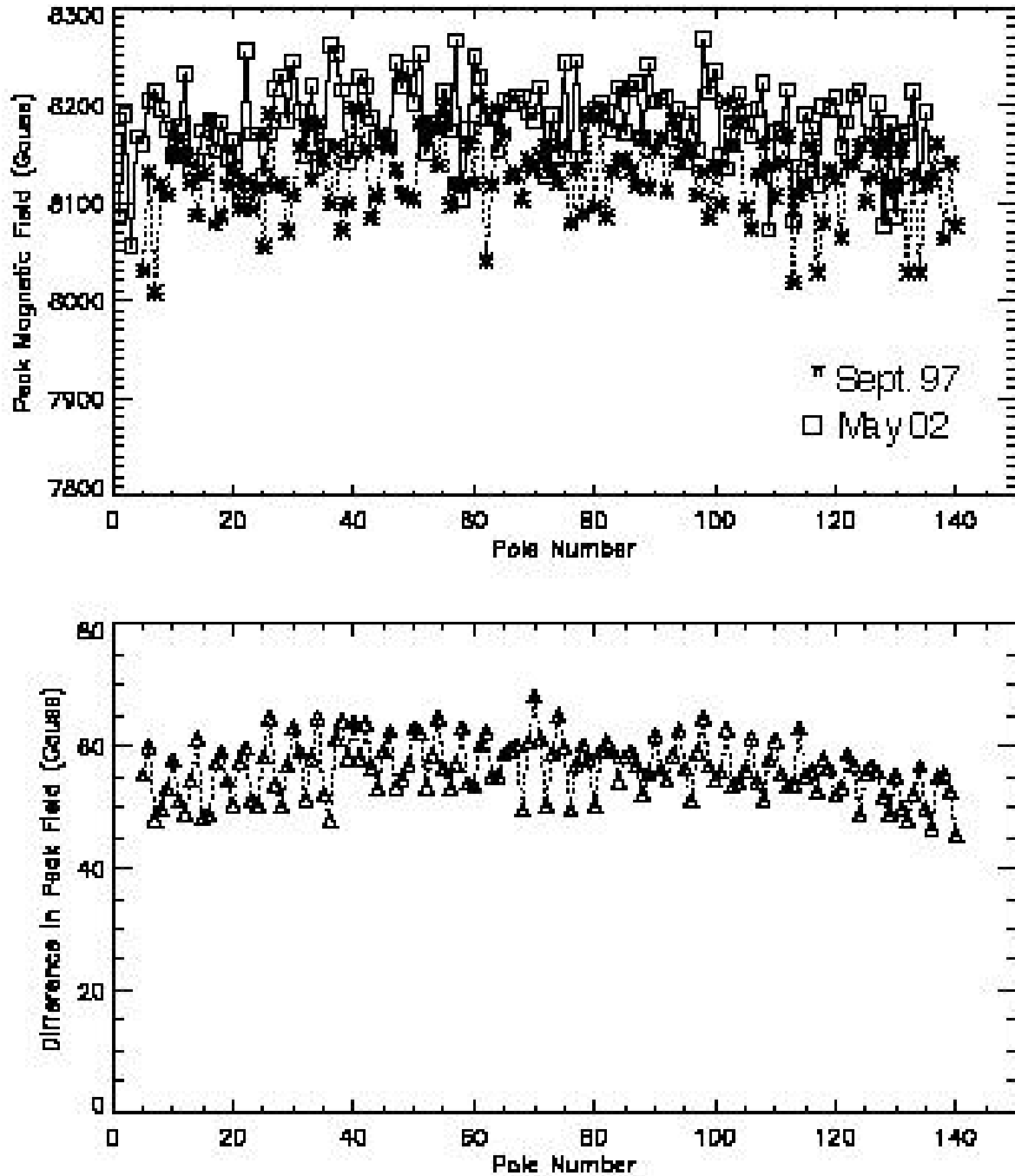
Fig. 2.7. An undamaged undulator! Magnetic field changes in the downstream undulator in sector 15, U33#3, at 11.5 mm gap. The top panel shows the peak magnetic field under each pole as measured in Sept. 1997 and in May 2002. The bottom panel shows the difference in the magnetic field. (The data for the weaker end poles are omitted.) There is no effective tapering of the field strength as was seen in the damaged devices. The overall increase in the field strength can be attributed to either a smaller Hall probe that integrates over a smaller region, thereby giving a higher peak field, or to improper removal of backlash in the gap-control mechanism.

The damage that can be seen in Figs. 2.3 – 2.6 includes, as a significant part, an effective taper in the magnetic field. Such a taper increases the rms phase errors and has a strong effect on the brilliance in the higher harmonics. Table 2.1 below shows the rms phase errors measured for each of the undulators initially, after the damage was observed, and after the device was retuned. An important part of the retuning consisted of altering the zero positions on the encoder position readouts in the undulator drive system to correct for the effective taper. The amount of the mechanical taper introduced is also shown in Table 2.1. The third harmonic of the undulator radiation, as calculated from the measured magnetic field, is given in the table as a percentage of the ideal intensity that would be obtained from a perfect undulator. (The original undulator specification aimed at having the third-harmonic intensity be at least 70% of ideal.) The radiation damage seen in the two undulators in sector 3 had a particularly strong effect on this third-harmonic intensity. The magnetic tuning was not able to remove all the damage from the downstream undulator. Instead, more extensive repair to this undulator will be needed.

Table 2.1. rms phase errors for specific undulators initially, after observed damage, and after retuning.

U27#12	Gap 10.5 mm		Sector 3 DS
Date	RMS Phase error	3rd harm., % of ideal	comment
1997 June 23	5.45	82.6	reference
2001 Dec. 31	36.5	35.2	damaged
2002 Jan. 3	9.29	69.0	tuned, taper 0.160mm
2002 May 6	14.14	52	more damage
2002 May 7	10.81	62.4	tuned, taper 0.025mm

U33#15	Gap 11.5 mm		Sector 1 DS
1997 Sept. 9	2.88	89.8	reference
2002 May 2	5.91	82	some damage
2002 May 3	5.14	84	tuned, taper 0.040 mm

APS27#2	Gap 11.5 mm		Sector 3 US
2000 June 23	2.62	91.5	reference
2002 Jan. 8	10.79	64.2	damaged
2002 Jan. 8	3.67	86.1	tuned, taper 0.150 mm

U33#3	Gap 11.5 mm		Sector 15 DS
1997 Sept.	4.54	91	reference
2002 May	5.14	89	still OK

2.1.3 Magnetic Measurement of the LCLS Prototype Undulator

Currently, an LCLS prototype undulator is under construction. The prototype is a 3.4-m-long hybrid-type undulator with a fixed gap of 6 mm. The period length is 30 mm, and the number of poles is 226. About 450 NdFeB magnet blocks will be used for this undulator. The requirements for integrated multipole moments are not demanding for this device, but those for trajectory straightness and for uniformity of the field strength at the beam position (undulator axis) are. All magnetic blocks received from Shin-Etsu have been investigated. For some magnets, the strength and direction of magnetization of the magnet blocks were measured using a Helmholtz-coil system and were compared with vendors results to confirm the validity. Hall probe measurements were performed for all magnet blocks while they were mounted in a specially designed fixture with Vanadium-Permendur poles. The magnet blocks were sorted using these data to minimize errors.

Figure 2.8 shows the variation of total magnetization. The maximum deviation from the average magnetization was smaller than ± 0.48%, and the standard deviation was 21 gauss (0.17%). Figure 2.9 shows a histogram of the magnet population. Although these numbers well exceed the specification, we applied a simple sorting for further improvement.

As shown in Fig. 2.9, the population distribution is symmetric about the average magnetization. Therefore, we chose pairs of magnets by matching the magnets at symmetric positions. Figure 2.10 shows the matched result. The pair of magnets will be mounted opposite one another in the assembled undulator (i.e., one in the top jaw, the other in the same position in the bottom jaw). If the stronger of the pair of magnets is placed in the upper jaw for this pair, then, for the adjacent pair of magnets in the undulator, the stronger will be in the lower jaw.
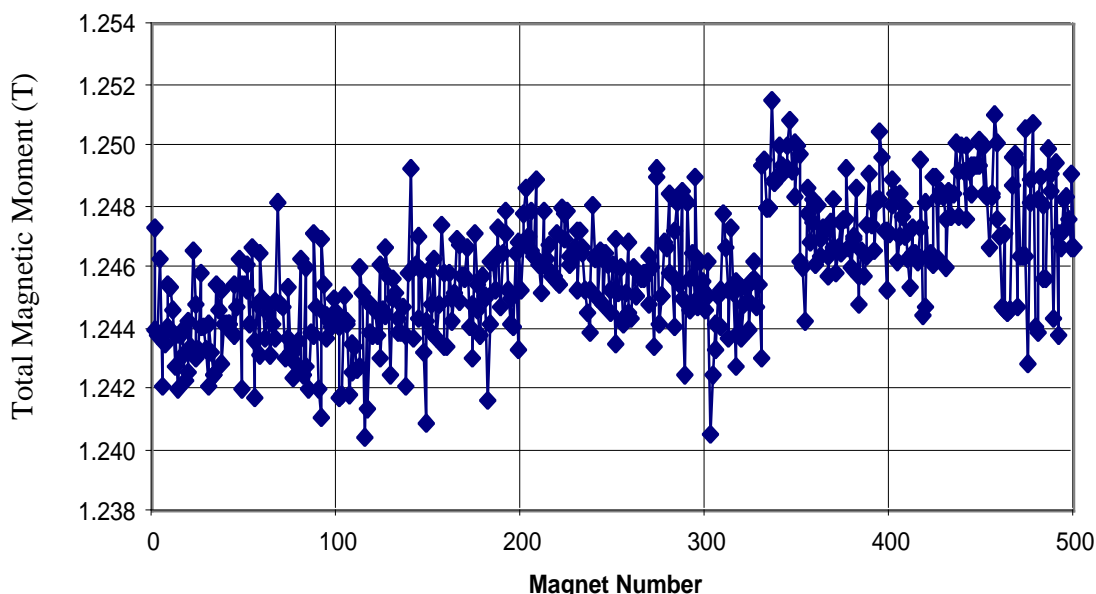

Fig. 2.8. Total magnetization as received.
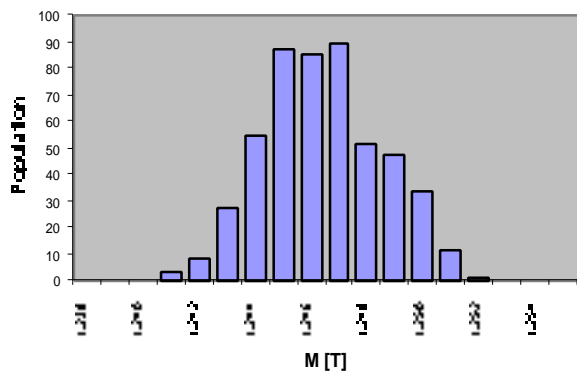
Fig. 2.9. Histogram of magnetization population.

The vertical scale of Fig. 2.10 is the same as that of Fig. 2.8 for easy comparison. The standard deviation after matching is only 1.24 Gauss (0.01%).
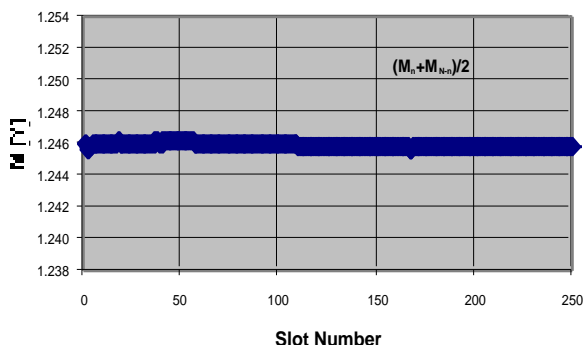
Fig. 2.10. Averaged magnetization after matching.

2.1.4 Improvements to the Magnetic Measurement Facility

The Magnetic Measurement Facility (MMF) includes systems to map the field of assembled IDs and to measure the magnetic strength of individual magnet blocks. These systems were built about 10 years ago, and some components, like computers, stepper motor controls, and analog integrators, have now become obsolete. Replacing them with fast ADCs, servomotors and up-to-date computers allowed improvement of the measurement capability while dispensing

with long power cables whose excessive noise interfered with the measured signal. New control programs allow more sophisticated data analysis and representation and a more convenient user interface. The upgrade will increase the reliability and ease of maintenance, and aid future developments and possible duplication in other projects.

Stretched Coil Measurement System
A stretched coil that can be rotated or translated is used for precise measurements of magnetic field integrals and multipole components of different types of IDs (Deriy et al., 2001). In the new system, a fast ADC is used to acquire about 1000 data points per coil turn. This allows for more detailed analysis and better accuracy than the previous four points/turn. Error sources present in the coil signal, such as coil vibrations, can now be analyzed. Other changes were to reduce the number of crates and to move data acquisition and control into the computer case. The computer runs the Linux OS instead of Windows, which allows standard APS software modules to be adopted. The data format used widely at the APS, SDDS, is now used for the acquired data.

In the new system, a translation mode of measurement can be used to measure the integrated multipole components of the magnetic field more quickly than the previous rotation mode. There is also a mode for AC field integral measurements with improved time resolution and different triggering options.

Hall Probe Measurement System
A Hall probe that is moved through the ID gap is used to measure the spatial distribution of the magnetic field. This system includes the Hall probe readout, motors for positioning the Hall probe,

position readouts, triggers, and software for processing the data and displaying the results. The updating of this system is now in progress. A significant improvement will come from the change to motors with integral controllers, because the long wires that have been a source of electromagnetic noise in the measurements will be eliminated.

Helmholtz Coil System for Measurement of Individual Magnet Blocks

The Helmholtz coil system is used for measuring the direction and strength of the total magnetic moment of permanent magnet blocks. Each magnet block that is used in an undulator magnetic structure is measured individually, and the data are used to sort the magnet blocks and determine their arrangement in the assembled device.

The controls and readout of the system have been improved. The old analog integrator was replaced by a fast 16-bit National Instruments ADC on the PCI bus. The integration is now performed digitally. The old electronically noisy stepper motor has been replaced with a servomotor that incorporates electronics for servo-loop feedback. Previously, the magnet block was rotated in 15° steps, but now the measurements are made on-the-fly with a 10 kHz sampling rate. The result is a better signal/noise ratio and more data per turn for precise digital analysis. With the first set of magnets measured after the upgrade, a reproducibility of 3 parts in 10000 was achieved.

2.2 Synchrotron Radiation Instrumentation Engineering

The XFD develops instrumentation, beamline components, and front-end components, for SRI CAT, for other CATs, and for the APS facility.

2.2.1 Front-End Design for a Canted Undulator Beamline

The XFD has designed a front end for two canted undulator beamlines from a single straight section that will allow greater utilization of the APS (see Fig. 2.11). This design will be used in three new sectors. This front end, vs. 200c, is designed to operate at a maximum beam current of 200 mA with dual 2.07-m-long undulators with a 1 mrad x-ray beam separation at 10.5 mm ID gap (K=2.8). The maximum total power on the front end is 20 kW, and the maximum peak power density is 276 $kW/mrad^2$. Many innovations were made in this front-end design to improve performance and to reduce cost. Figure 2.12 shows a model of the photon shutter (PS1 and PS2). The design was the result of optimizing the cooling and cross section to reduce the mechanical stress from thermal loading. Another redesigned component was the safety shutter. The tungsten block was changed to simplify the geometry to reduce fabrication cost. The wall collimator was also redesigned and the length reduced from 800 mm to 300 mm, which simplifies installation while maintaining adequate shielding thickness. The sizes of most in-line vacuum fittings, such as the tubes and flanges, were reduced—significantly lowering the cost. Most of the pumps are mounted in-line to increase the pumping speed. All of the support tables were redesigned using commercially available extruded aluminum bars to reduce cost.
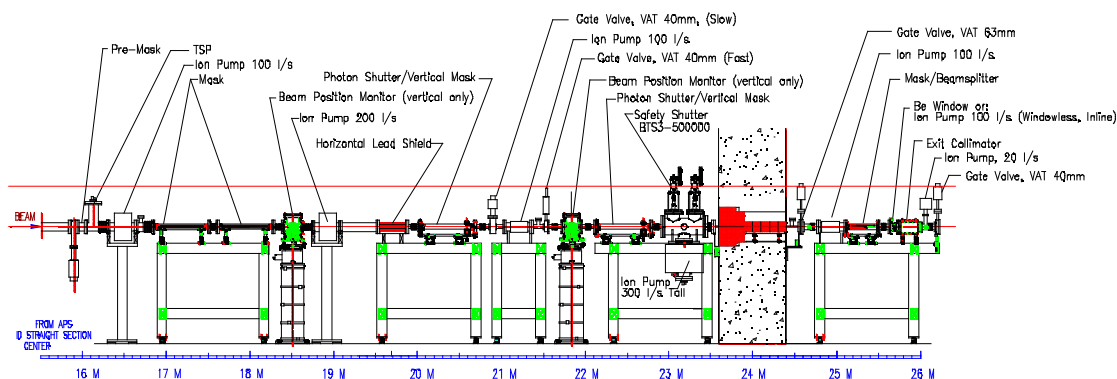
Fig. 2.11. Layout of the new front end for the canted undulator beamlines.

2.2.2 Enhanced Heat Transfer Measurements

Methods for enhancing heat transfer in cooling channels have been used and incorporated into all APS front-end (FE) high-heat-load components. In previous FE designs, porous copper mesh inserts with 76% porosity made from 8" × 8" × 0126" copper mesh were brazed into all FE photon-shutter and fixed-mask cooling channels to minimize beam-strike surface temperatures and corresponding thermally induced stresses. Although porous copper mesh inserts offered the best solution at the time, a new heat transfer enhancement technology using wire coils has been developed at the APS. Compared to mesh inserts, wire coils offer high levels of heat transfer enhancement at significantly lower sustained pressure loss. Wire coils are sized to fit snugly inside of the heat transfer testing tube. Due to the tube construction, heat flow is essentially radial, and thus the heat transfer coefficient can be directly

calculated using simple one-dimensional heat transfer equations. Figure 2.13 provides heat transfer results for various pitch 0.094" wire coil inserts; data for a standard 76% porosity mesh insert are also included for comparison. All samples were tested in the
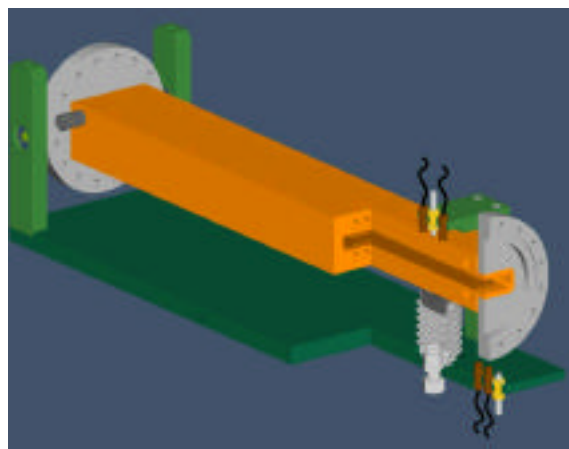
Fig. 2.12. The design of the PS1 and PS2 shutter/mask uses GlidCop beam strike plates brazed to an OFHC body. The bellows actuator eliminates the need for air cylinders with radiation-sensitive seals.

same heat transfer tube, and the results agree, within a few percent across the flow range, with the classic Dittus-Boelter relation ensuring excellent data integrity. Note that the results for the 0.094" wire coil with 0.20" pitch are very close to the standard mesh insert results. However, as can be seen in Fig. 2.14, the corresponding pressure loss results are substantially different from the mesh insert results. At comparable flow rates, the 0.20" wire coil yields nearly four times less pressure loss.

2.2.3 ID Vacuum Chamber Development and Fabrication

A family of ID vacuum chambers has been developed over the years at the APS based on extruded aluminum technology.

Chambers with an 8 mm aperture are standard at the APS, but 5 mm and 12 mm aperture chambers have also been designed. The technology has also been extended to provide chambers for BESSY II, in Berlin, Germany, for the Deutsches Elektronen-Synchrotron (DESY) vacuum-ultraviolet free-electron laser, and for the Swiss Light

Fig. 2.14. Pressure loss results for various wire coil inserts.

Source at the Paul Scherer Institute. Over the last two years, a new chamber has been designed at the APS with a 7.5 mm aperture and a revised profile that provides greater vertical clearance at the horizontal extremes of the aperture (Fig. 2.15). The new chamber should help to reduce beam loss during injection. A new extrusion has been produced for this cross section, and four new vacuum chambers are being fabricated. The end transition that is welded to the chamber was also be redesigned to allow a more gradual transition from the standard 42 mm ellipse storage ring chamber and thus reduce rf wakefield effects. The new profile chamber will be used for the insertion device vacuum chamber of the new canted undulator beamlines. The straight sections for these beamlines require chambers that include beam position monitors at the center of the chamber between the two undulators in order to decouple beam motion on the second undulator beamline from induced gap changes due to the electron beam motion of the first undulator.

Fig. 2.13. Heat transfer results for various pitch 0.094" wire coil inserts.
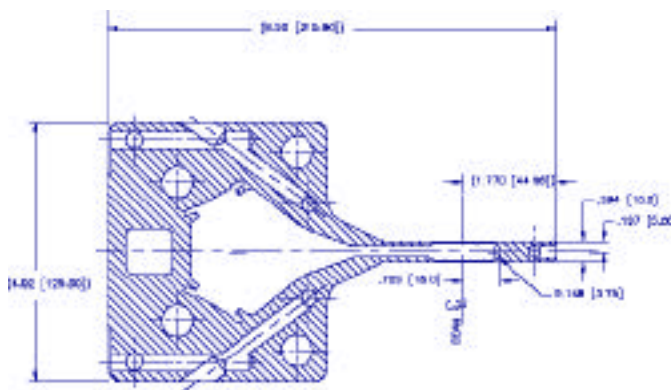
Fig. 2.15. Cross section of the 7.5-mm-aperture ID vacuum chamber. Note the oval beam aperture.

Fig. 2.16. Mono Shutter P8-70.

2.2.4 Engineering Support to CATs by XFD

In addition to internal support for SRI CAT, XFD provides design engineering support to other CATs around the storage ring. Typically, this support is for the mechanical design of new standard components or the thermal and stress analysis of existing components.

A major new design was a new mono shutter for the IMM CAT beamline including design changes on the existing hutch to accommodate the shutter. The shutter was designed as a compact unit (Fig. 2.16) capable of providing users with the means of shutting off the beam in multiple secondary beamlines that are at different angles to the primary beamline.

2.2.5 Undulator Mechanical Design

One of the consequences of the reduction in the number of poles that characterizes the canted undulator design is a change in the way that ID strongbacks deform under the influence of the attractive force. This in turn influences the magnetic field. In order to

better understand the impact of the reduced number of poles on the strongback, an extensive static deformation analysis of the strong-back was performed (Fig. 2.17).

The results of the calculations (Fig. 2.18) indicate that removal of 10 poles on each side of the strongbacks affects gap height in two ways. First, the maximum reduction in gap height reaches twice the value of the gap reduction calculated for the original 144 pole structure but is limited to the central portion of the strongbacks. Second, the ends of the 124 pole strongbacks deflect in the opposite direction than do the ends of the 144 pole strongbacks, and gap height increases towards the ends of the strong-backs. Although the shape of elastic line is changed and the extent of deformation doubles for both 124 pole upper and lower strongbacks, the changes in gap height do not exceed 0.15% of its nominal value. We believe that careful magnetic tuning can eliminate the influence of the strongback deformation on the magnetic field.

2.2.6 LCLS Assembly

The XFD is building the prototype undulator for the LCLS project (Fig. 2.19). The LCLS is a proposed fourth-generation light source that will be located at the Stanford Linear

a) 124 pole structure, no stiffeners

Fig. 2.18. Gap change due to the deformation of strongbacks.

b) 124 pole structure with stiffeners
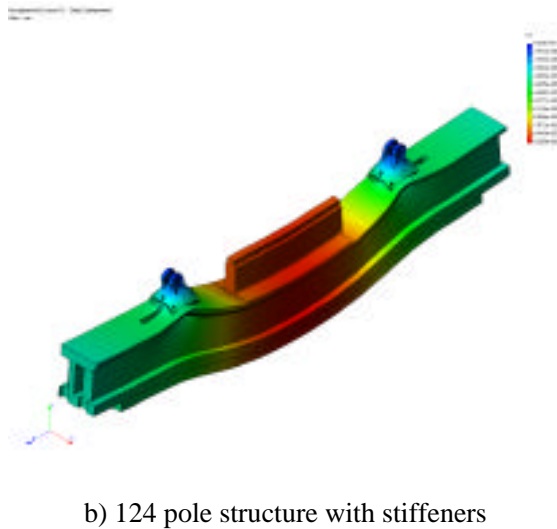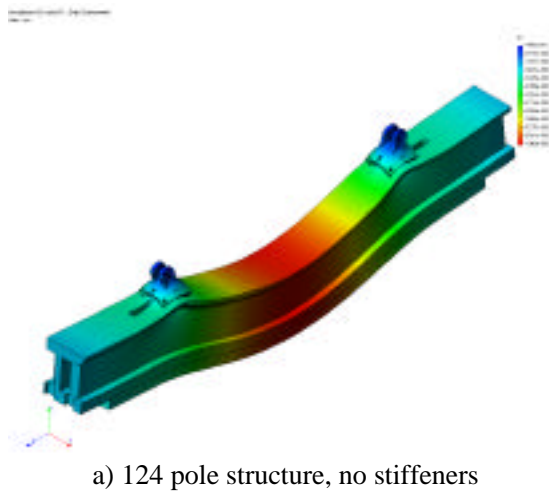
Fig. 2.17. Y-direction deformation of the upper strongback.

strongback is fabricated out of a solid piece of titanium. In addition to its strength, titanium has a low coefficient of thermal expansion. To complete the 3.0-cm-period device, 452 vanadium permendur poles are needed. Upon completion, the poles undergo a thermal stress relief and are individually measured and sorted to adhere to the +/- 3 micron nearest-neighbor pole-gap specification. Likewise, the 450 neodimium iron boron magnets are individually measured to determine the magnetic properties and then sorted. The device is adjusted in both the horizontal and vertical planes using a novel cam-type design whereby servomotors rotate the cylindrical strongback in a specific sequence to achieve the desired location.

Accelerator Center (SLAC). The 3.4-meter-long permanent magnet undulator is a fixed-gap device with a gap tolerance of +/- 6 microns. To meet this requirement, the
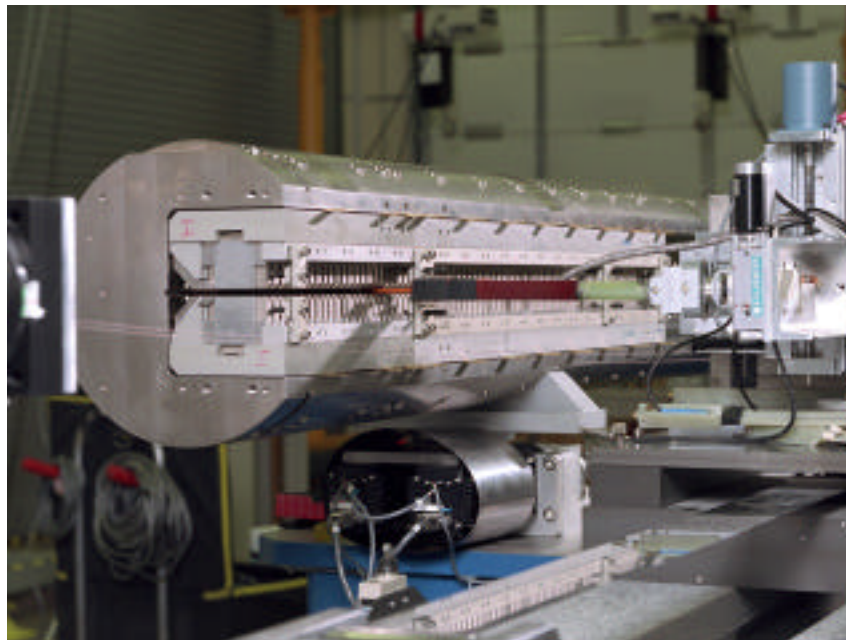
Fig. 2.19. The LCLS prototype undulator on the magnetic measurement bench.

2.2.7 4-ID-A BCTF Photon Shutter Simulation Experiments

Most of the original version 1.2 photon shutters have been in operation for over five years. However, it is very difficult if not impossible to obtain sufficient operational data to verify thermal performance due to the extreme radiation present within a front end. Surface temperature mapping in conjunction with thermocouple data is required for proper comparison with a model, but infrared imaging is not possible without destroying the camera in the process due to the radiation. Operational data are needed to determine the maximum thermal load and power density that can be tolerated, and this information is also needed to assess the expected life cycle.

To obtain operational data, a series of experiments is planned in order to simulate a range of thermal loading conditions that

might exist on version 1.2 photon shutters. The experiments will be performed in the 4-ID-A beamline components testing facility (BCTF) testing chamber using two primary test pieces. Each test piece will be identical in cross section to the beam strike surface of the version 1.2 photon shutter—but will be much shorter in length. One test piece will contain standard brazed copper mesh inserts, and the other will have open channels. This will bracket the range of heat transfer coefficient values that might exist in operation. The test pieces will be individually mounted, one at a time, inside the BCTF chamber on X-Y-Z stages and a rotational stage in order to precisely control the position and angle of the beam strike surface relative to the beam. Each test piece will be instrumented with a series of thermocouples positioned under the beam strike surface. A large sapphire window will be mounted on the BCTF chamber that will allow direct viewing of the beam strike surface using an infrared camera.

Simultaneous thermocouple data and infrared data will be collected over a range of beam conditions for each of the two test pieces. Coolant water flow rate and enthalpy data for each of the individual coolant channels within the test pieces will also be collected. Valves will be incorporated on each coolant channel's return lines so that the coolant flow rate can be individually set for each channel.

Figure 2.20 shows a cut-away view of the BCTF chamber with the test piece installed. Note that the centerline of the shaft coupling the test piece to the stages corresponds to the beam strike surface, thus the test piece can be rotated with respect to the beam and the beam position will not move with respect to the surface location. Data can be collected for a series of different rotational angles, yielding different power loading conditions, without requiring repositioning of the test piece. This allows for rapid, repeatable data collection over a range of conditions.
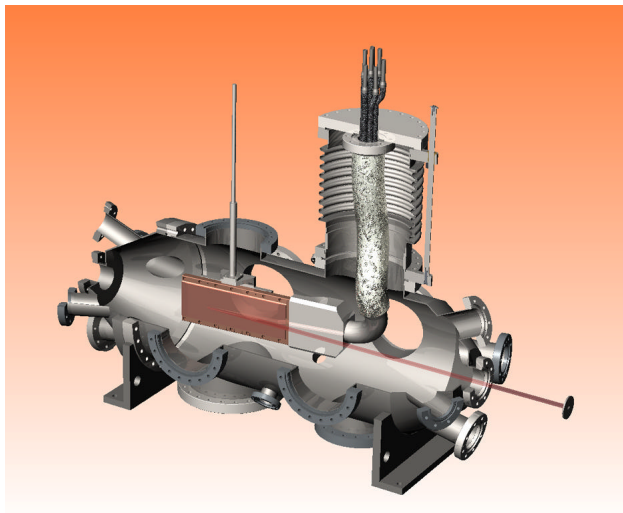
Fig. 2.20. Cut-away view of the test piece for the photon shutter simulation experiments.

In addition to these experiments, spare version 1.2 P1 and P2 blades have been fabricated for the purpose of exchanging these blades with operational shutter blades that have experienced severe duty. Metallurgical examinations will be performed on the blades in order to assess damage in the beam strike zones. This will be the first time that photon shutter blades have been available for metallurgical examination. Photography, stereo microscopy with high-resolution digital imaging, and high-resolution metallography can determine if there is a problem that warrants destructive testing. Examining these shutter blades will develop a procedure for testing present and future front-end high-heat-load components.

2.2.8 Software Development

Significant advances have been made in the integration of all steps of a tomography experiment into a single user interface. An easy-to-use, robust user interface has been developed to allow users to "pre-program" the steps necessary to acquire a complete set of tomographic data. Once set up, the data-acquisition process can continue to completion without further user interaction. This step alone has significantly decreased the time required to acquire a complete set of data.

In addition, initial steps have been taken to integrate the preprocessing and reconstruction steps into the same interface. The ultimate goal is to provide the user a single interface through which they can control the many machines and processes required to complete a tomographic experiment.

A stand-alone Linux cluster for parallel processing has also been successfully implemented. A small subset of users routinely use this parallel processing cluster

to perform time-consuming calculations in a fraction of the time required on a single machine. In most cases, users can now take home their processed data within hours of the completion of their experiment rather than take it home and struggle for days to process it themselves. In the future, user interface improvements to this system will open up this capability to all users with a need for processing power.

Improvements and new features have also been added to the CCD acquisition program used by the majority of SRI-CAT users for acquiring CCD data. It is now possible for users to control cameras from five different manufacturers through the same user interface—all seamlessly integrated into the standard EPICS control system. Additional data acquisition modes have been added to make the system more useable to a greater number of people.

2.3   X-ray Optic Fabrication and Metrology

The CAT members at the APS continued to make requests for x-ray optics from the staff of the Optics Fabrication and Metrology (OFM) Group. As detailed below, these requests have come in four areas: metrology, thin film deposition, crystal fabrication, x-ray characterization, and mirror design and consulting. Recent highlights include:

- Differential deposition of gold for K-B mirrors was perfected to achieve 0.90 microrad rms deviation over 60 mm from an ideal elliptical surface starting from a spherically shaped silicon substrate.
- Fabrication of a Si crystal designed for sagittal focusing in a bender with a thickness of 0.9 mm over a diffraction area of 53 mm by 76 mm and with a

thickness variation of only 5 microns over the entire diffraction area was achieved.
- Parabolic refractory lenses made by extrusion and having a 0.2 mm wall thickness were fabricated very inexpensively and tested at 81 keV to show effective focusing. Such lenses were assembled into a variable focus unit. Subsequently lenses were obtained for which the wall thickness was reduced to 0.1 mm.
- Polishing of silicon to a roughness of 0.09 nm (rms) was accomplished in-house with chemical mechanical polishing.
- Stitching interferometry, which promises to provide precise figure error data for large mirrors over an area, was demonstrated
- A double-multilayer monochromator was made and put into service on beamline 2-BM (Chu et al., 2002).
- Etching of diamond monochromators to remove strain was found to be efficacious (Maj et al., 2002).

2.3.1 X-ray Optics Metrology Laboratory

Measurement Requests
During the last fiscal year, we handled a total of 110 metrology measurement requests out of which 56 originated from the CATs. These included beamline mirrors, multilayers optics, and mirror bender systems. Metrology requests were filled for the following CATs: BESSRC, Bio, CMC, DND, GSECARS, MHATT, SER, SBC, SGX, SRI, and UNI. Requests from non-APS users originated from SNS/IPNS, Fermi Laboratory, and others. In addition, the laboratory continues to provide measurement data to the OFM Group's polishing facility, thus indirectly supporting the users activities. Such measurements are

also used to monitor and improve our polishing capability, which equally benefits the APS users.

Instrumentation Upgrades and Developments

With the advances in synchrotron radiation sources and research, tolerances on x-ray mirror quality are becoming tighter. There is now demand for mirrors with surface roughness and slope error on the order of 1 Å rms, and 1 μrad rms, respectively. Metrology of mirrors with such a tolerance level is expected to be challenging, particularly with respect to the APS long trace profiler (LTP II), which has a sensitivity that is limited to 0.5 μrad. Moreover, one of our major ongoing efforts relates to the development of an elliptically shaped K-B microfocusing mirror using a differential deposition technique (Ice et al., 2000). The LTP II data continue to be essential in the optimization of the shape and thickness of the differentially deposited films on K-B mirror substrates. Progress towards achieving diffraction-limited focusing will require even highly optimized differentially deposited thin film. This, along with efforts in developing coherence preserving optics, will likely push the measurement accuracy far below the limits of our current LTP. Therefore, a number of steps are being considered to enhance the instrument performance. One of the most crucial optical components is the Fourier transform (FT) lens. The existing FT lens suffers from aberration impacting the accuracy of measurements, particularly those concerning strong aspheric surfaces. We are pursuing obtaining an improved lens for the LTP. Since K-B mirrors are generally much shorter than regular x-ray mirrors, a compact LTP is being constructed. The ultimate resolution is expected to be better for the smaller unit.

Development of a Stitching Interferometry System for Large X-ray Mirrors

To enhance the metrology measurements and complement the LTP II instrument, a stitching interferometry system for evaluating large x-ray mirrors is being developed in collaboration with Michael Bray at MB-Optique Inc, (Assoufid et al., 2002a). The system has the potential of providing a full 3-D surface profile with nanometer resolution, and the data can be used, for example, to provide feed back for surface error correction during mirror polishing. The data can also be used for simulation purposes.

The system is being developed around an existing laboratory laser interferometer (a WYKO-6000 surface profiler), a 1-m-long high-accuracy translation stage/rail, a tilt platform, a mirror mount system, and the stitching computer code provided by M. Bray.

The measurement procedure consists of acquiring N overlapped subaperture measurements until the whole mirror surface is covered. At the end of the measurement sequence, the full 3-D surface is constructed by stitching together the submeasurements, using the stitching computer code.

Preliminary tests were performed on an actual silicon beamline mirror. The measurement required eight subaperture measurements with 41% overlap between adjacent subapertures, and each subaperture represented an average of ten phase measurements. Table 2.2 compares the resulting surface slope error value with that obtained with the LTP II. As one can see, the rms slope error values are in close agreement, but there is a large discrepancy in the peak-to-valley values, which is due to

Table 2.2. Comparison between LTP II and stitching interferometry data obtained on a silicon mirror over a 750-mm-long scan length. (Note that the LTP II data are the result of a one-dimensional trace along the mirror axis, while the stitching data are the result of measurement of a surface 750 mm long by 40 mm wide.)

Instrument/Measurement Technique	rms Slope Error (µrad)	Peak-to-Valley (µrad)
LTP II	2.0	11.2
Stitching Interferometry	1.6	70.3

a bad pixel in the stitched profile, thus giving an exaggerated peak.

With this work, we demonstrated that the technique can be easily adapted for evaluation of large synchrotron radiation mirrors, and the preliminary results were encouraging. However, there are still a few sources of errors that must be tackled in order to obtain reliable, large field-of-view images with the desired accuracy. These sources of errors pertain mainly to temperature control and system calibration. We are currently actively working on implementing the necessary improvements.

Applications of the Atomic Force Microscope

The atomic force microscope (AFM) has proven to be a very useful metrology tool and is now routinely used. The PSD data derived from the AFM topography measurements are very useful for comparison with those obtained from x-ray scattering measurements. A variety of samples were characterized for the users during the last fiscal year. These include thin films (Satyam et al., 2001), patterned deposition of metallic nanoclusters (Divan et al., 2001), zone plates, and superpolished silicon substrates.

Investigation of Polished Silicon Substrates Using X-rays

In addition to metrology at optical wavelengths, we began using x-rays as a means of characterizing polished substrates destined for x-ray use. The focus was essentially on silicon surfaces prepared in the OFM Group polishing facility. The intent of this work was to quantitatively assess the nature of the power spectrum of the surface as measured by x-rays and that would influence the x-ray scattering properties of optics made using such surfaces. To this end, x-ray scattering measurements were conducted at the C station of 1-BM beamline on three polished silicon samples with nominal roughness of 0.9, 1.6, and 10 Å rms, respectively, as measured using our WYKO TOPO-2D. Figure 2.21 shows the AFM surface topography images for the three silicon substrates. This study showed that the power spectra derived (see Fig. 2.22) from x-ray diffuse scattering data agree reasonably well with those obtained from the AFM surface topography measurements. The data also showed features with a size comparable to that of the colloidal particles used for polishing (65 Å) (Assoufid et al., 2002b).

a)
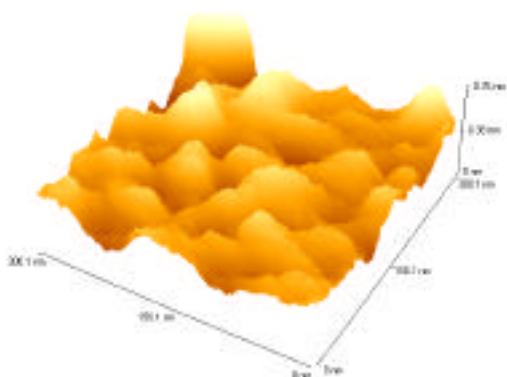
b)
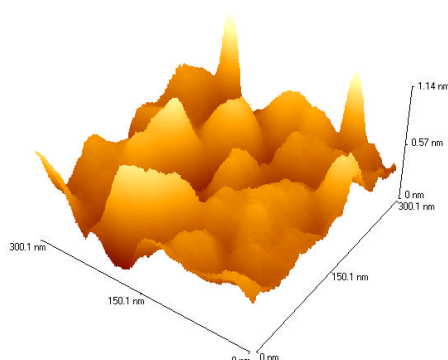
c)
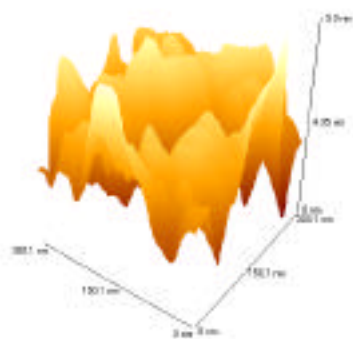
Fig. 2.21. Atomic force microscopy surface topography of three silicon substrates polished at the OFM Group facility. The three substrates have a surface roughness of a) 0.9, b) 1.6, and c) 10 Å rms, respectively, as measured with the WYKO TOPO-2D.

2.3.2 Deposition Laboratory

We have filled deposition requests from users including over 200 regular depositions and more than 450 mirrors and experimental samples since September 2000. Kirk-partrick-Baez grazing-incidence mirrors and multilayer x-ray optics are routinely fabricated at the deposition lab. Coatings for SRI-CAT x-ray lithography experiments are made in large quantities.

Graded Multilayers

Continuous efforts in laterally graded multilayers have been made after the initial success in tunable x-ray double-monochromator applications (Liu et al., 2001). Graded multilayers can now be grown in both the large and the small deposition systems. Using the large deposition system, the grading length can be expanded to 6 inches. Recently we have used the large deposition system to make graded multilayers for x-ray fluorescence detection applications. Figure 3.23 shows the measured d spacing and reflectivity as a function of lateral distance along a W/C graded multilayer made for Bio-CAT. The measurements were done at 6.5 keV on the Bio-CAT undulator x-ray beamline (via K. Zhang of Bio-CAT). The multilayers consists of 60 bilayers of a uniform W layer and a wedge-shaped C layer grown on a 100 mm × 100 mm × 2 mm Si substrate with a 0.7 nm rms roughness.

Selective Profile Coating/ Differential Deposition

Our experience in graded multilayers has been expanded into coating films with other selective thickness profiles. One application of this technique is to convert a cylindrical mirror to an elliptical one by differentially depositing Au films. In this application, a desired surface profile after Au coating on a cylindrical mirror should be the ideal surface

figure of a focus ellipse. In the selective profile coating, the sputter source power is kept constant while the substrate is passed over a contoured mask at a constant speed. The mask is placed very close to the substrate level (within ~1.5 mm) on a shield can over the sputter gun (see Fig. 2.24). To determine the shape of the contour, we first measured the Au thickness distribution above the sputter gun at the substrate level. Figure 2.25 shows such a distribution of a Au film on a 4-inch-diameter Si wafer measured by using an ellipsometer. The growth was done without any masks nor

substrate movements. The units in Fig. 2.25 are angstroms for the vertical axis and cm for the horizontal axes. The center directly above the target shows the largest thickness, as expected. A model has been developed to fit the measured thickness distribution for this stationary growth. The relative thickness weightings are then digitized at every point 1 mm apart for an area of 76×152 mm^2 directly above the sputter gun at the substrate level. When the substrate is moving across the shield can, the film
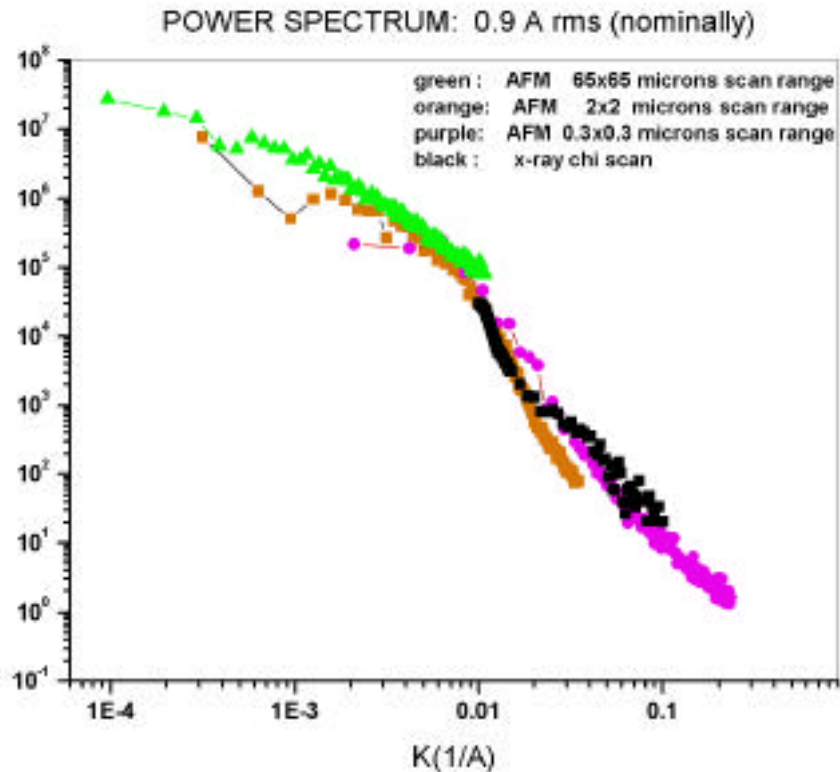

Fig. 2.22. Power spectral density (PSD) curve obtained from x-rays and AFM for 0.9 Å superpolished silicon.
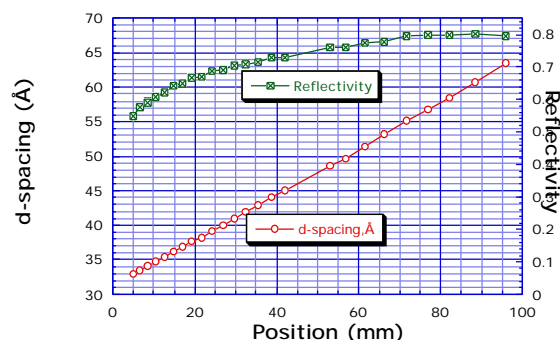
Fig. 2.23. Measured d spacing and reflectivity as a function of position along a W/C graded multilayer made for Bio-CAT. The measure-ments were done at 6.5 keV on the Bio-CAT undulator x-ray beamline (via K. Zhang of Bio-CAT).

thickness is directly proportional to the length of the opening on the can. By equaling the summation of relative weighting to the required relative thickness, a contour can be obtained for a desired thickness profile. A desired profile for changing a 90-mm-long cylindrical mirror into an elliptical one is shown as the "initial" required thickness in Fig. 2.26. With the contoured mask in place, a film with the desired thickness profile can be grown by passing the substrate over the mask during the deposition. By adjusting the speed and the number of passes of the substrate, a desired total film thickness can be achieved. The results to date have been encouraging.

After only one deposition, the surface figure of the mirror was already close to that of an ideal ellipse. As judged by LTP measure-ments, the difference from the ideal ellipse is shown in Fig. 2.26 as the required thick-ness "after one deposition." For over a 30 mm length, the mirror had a figure error of 0.47 microrad from an ellipse. This is beyond the known state-of-the-art which is 0.69 microrad over 20 mm. Very recently we have been able to extend this result to
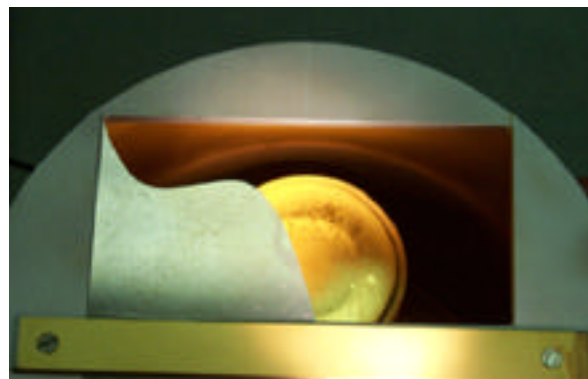
Fig. 2.24. A mask placed on top of the shield can above the Au target to achieve a desired Au thickness profile on a cylindrical mirror for ellipse focusing. The opening on the can top is 3" × 6". The 90-mm-long mirror was placed on a carrier with one end aligned to the far-left side of the mask and the other end towards the center. During the deposition, the mirror was moving across the mask so that the end which moves across the center receives the thickest deposition.

longer lengths and have acheived 0.90 microrad rms over 60 mm.

System Improvements

We have improved the large deposition system and maintained the facility in good working order. The shielding cans for all four sputter guns have been redesigned so that 6-inch-wide substrates can be coated in the large deposition system. The previous limit was 4 inches. We improved the transport system in the large deposition system by adding a cable-separator so that the previously crossed pulling cables no longer interfere with each other.

The ellipsometer has been upgraded so that automated measurements can be performed on 4" × 4" samples to obtain a film thickness profile. A Specs ion sputter-cleaning gun has been added to the large deposition system. It is useful for modifying the surface structure of a sample.
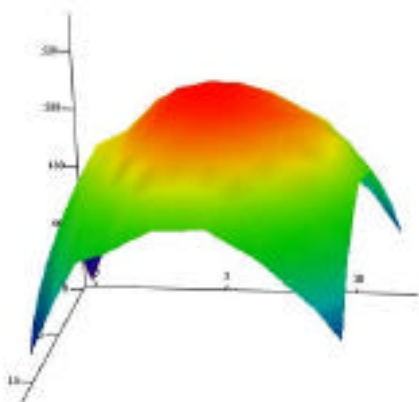
Fig. 2.25. Thickness distribution obtained from ellipsometer measurements of a gold film on a Si wafer placed directly above the Au target. The units are angstroms for the vertical axis and cm for the horizontal axes.

2.3.3 Fabrication Laboratory

The optics fabrication laboratories are the leading suppliers of x-ray difractive optical elements for APS beamlines. For the period of June 2000 – April 2002, 510 optical elements made of Si, Ge, Sapphire, MgO and different type of glasses have been fabricated. Elements were fabricated for other research centers as well, such as UOC, SNS, NWU, NIST. For example, a cryocrystal was made for Bio-CAT and for SBC. Both (111) and (100) versions have been fabricated and delivered.

Purchasing, installation, and learning how to properly operate the K&S Dicing saw was notable. It enhanced our capabilities for more precise cutting and dicing slabs and microstructures up to 5 mm thick and 200 mm in diameter. By using the unique technical capabilities of this cutter, we have fully fabricated six silicon and germanium substrates for x-ray analyzers. The machine is being widely used for fabrication of precise optical elements based on thin crystalline and glass substrates.
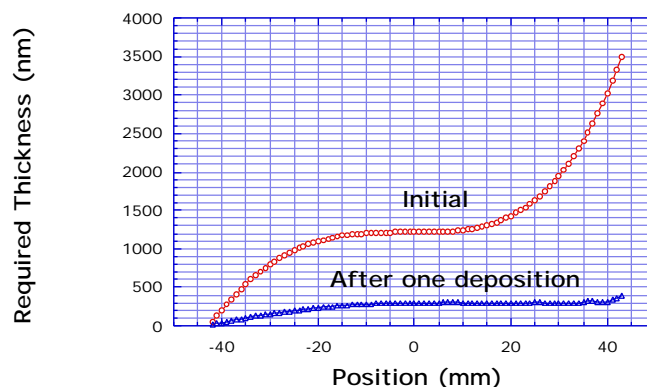
Fig. 2.26. Required thickness profile to achieve an ideal ellipse surface profile according to LTP measurements.

Preparation of ultrasmooth surfaces is one important issue for the fabrication of refractive x-ray optical components for synchrotron radiation instrumentation. In order to fabricate ultrasmooth surfaces in-house, some R&D projects have been carried out:

- A semiclean polishing laboratory, with three types of polishers, including a polisher with chemical-mechanical polishing (CMP) capabilities is now totally functional. We have purchased a Zeiss microscope for visual characterization of surfaces between polishing stages.
- A review of recent publications on fabrication of ultrasmooth surfaces has been shown that CMP is currently the best technique for this purpose. The most common polishing compounds being used for CMP processes are different types of colloidal liquids, but still there are not enough research results to fully understand the polishing mechanisms in many cases.

In order to obtain some ideas of how colloidal particles work in the polishing processes, we have chosen three type of

commercially available slurries and analyzed them to get information about their chemical contents. Important from the point of view of polishing results is that none of these compounds contains chemicals that can etch silicon or germanium in free forms. A review of recent publications on the chemistry and technology of colloidal polishing compounds in combination with our experimental results allowed us to better understand the process and mechanism of CMP. By solving many other technical and technological problems and by applying a float polishing technique, we have been able to develop in-house the technology for ultasmooth polishing of silicon and have reached a 1 Å rms finish. However, we still have a lot to do towards fabrication of smooth and flat optical elements, and we are continuously working on development of better technologies for fabrication of x-ray optical elements.

Recently, fabrication of a Si crystal designed for sagittal focusing in a bender with a thickness of 0.9 mm over a diffraction area of 53 mm by 76 mm and with a thickness variation of only 5 microns over the entire diffraction area was achieved.

2.3.4 X-ray Characterization Laboratory

In accordance with its mission, the x-ray laboratory has served the APS users by offering them opportunities to test their crystals or thin layers deposited on different substrates. A single-axis diffractometer, a Laue camera, and a double-axis diffractometer (all installed at conventional x-ray generators—Rigaku and Spellman) were used to obtain the crystallographic orientation and/or to test numerous crystals. The instruments were available to all authorized users. However, most of the

efforts in the x-ray lab were connected with diffractometers installed at the rotating anode generator, i.e., with the Topo Test Unit (TTU) and the triple-axis diffractometer.

In the past two years, a total of 122 crystal tests were performed with the use of the TTU. Of those, 90 tests were for silicon [predominantly monochromators and analyzers manufactured by the former User Program Division (UPD), and sometimes ingots to be used for fabrication], 4 for germanium, and 28 for diamond crystals. A majority of the tested optical elements (74) originated from XFD and UPD. However, 48 experiments were carried out for users from UNI-CAT, IMM-CAT, COM-CAT, SBC-CAT, Bio-CAT, Rockefeller University, Northwestern University, University of Illinois at Urbana Champaign, and the National Institute of Standards and Technology.

As in previous years, the triple-axis diffractometer was mostly used for reflectivity measurements (11 single- or multilayers were investigated) and for testing samples that were later used at the beamlines (about 12 different samples were checked).

Parallel to serving users, a major effort to rebuild and modernize the TTU was undertaken, including having easily exchangeable CCD and scintillation detectors, improving sample crystal rotations, and improving changing of monochromators.

2.3.5 Refractory Lenses

Focusing or collimating diverging x-ray beams produced by synchrotron sources is necessary in a range of applications. This can be achieved by using mirrors, crystals, zone plates, capillaries, and more recently

by using a compound x-ray lens (CXL), proposed a few decades ago and more vigorously pursued since the mid-1990s.

With the reduction to practice of CXLs in the mid-1990s and the general realization of their usefulness, a number of attempts have been made to manufacture such lens arrays in a variety of suitable materials and configurations.

Recently, the APS has developed parabolic lenses in aluminum using microextrusion technology. With this technique, we are able, for the first time, to generate miles of x-ray lenses at a very economical cost and with reasonable precision. The first generation of such lenses has been designed, fabricated, assembled, and tested at the APS. Our first prototype lens of this kind is shown in Fig. 2.27.

The variable focus aluminum lens has been used at the APS to collimate a mono-chromatic, 81-keV undulator beam. Results indicate collimation consistent with theoretical expectations. At this energy, the absorption coefficient for aluminum is $\mu = 0.53976 \text{ cm}^{-1}$.

Two sets of lenses were tested on the APS 1-ID beamline. In one experiment, an upstream vertical slit was used to provide an approximately 0.6-mm-high beam at 35 m from the source where the CXL would be located. After inserting the lens, the transmitted beam through the lens was measured both 0.3 m and 24 m downstream using two vertical scans. Figure 2.28 shows the results.

The narrowing of the x-ray beam seen in both curves in Fig. 2.28 is due to two different effects. The curve for the beam at 0.3 m from the lens indicated not focusing— but the higher absorption of x-rays away from the optical axis of the lens, where the beam has to go through thicker aluminum layers. Focusing is apparent from the curve showing the measurements at 24 m from the lens. The beam is considered collimated where the two curves cross, in this case at about 160 lenses, in agreement with theory.
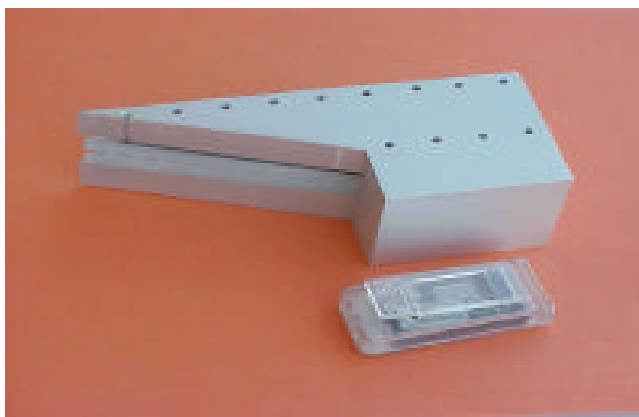
Fig. 2.27. A prototype variable focus compound x-ray lens. By moving the assembly horizontally, the incident beam from the right-hand side is made to pass through different numbers of lenses.

Vertical Beam Size at 0.3 mm (Circles) and 24 m (Diamonds)
Downstream of the Variable Focus Lens
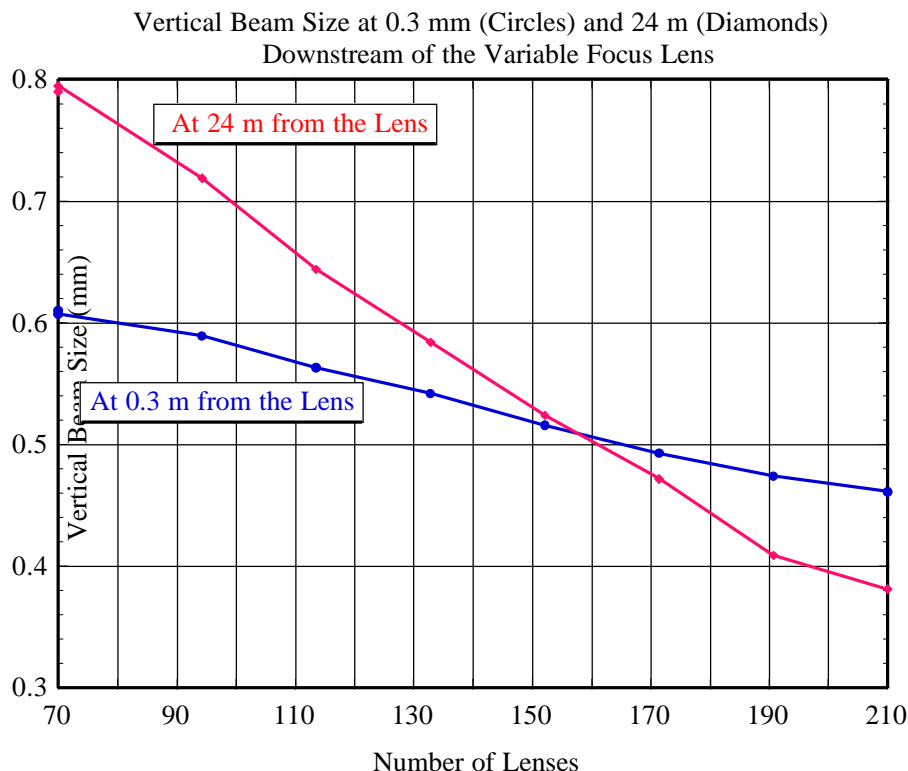
Fig. 2.28. Variation in the vertical size of an x-ray beam with the number of lenses on its path measured at 0.3 m and 24 m downstream of the CXL.

We expect that reducing the lens wall thickness from the present 0.2 mm to 0.1 mm will approximately double the throughput in the present setup. The next generation of the lenses, with a wall thickness of 0.1 mm has recently be obtained, and tests are planned.

2.4 References

L. Assoufid, M. Bray, D. Shu, J. Qian, SPIE Meeting, Seattle, WA, July 7-11, 2002a

L. Assoufid, A.T. Macrander, S, Narayanan, R. Khachatryan, and S. Krasnicki, American Physical Society March Meeting, Session S21-Focus session: Synchrotron Radiation Base Instruments and Measurements. Indianapolis, Indiana, March 21, 2002b

Y.S. Chu, C. Liu, D.C. Mancini, F. De Carlo, A.T. Macrander, B. Lai, and D. Shu, Rev. Sci. Instrum. **73**, 1485 (2002)

B. Deriy, Yu. Eidelman, O. Makarov, and I. Vasserman, "New Magnetic Measurement System at the Advanced Photon Source," Proceedings of the 8th International Conference on Accelerator and Large Experimental Physics Control Systems, held Nov 27-30, 2001, San Jose, CA. Available at:

http://www.slac.stanford.edu/econf/C01 1127/TUAP051.pdf.

R. Divan, D. Mancini, N. Moldovan, L. Assoufid, Y. Chu, Q. Ma, and R.A.

Rosenberg, 2001 International Micro-processes and Nanotechnology Conference, October 29 – 31, 2001, Kunibiki Messe, Matsue-shi, Shimane, Japan

G. E. Ice, J-S. Chung, J.Z. Tischler, A. Lunt, and L. Assoufid , Rev. Sci. Intrum. **71**, 2635 (2000)

C. Liu, A.T. Macrander, J. Als-Nielsen, and K. Zhang, J. Vac. Sci. Technol. A **19**, 1421 (2001))

J. Maj, A.T. Macrander, S. Krasnicki, P.B. Fernandez, and R.A. Erck, Rev. Sci. Instrum. **73**, 1546 (2002)

P.V. Satyam, R.E. Cook, S. Narayanan, L. Assoufid, J. Wang, J. Kamila, D. Goswami, and B.N. Dev, The 11th User Meeting for the Advanced Photon, Argonne National Laboratory, Illinois, October 9-11, 2001

APPENDIX

Staff Publications January 2001 – June 2002

K. Achterhold, C. Keppler, A. Ostermann, U. van Bürck, W. Sturhahn, E. E. Alp, F. G. Parak, "Vibrational dynamics of myoglobin determined by the phonon-assisted Mössbauer effect," Phys. Rev. E **65**, 051916-1-13 (2002).

B. Adams, Y. Nishino, D. V. Novikov, G. Materlik, D. M. Mills, "Parametric Down Conversion of X-rays, Recent Experiments," Nucl. Instrum. Methods A **467-468**, 1019-1020 (2001).

I. Ahmad, J. C. Banar, J. A. Becker, D. S. Gemmell, A. Kraemer, A. Mashayekhi, D. P. McNabb, G. G. Miller, E. F. Moore, L. N. Pangault, R. S. Rundberg, J. P. Schiffer, S. D. Shastri, T. F. Wang, J. B. Wilhelmy, "Search for X-ray Induced Acceleration of the Decay of the 31-Yr Isomer of [178]Hf Using Synchrotron Radiation," Phys. Rev. Lett. **87**, 072503-1-4 (2001).

E. E. Alp, H. Sinn, A. Alatas, W. Sturhahn, T. Toellner, J. Zhao, J. Sutter, M. Hu, D. Shu, Y. Shvydko, "Source and Optics Considerations for New Generation High-Resolution Inelastic X-ray Spectrometers," Nucl. Instrum. Methods A **467-468**, 617-622 (2001).

E. E. Alp, W. Sturhahn, T. S. Toellner, "Lattice Dynamics and Inelastic Nuclear Resonant X-ray Scattering," J. Phys. Condens. Matter **13**, 7645-7658 (2001).

E. E. Alp, W. Sturhahn, T. S. Toellner, "Lattice dynamics and inelastic nuclear resonant x-ray scattering," Hyperfine Interact. **135**, 295-310 (2001).

W. J. Antel, Jr., I. Coulthard, J. W. Freeland, A.P J. Stampfl, M. M. Schwickert, "Method for the Measurement of Anisotropy and Rotational Hysteresis Using Linear Dichroism," Appl. Phys. Lett. **79**, 997-999 (2001).

F. M. Anthony, A. M. Khounsary, D. R. McCarter, F. Krasnicki, M. Tangedahl, "McCarter Superfinish Grinding for Silicon - An Update," Proc. SPIE Vol. **4145**, A.K.Freund, T. Ishikawa, A.M. Khounsary, D.C. Mancini, A.G. Michette, and S. Oestreich, eds. (2001) pp. 37-44.

D. A. Arms, R. O. Simmons, M. Schwoerer-Böhning, A. T. Macrander, T. J. Graber, "Exciton Dispersion and Electronic Excitations in hcp [4]He," Phys. Rev. Lett. **87**, 156402-1-4 (2001).

N. D. Arnold, J. Attig, G. Banks, R. Bechtold, K. Beczek, C. Benson, S. Berg, W. Berg, S. Biedron, J. A. Biggs, M. Borland, K. Boerste, M. Bosek, W. R. Brzowski, J. Budz, J. A. Carwardine, P. Castro, Y. C. Chae, S. Christensen, C. Clark, M. Conde, E. A. Crosbie, G. A. Decker, R. J. Dejus, H. DeLeon, P. K. Den Hartog, B. N. Deriy, D. Dohan, P. Dombrowski, D. Donkers, C. L. Doose, R. J. Dortwegt, G. A. Edwards, Y. Eidelman, M. J.

Erdmann, J. Error, R. Ferry, R. Flood, J. Forrestal, H. Freund, H. Friedsam, J. Gagliano, W. Gai, J. N. Galayda, R. Gerig, R. L. Gilmore, E. Gluskin, G. A. Goeppner, J. Goetzen, C. Gold, A. J. Gorski, A. E. Grelick, M. W. Hahne, S. Hanuska, K. C. Harkay, G. Harris, A. L. Hillman, R. Hogrefe, J. Hoyt, Z. Huang, J. M. Jagger, W. G. Jansma, M. Jaski, S. J. Jones, R. T. Kean, A. L. Kelly, C. Keyser, K. J. Kim, S. H. Kim, M. Kirshenbaum, J. H. Klick, K. Knoerzer, R. J. Koldenhoven, M. J. Knott, S. Labuda, R. Laird, J. Lang, F. Lenkszus, E. S. Lessner, J. W. Lewellen, Y. Li, R. M. Lill, A. H. Lumpkin, O. A. Makarov, G. M. Markovich, M. McDowell, W. P. McDowell, P. E. McNamara, T. Meier, D. Meyer, W. Michalek, S. V. Milton, H. Moe, E. R. Moog, L. Morrison, A. Nassiri, J. R. Noonan, R. Otto, J. Pace, S. J. Pasky, J. M. Penicka, A. F. Pietryla, G. Pile, C. Pitts, J. Power, T. Powers, C. C. Putnam, A. J. Puttkammer, D. Reigle, L. Reigle, D. Ronzhin, E. R. Rotela, E. F. Russell, V. Sajaev, S. Sarkar, J. C. Scapino, K. Schroeder, R. A. Seglem, N. S. Sereno, S. K. Sharma, J. F. Sidarous, O. Singh, T. L. Smith, R. Soliday, G. A. Sprau, S. J. Stein, B. Stejskal, V. Svirtun, L. C. Teng, E. Theres, K. Thompson, B. J. Tieman, J. A. Torres, E. M. Trakhtenberg, G. Travish, G. F. Trento, J. Vacca, I. B. Vasserman, N. A. Vinokurov, D. R. Walters, J. Wang, X. J. Wang, J. Warren, S. Wesling, D. L. Weyer, G. Wiemerslage, K. Wilhelmi, R. Wright, D. Wyncott, S. Xu, B. X. Yang, W. Yoder, R. B. Zabel, "Observation and Analysis of Self-Amplified Spontaneous Emission at the APS Low-Energy Undulator Test Line," Nucl. Instrum. Methods A **475**, 28-37 (2001).

L. Assoufid, "Future Metrology Needs for FEL Reflective Optics," Proc. SPIE Vol. **4143**, D.M. Mills, H. Schulte-Schrepping, and J.R. Arthur, eds. (2001) pp. 98-102.

L. Assoufid, O. Hignette, M. Howells, S. Irick, H. Lammert, P. Takacs, "Future Metrology Needs for Synchrotron Radiation Grazing-Incidence Optics," Nucl. Instrum. Methods A **467**, 267-270 (2001).

L. Assoufid, A. Khounsary, J. Qian, A. Macrander, D. Mills, "Surface Quality of X-ray Mirrors Evaluated at the Advanced Photon Source," X-ray Mirrors, Crystals, and Multilayers, Proc. SPIE Vol. **4501**, A.K. Freund, T. Ishikawa, and A.M. Khounsary, eds. (2001) pp. 54-62.

O. Auciello, J. C. Tucek, A. R. Krauss, D. M. Gruen, N. Moldovan, D. C. Mancini, "Reveiw of Synthesis of Low-Work Function Cu-Li Alloy Coatings and Characterization of the Field Emission Properties for Application to Field Emission Devices," J. Vac. Sci. Technol. B **19**, 877-883 (2001).

Y. S. Badyal, D. L. Price, M.- L. Saboungi, D. R. Haeffner, S. D. Shastri, "Quantum effects on the structure of water at constant temperature and constant atomic density," J. Chem. Phys. **116**, 10833-10837 (2002).

J. Bahrdt, W. Frentrup, A. Gaupp, M. Scheer, W. Gudat, G. Ingold, S. Sasaki, "Elliptically Polarizing Insertion Devices at BESSY II," Nucl. Instrum. Methods A **467-468**, 21-29 (2001).

J. Bahrdt, W. Frentrup, A. Gaupp, M. Scheer, W. Gudat, G. Ingold, S. Sasaki, "A Quasi-Periodic Hybrid Undulator at BESSY II," Nucl. Instrum. Methods A **467-468**, 130-133 (2001).

S. G. Biedron, R. J. Dejus, Z. Huang, S. V. Milton, V. Sajaev, W. Berg, M. Borland, P. K. Den Hartog, M. Erdmann, W. M. Fawley, H. P. Freund, E. Gluskin, K. J. Kim, J. W. Lewellen, Y. Li, A. H. Lumpkin, E. R. Moog, A. Nassiri, G. Wiemerslage, B. X. Yang, "Measurements of Nonlinear Harmonic Generation at the Advanced Photon Source's SASE FEL," Nucl. Instrum. Methods A **483**, 94-100 (2002).

S. G. Biedron, M. Borland, P. Den Hartog, R. Dejus, M. Erdmann, Z. Huang, K.-J Kim, J. Lewellen, Y. Li, A. Lumpkin, O. Makarov, S. V. Milton, E. Moog, V. Sajaev, G. Wiemerslage, "The low-energy undulator test line: a SASE FEL operating from 660 to 130 nm," X-ray Lasers 2002: 8th International Conference on X-ray Lasers, J.J. Rocca et al., eds., AIP Conf. Proc. **641** (2002) pp. 357-364.

A. Bienenstock, D. Mills, G. Shenoy, H. Winick, "Synchrotron Radiation," in *Encyclopedia of Science & Technology* (McGraw-Hill, 2001).

S. J. L. Billinge, V. Petkov, Th. Proffen, G. H. Kwei, J. L. Sarrao, S. D. Shastri, S. Kycia, "Charge Inhomogeneities in the Colossal Magnetoresistant Manganites from the Local Atomic Structure," Mater. Res. Soc. Symp. Proc. **602** (2001) p. 177.

C. A. Burns, P. M. Platzman, H. Sinn, A. Alatas, E. E. Alp, "Evidence for an Instability near Twice the Fermi Wave Vector in the Low Electronic Density Liquid Metal Li(NH$_3$)$_4$," Phys. Rev. Lett. **86**, 2357-2360 (2001).

Z. Cai, B. Lai, P. Ilinski, D. Legnini, W. Yun, "X-ray microdiffraction study of martensite-retained austenite microstructures at the tip of a steel blade," Proc. SPIE Vol. **4499**, I. McNulty, ed. (2001) pp. 19-22.

Z. Cai, "A hard x-ray hundred-nanometer probe and its application," in *Nanoscience and Nanotechnology in Perspective*, (Tsinghua University Press, 2002) pp. 106-114.

R. Callens, R. Coussement, C. L'abbe, S. Nasu, K. Vyvey, T. Yamada, Y. Yoda, J. Odeurs, "Stroboscopic detection of nuclear forward-scattered synchrotron radiation," Phys. Rev. B **65**, 180404-1-4 (2002).

D. Casa, B. Keimer, M. v. Zimmerman, J. P. Hill, H. U. Habermeier, F. S. Razavi, "Unusual x-ray transport phenomena in La$_{(1-x)}$Sr$_x$MnO$_3$," Phys. Rev. B **64**, 100404-100407 (2001).

M. Cholewa, C. Dillon, P. Lay, D. Phillips, T. Talarico, B. Lai, "High resolution muclear and x-ray microprobes and their application in single cell analysis," Nucl. Instrum. Methods B **181**, 715-722 (2001).

Y. S. Chu, T. E. Lister, W. G. Cullen, H. You, Z. Nagy, "Commensurate Water Monolayer at the RuO(sub)2(110)/Water Interface," Phys. Rev. Lett. **86**, 3364-3367 (2001).

Y. S. Chu, C. Liu, D. C. Mancini, F. De Carlo, A. T. Macrander, B. Lai, D. Shu, "Performance of a double-multilayer monochromator at beamline 2-BM at the Advanced Photon Sourcex," Rev. Sci. Instrum. **73**, 1485-1487 (2002).

I. Coulthard, T. K. Sham, Y.- F. Hu, S. J. Naftel, P.- S. Kim, J. W. Freeland, "Threshold Behavior of Cu $L_3M_{4,5}M_{4,5}$ Auger Effect of Cu Metal at the L_3-Edge," Phys. Rev. B **64**, 5101 (2001).

J. J. Curry, H. Adler, S. D. Shastri, J. E. Lawler, "Minority Additive Distributions in a Ceramic Metal-Halide Arc Lamp Using High-Energy X-ray Induced Fluorescence," Appl. Phys. Lett. **79**, 1974-1976 (2001).

M. F. DeCamp, D. A. Reis, P. H. Bucksbaum, B. Adams, J. M. Caraher, R. Clarke, C.W S. Conover, E. M. Dufresne, R. Merlin, V. Stoica, J. Wahlstrand, "Coherent Control of Pulsed X-ray Beams," Nature **413**, 825-828 (2001).

F. De Carlo, P. Albee, Y. S. Chu, D. C. Mancini, B. Tieman, S. Y. Wang, "High-throughput real-time x-ray microtomography at the Advanced Photon Source," Proc. SPIE Vol. **4503**, U. Bonse, ed. (2002) pp. 1-13.

P. Den Hartog, J. Gagliano, G. Goeppner, J. Noonan, E. Trakhtenberg, G. Wiemerslage, "Vacuum System of the APS: Operation Experience and Status Report," Proc. 2001 Particle Accelerator Conf. (IEEE, 2001) pp. 607-609.

P. Den Hartog, E. Moog, C. Benson, M. Erdmann, A. Lumpkin, O. Makarov, M. Petra, B. Tieman, E. Trakhtenberg, G. Wiemerslage, "UV-VUV diagnostics for the Advanced Photon Source SASE FEL," Nucl. Instrum. Methods A **483**, 407-411 (2002).

C. T. Dillon, P. T. Lay, B. J. Kennedy, A.P J. Stampfl, Z. Cai, P. Ilinski, W. Rodrigues, D. G. Legnini, B. Lai, J. Maser, "Hard x-ray microprobe studies of chromium(VI)-treated V79 Chinese hamster lung cells: intracellular mapping of the biotransformation products of a chromium carcinogen," J. Biol. Inorg. Chem. **7**, 640-645 (2002).

E. DiMasi, J. O. Fossum, T. Gog, C. T. Venkataraman, "Orientational Order in Gravity Dispersed Clay Colloids: A Synchrotron X-ray Scattering Study of Na Fluorohectorite Suspensions," Phys. Rev. E **64**, 061704-061710 (2001).

A. Doyuran, M. Babzien, T. Shaftan, L. H. Yu, I. Ben-Zvi, S. G. Biedron, L. F. DiMauro, W. Graves, E. Johnson, S. Krinsky, R. Malone, I. Pogorelsky, J. Skaritka, G. Rakowsky, X. J. Wang, M. Woodle, V. Yakimenko, J. Jagger, V. Sajaev, I. Vasserman, "Characterization of a High-Gain Harmonic-Generation Free-Electron Laser at Saturation," Phys. Rev. Lett. **86**, 5902-5905 (2001).

A. Doyuran, M. Babzien, T. Shaftan, S. G. Biedron, L. H. Yu, I. Ben-Zvi, L. F. DiMauro, W. Graves, E. Johnson, S. Krinsky, R. Malone, I. Pogorelsky, J. Skaritka, G. Rakowsky, X. J. Wang, M. Woodle, V. Yakimenko, J. Jagger, V. Sajaev, I. Vasserman, "New Results of the

High-Gain Harmonic Generation Free-Electron Laser Experiment," Nucl. Instrum. Methods A **475**, 260-265 (2001).

D. E. Eastman, C. B. Stagarescu, G. Xu, P. M. Mooney, J. L. Jordan-Sweet, B. Lai, Z. Cai, "Observation of columnar microstructure iin step-graded $Si_{1-x}Ge[sub_x/Si$ films using high-resolution x-ray microdiffraction," Phys. Rev. Lett. **88**, 156101-1-4 (2002).

T. Egami, E. Mamontov, W. Dmowski, T. Gog, C. Venkataraman, P. W. Rehrig, L. E. Cross, "Electronic States of Ferroelectric Oxides Probed by X-ray Spectroscopy and Scattering," AIP Conf. Proc. **626** (2002) p. 216.

L. Emery, M. Borland, R. J. Dejus, E. Gluskin, E. Moog, "Progress and Prospects towards Brightness Improvements at the Advanced Photon Source," Proceedings of the 2001 Particle Accelerator Conference, Vol. 4, P. Lucas, S. Webber, eds. (IEEE 2001) pp. 2602-2604.

K. T. Erwin, O. Delaire, A. T. Motta, Y. S. Chu, D. C. Mancini, R. C. Birtcher, "Observation of Second-Phase Particles in Bulk Zirconium Alloys Using Synchrotron Radiation," J. Nucl. Mater. **294**, 299-304 (2001).

P. G. Evans, E. D. Isaacs, G. Aeppli, Z. Cai, B. Lai, "X-ray microdiffraction images of antiferromagnetic domain evolution in chromium," Science **295**, 1042-1045 (2002).

P. Fenter, M. T. McBride, G. Srajer, N. C. Sturchio, D. Bosbach, "Structure of Barite(001)- and (210)-Water Interfaces," J. Phys. Chem. B **105**, 8112-8119 (2001).

P. B. Fernandez, W.- K. Lee, D. M. Mills, G. Tajiri, L. Assoufid, "Double-Undulator Tests of a Diamond Monochromator at the Advanced Photon Source," Nucl. Instrum. Methods A **459**, 347-353 (2001).

K. Fezzaa, W.- K. Lee, "A X-ray Interferometer with a Large and Variable Path Length Difference," J. Appl. Crystallogr. **34**, 166-171 (2001).

J. W. Freeland, I. Coulthard, W. J. Antel, Jr., A.P J. Stampfl, "Interface Bonding for Fe Thin Films on GaAs Surfaces of Differing Morphology," Phys. Rev. B **63**, 193301-1-4 (2001).

J. W. Freeland, J. C. Lang, G. Srajer, R. Winarski, D. Shu, D. M. Mills, "A unique polarized x-ray facility at the Advanced Photon Source," Rev. Sci. Instrum. **73**, 1408-1410 (2002).

R. F. Garrett, N. Blagojevic, Z. Cai, B. Lai, D. G. Legnini, W. Rodrigues, A.P.J Stampfl, "Synchrotron X-Ray Microprobe Analysis of Radioactive Trace Elements in Mineral Sands," Nucl. Instrum. Methods A **467-468**, 897-900 (2001).

E. Gluskin, P. Ilinski, N. Vinokurov, "Predicted Performance of the LCLS X-ray Diagnostics," AIP Conf. Proc.: Physics of, and Science with, the X-ray Free-Electron Laser, S.

Chattopadhyay, M. Cornacchia, I. Lindou, and C. Pellegrini, eds., AIP Conf. Proc. **581**, (2001) pp. 131-140.

E. Gluskin, N. A. Vinokurov, G. Decker, R. J. Dejus, P. Emma, P. Ilinski, E. R. Moog, H.- D. Nuhn, I. B. Vasserman, "Optimization of the Design for the LCLS Undulator Line," Nucl. Instrum. Methods A **475**, 323-327 (2001).

D. Haskel, E. A. Stern, F. Dogan, A. R. Moodenbaugh, "Dopant Structural Distortions in High-Temperature Superconductors: An Active or a Passive Role?" J. Synchrotron Rad. **8**, 186-190 (2001).

D. Haskel, G. Srajer, J. C. Lang, J. Pollmann, C. S. Nelson, J. S. Jiang, S. D. Bader, "Enhanced Interfacial Magnetic Coupling of Gd/Fe Multilayers," Phys. Rev. Lett. **87**, 207201-1-4 (2001).

M. Z. Hassan, P. A. Montano, E. D. Isaacs, Z.-X. Shen, H. Eisaki, S. K. Sinha, Z. Islam, S. Uchida, "Momentum-Resolved Charge Excitations in a Protoype One-Dimensional Mott Insulator," Phys. Rev. Lett. **88**, 177403-1-4 (2002).

J. P. Hill , C. S. Nelson, M. v. Zimmerman, Y. -J Kim, D. Gibbs, D. Casa, B. Keimer, Y. Murakami, C. Venkataraman, T. Gog, Y. Tomioka, Y. Tokura, T. Y. Koo, S. W. Cheong, "Orbital Correlations in Doped Manganites," Appl. Phys. A **73**, 723-730 (2001).

S. Hosokawa, Y. Kawakita, W. C. Pilgrim, H. Sinn, "Inelastic x-ray scattering study on the dynamics of liquid Ge," Phys. Rev. B **63**, 134205-1-5 (2001).

S. Hosokawa, H. Sinn, F. Hensel, A. Alatas, E. E. Alp, W.-C Pilgrim, "Collective dynamics of liquid Hg investigated by inelastic x-ray scattering," J. Non-Cryst. Solids **312-314**, 163-167 (2002).

S. Hosokawa, Y. Kawakita, W.-C. Pilgrim, H. Sinn, "Studies of collective dynamics in liquid Ge over a wide temperature range using inelastice x-ray scattering technique," Physica B **316-317**, 610-612 (2002).

Z. W. Hu, B. Lai, Y. S. Chu, Z. Cai, D. C. Mancini, B. R. Thomas, A. A. Chernov, "Phase Sensitive X-ray Diffraction Imaging of Defects in Biological Macromolecular Crystals," Phys. Rev. Lett. **87**, 148101-1-4 (2001).

Y. Hwu, W. L. Tsai, B. Lai, J. H. Je, G. H. Fecher, M. Bertolo, G. Margaritondo, "Using Photoelectron Emission Microscopy with Hard X-rays," Surf. Sci. **480**, 188-195 (2001).

P. P. Ilinski, B. Lai, N. J. Bassom, J. Donald, G. Athas, "X-ray Zone Plate Fabrication Using a Focused Ion Beam," Proc. SPIE Vol. **4145** (2001) p. 311.

Z. Islam, J. C. Lang, L. Vasiliu-Doloc, G. Srajer, P. C. Canfield, "Resonant X-ray Scattering Study of Magnetic Ordering Due to Fermi-surface Nestingin $SmNi_2Ge_2$," Phys. Rev. B **65**, 054404-1-8 (2001).

Z. Islam, S. K. Sinha, D. Haskel, J. C. Lang, G. Srajer, B. W. Veal, D. R. Haeffner, H. A. Mook, "X-ray diffraction study of lattice modulations in an underdoped $YBa_2Cu_3O_{6+x}$ superconductor," Phys. Rev. B **66**, 092501-1-4 (2002).

A. Khounsary, J. Maser, "A Water-Cooled X-ray Monochromator for Using Off-Axis Undulator Beam," Nucl. Instrum. Methods A **467-468**, 654-658 (2001).

A. Khounsary, P. Fernandez, L. Assoufid, D. Mills, D. Walters, J. Schwartz, J. Robichaud, "Design, fabrication, and evaluation of an internally cooled silicon carbide mirror," Rev. Sci. Instrum. **73**, 1537-1540 (2002).

H. Kim, O. H. Seeck, D. R. Lee, I. D. Kaendler, D. Shu, J. K. Basu, S. K. Sinha, "Synchrotron X-ray Studies of Molecular Ordering in Confined Liquids," Mat. Res. Soc. Symp. Proc. Vol. **651** (2001) pp. T2.1.1-T2.1.7.

H. Kim, A. K. Ramdas, S. Rodriguez, Z. Barticevic, M. Grimsditch, T. R. Anthony, "Magnetospectroscopy of Acceptors in "Blue" Diamonds," Physica B **302-303**, 88-100 (2001).

H. Kim, A. Ruhm, L. B. Lurio, J. K. Basu, J. Lal, S. K. Sinha, D. Lumma, S. G. J. Mochrie, "Surface Dynamics of Polymer Films," Phys. Rev. Lett. **in press, pp. x-x, (2001).**

M. J. Kramer, L. Margulies, A. I. Goldman, P. L. Lee, "Measuring crystal structure dynamics during polymorphic phase transitions," J. Alloy Comp. **338**, 235-241 (2002).

T. M. Kuzay, M. Kazmierczak, B. J. Hsieh, "X-ray Beam/Biomaterial Thermal Interactions in Third-Generation Synchrotron Sources," Acta Crystallogr. D **57**, 69-81 (2001).

C. L'abbe, R. Callens, J. Odeurs, "Time-Integrated Synchrotron Mössbauer Spectroscopy," Hyperfine Interact. **135**, 275-294 (2001).

B. Lai, J. Maser, T. Paunesku, G. E. Woloschak, "Workshop on biological applications of x-ray microbeams," Synchrotron Radiat. News **15**, 18-20 (2002).

J. C. Lang, J. Pollmann, D. Haskel, G. Srajer, J. Maser, J. S. Jiang, S. D. Bader, "Imaging Buried Magnetic Domains Using Hard X-rays," X-ray Micro- and Nano-Focusing: Applications and Techniques II, Proc. SPIE Vol. **4499**, I. McNulty, ed. (2001) pp. 1-9.

W.- K. Lee, K. Fezzaa, P. Fernandez, G. Tajiri, D. Mills, "Performance Limits of Indirectly Cryogenically Cooled Silicon Monochromators - Experimental Results at the APS," J. Synchrotron Rad. **8**, 22-25 (2001).

APPENDIX

W.- K. Lee, K. Fezzaa, J. Wang, "X-ray Propagation-Based Phase-Enhanced Imaging of Fuel Injectors," Proc. ASME 2001: Diesel Combustion and Emissions, Fuel Injection and Sprays, V.W. Wong, ed., ICE-Vol. **37-1** (ASME, 2001) pp. 11-14.

Z. H. Levine, S. Grantham, S. Neogi, S. P. Frigo, I. McNulty, C. C. Retsch, Y. Wang, T. B. Lucatorto, "Accurate Pattern Registration for Integrated Circuit Tomography," J. Appl. Phys. **90**, 556-560 (2001).

Z. H. Levine, S. Grantham, I. McNulty, "Mass absorption coefficient of tungsten for 1600-2100 eV," Phys. Rev. B **65**, 064111-1-5 (2002).

J. W. Lewellen, S. V. Milton, E. Gluskin, N. D. Arnold, C. Benson, W. Berg, S. G. Biedron, M. Borland, Y. C. Chae, R. J. Dejus, P. K. Den Hartog, B. Deriy, M. Erdmann, Y. I. Eidelman, M. W. Hahne, Z. Huang, K. J. Kim, Y. Li, A. H. Lumpkin, O. Makarov, E. R. Moog, A. Nassiri, V. Sajaev, R. Soliday, B. J. Tieman, E. M. Trakhtenberg, I. B. Vasserman, N. A. Vinokurov, G. Wiemerslage, B. X. Yang, "Present Status and Recent Results from the APS SASE FEL," Nucl. Instrum. Methods A **483**, 40-45 (2002).

J. W. Lewellen, S. G. Biedron, M. Borland, Y. C. Chae, R. J. Dejus, E. Gluskin, P. K. Den Hartog, Z. Huang, K. J. Kim, A. H. Lumpkin, S. V. Milton, E. R. Moog, V. Sajaev, "A Sampling of Recent Measurements at the APS SASE-FEL," Nucl. Instrum. Methods A **483**, II-1-II-2 (2002).

J. Libera, Z. Cai, B. Lai, S. Xu, "Integration of a hard x-ray microprobe with a diffractometer for microdiffraction," Rev. Sci. Instrum. **73**, 1506-1508 (2002).

C. Liu, A. Macrander, J. Als-Nielsen, K. Zhang, "Laterally Graded Multilayers and Their Applications," J. Vac. Sci. Technol. A **19**, 1421-1424 (2001).

C. Liu, A. Macrander, "Simple Vacuum Heater and its Application for Annealing TiO[sub 2] Films," J. Vac. Sci. Technol. A **19**, 2703-2705 (2001).

M. J. Longfield, J. Wilmshurst, L. Bouchenoire, M. J. Cooper, D. Mannix, G. H. Lander, N. Bernhoeft, A. Stunault, W. G. Stirling, J. Pollmann, D. Haskel, G. Srajer, "The Use of Resonant X-ray Magnetic Scattering to Examine the Magnetic Phases in UAs-USe Solid Solutions," J. Magn. Magn. Mater. **233**, 53-56 (2001).

A. H. Lumpkin, R. Dejus, W. J. Berg, M. Borland, Y. C. Chae, E. Moog, N. S. Sereno, B. X. Yang, "First Observation of z-Dependent Electron-Beam Microbunching Using Coherent Transition Radiation," Phys. Rev. Lett. **86**, 79-82 (2001).

A. H. Lumpkin, W. Berg, S. G. Biedron, M. Borland, Y. C. Chae, R. J. Dejus, J. W. Lewellen, S. V. Milton, E. Moog, G. Travish, B. X. Yang, "Investigations of Electron-Beam Microbunching and Beam Coalignment Using CTR in a High-Gain SASE FEL," Proceedings of the 2001 Particle Accelerator Conference, P. Lucas, S. Webber, eds., Vol. 1 (IEEE, 2001) pp. 550-552.

A. H. Lumpkin, B. X. Yang, W. J. Berg, Y. C. Chae, N. S. Sereno, R. J. Dejus, C. Benson, E. Moog, "Utilization of CTR to Measure the Evolution of Electron-Beam Microbunching in a Self-Amplified Spontaneous Emission (SASE) Free-Electron Laser (FEL)," Nucl. Instrum. Methods A **475**, 462-469 (2001).

A. B. Lumpkin, W. Berg, S. G. Biedron, M. Borland, R. Dejus, M. Erdmann, Z. Huang, J. W. Lewellen, Y. Li, S. V. Milton, E. Moog, V. Sajaev, B. X. Yang, "First Observations of Electron-Beam Microbunching in the Ultraviolet at 265 nm Using COTR in a SASE FEL," Nucl. Instrum. Methods A **483**, 402-406 (2002).

A. H. Lumpkin, R. Dejus, J. W. Lewellen, W. Berg, S. G. Biedron, M. Borland, Y. Chae, M. Erdmann, Z. Huang, K. J. Kim, Y. Li, S. V. Milton, E. Moog, D. W. Rule, V. Sajaev, B. X. Yang, "Comprehensive z-Dependent Measurements of Electron-Beam Microbunching Using COTR in a Saturated SASE FEL," Nucl. Instrum. Methods A **483**, 394-401 (2002).

A. H. Lumpkin, R. J. Dejus, J. W. Lewellen, S. Berg, S. G. Biedron, M. Borland, Y. C. Chae, M. Erdmann, Z. Huang, K-J Kim, Y. Li, S. V. Milton, D. W. Rule, V. Sajaev, B. X. Yang, "Evidence for Microbunching 'Sidebands' in a Saturated FEL Using Coherent Optical Transition Radation," Phys. Rev. Lett. **88**, 234801 (2002).

Q. Ma, N. Moldovan, D. C. Mancini, R. A. Rosenberg, "Wet Etching of GaAs Using Synchrotron Radiation X Rays," J. Appl. Phys. **89**, 3033-3040 (2001).

A. MacPhee, M. W. Tate, C. F. Powell, Y. Yue, M. J. Renzi, A. Ercan, S. Narayanan, E. Fontes, J. Walther, J. Schaller, S. M. Gruner, J. Wang, "X-ray imaging of shock waves generated by high-pressure fuel sprays," Science **295**, 1261-1263 (2002).

J. A. Maj, A. T. Macrander, S. F. Krasnicki, P. B. Fernandez, R. A. Erck, "Etching of diamonds for x-ray monochromators," Rev. Sci. Instrum. **73**, 1546-1549 (2002).

O. V. Makarova, C.-M Tang, D. C. Mancini, N. Moldovan, R. Divan, D. G. Ryding, R. H. Lee, "Microfabrication of freestanding metal structures released from graphite substrates," The 15th IEEE International Conference on Micro Electro Mechanical Systems IEEE, (2002) pp. 400-402.

D. C. Mancini, N. A. Moldovan, R. Divan, F. De Carlo, J. Yaeger, "Process Strategies for Ultra-Deep X-ray Lithography at the Advanced Photon Source," Micromachining and Microfabrication Process Technology, Proc. SPIE Vol. **4557**, J.M. Karam and J. Yasaitis, eds. (2001) pp. 77-84.

H. K. Mao, J. Xu, V. V. Struzhkin, J. Shu, R. J. Hemley, W. Sturhahn, M. Y. Hu, E. E. Alp, L. Vocadlo, D. Alfe, G. D. Price, M.J. Gillan, M. Schwoerer-Bohning, D. Hausermann, P. Eng, G. Shen, H. Giefers, R. Lubbers, G. Wortmann, "Phonon Density of States of Iron up to 153 Gigapascals," Science **292**, 914-916 (2001).

L. S. Matkin, S. J. Watson, H. F. Gleeson, R. Pindak, J. Pitney, P. M. Johnson, C. C. Huang, P. Barois, A.- M. Levelut, G. Srajer, J. Pollmann, J. W. Goodby, M. Hird, "Resonant X-ray Scattering Study of the Antiferroelectric and Ferrielectric Phases in Liquid Crystal Devices," Phys. Rev. E **64**, 021705-1-6 (2001).

I. McNulty, "Current and ultimate limitations of scanning x-ray nanotomography," Proc. SPIE Vol. **4499**, X-Ray Micro- and Nano-Focusing: Applications and Techniques II, I. McNulty, ed. (2001) pp. 23-28.

A. McPherson, "The X-ray FEL: An Experimenter's Dilemma," Proc. SPIE Vol. **4143**, D.M. Mills, H. Schulte-Schrepping, and J.R. Arthur, eds. (2001) pp. 20-25.

J. Meersschaut, C. L'abbe, M. Rots, S. D. Bader, "Origin of Biquadratic Coupling in Fe/Cr(100) Superlattices," Phys. Rev. Lett. **87**, 107201-1-4 (2001).

S. V. Milton, E. Gluskin, N. D. Arnold, C. Benson, W. Berg, S. G. Biedron, M. Borland, Y. C. Chae, R. J. Dejus, P. K. Den Hartog, B. Deriy, M. Erdmann, Y. I. Eidelman, M. W. Hahne, Z. Huang, K. J. Kim, J. W. Lewellen, Y. Li, A. Lumpkin, O. Makarov, E. R. Moog, A. Nassiri, V. Sajaev, R. Soliday, B. J. Tieman, E. M. Trakhtenberg, G. Travish, I. B. Vasserman, N. A. Vinokurov, X. J. Wang, G. Wiemerslage, B. X. Yang, "Exponential Gain and Saturation of a Self-Amplified Spontaneous Emission Free-Electron Laser," Science **292**, 2037-2041 (2001).

V. Mocella, Y. Epelboin, J. P. Guigay, J. Härtwig, "Applications of Dynamical Diffraction under Locally Plane Wave Conditions: Defects in Nearly Perfect Crystals and X-ray Refractometry," Acta Crystallogr. A **57**, 526-530 (2001).

E. R. Moog, R. J. Dejus, P. K. Den Hartog, E. Gluskin, E. Trakhtenberg, I. Vasserman, V. Tcheskidov, N. Vinokurov, "Design and Manufacture of a Prototype Undulator for the LCLS Project," Proc. 2001 Particle Accelerator Conf., P. Lucas, S. Weber, eds. (IEEE, (2001) p. 256.

S. J. Naftel, P. Zhang, P.- S. Kim, T. K. Sham, I. Coulthard, W. J. Antel, Jr., J. W. Freeland, S. P. Frigo, M.- K. Fung, S. T. Lee, Y. F. Hu, B. W. Yates, "Soft X-ray-Excited Luminescence and Optical X-ray Absorption Fine Structures of Tris (8-Hydroxyquinoline) Aluminum," Appl. Phys. Lett. **78**, 1847-1849 (2001).

C. S. Nelson, M. v. Zimmerman, Y. J. Kim, J. P. Hill, D. Gibbs, V. Kiryukhin, T. Y. Koo, S. -W Cheong, D. Casa, B. Keimer, Y. Tomioka, Y. Tokura, T. Gog, C. T. Venkataraman, "Correlated Polarons in Dissimilar Perovskite Manganites," Phys. Rev. B **64**, 174405-1-6 (2001).

B. M. Ocko, E. B. Sirota, M. Deutsch, E. DiMasi, S. Coburn, J. Strzalka, S. Zheng, A. Tronin, T. Gog, C. Venkataraman, "Positional order and thermal expansion of surface crystalline N-alkane monolayers," Phys. Rev. E **63**, 032602-032604 (2001).

D. Paterson, B. E. Allman, P. J. McMahon, J. Lin, N. Moldovan, K. A. Nugent, I. McNulty, C. T. Chantler, C. C. Retsch, T.H. K. Irving, D. C. Mancini, "Spatial Coherence Measurement of X-ray Undulator Radiation," Opt. Commun. **195**, 79-84 (2001).

A. G. Peele, T.H K. Irving, K. A. Nugent, D. C. Mancini, T. R. Christenson, R. Petre, S. P. Brumby, W. C. Priedhorsky, "LIGA for Lobster: First Observation of Lobster-Eye Focusing from Lithographically Produced Optics," Rev. Sci. Instrum. **72**, 1843-1849 (2001).

A. G. Peele, T.H K. Irving, K. A. Nugent, D. C. Mancini, N. Moldovan, T. R. Christenson, R. Petre, S. P. Brumby, W. C. Priedhorsky, "LIGA for Lobster?" Proc. SPIE Vol. **4145** (2001) pp. 219-226.

V. Petkov, S.J L. Billinge, S. D. Shastri, B. Himmel, "High-Resolution Atomic Distribution Functions of Disordered Materials by High-Energy X-ray Diffraction," J. Non-Cryst. Solids **293-295**, 726-730 (2001).

J. Pollmann, G. Srajer, D. Haskel, J. C. Lang, J. Maser, J. S. Jiang, S. D. Bader, "Magnetic Imaging of a Buried SmCo Layer in a Spring Magnet," J. Appl. Phys. **89**, 7165-7167 (2001).

T. L. Reitz, P. L. Lee, K. F. Czaplewski, J. C. Lang, K. E. Popp, H. H. Kung, "Time-Resolved XANES Investigation of CuO/ZnO in the Oxidative Methanol Reforming Reaction," J. Catal. **199**, 193-201 (2001).

G. Reichardt, J. Bahrdt, J.- S. Schmidt, W. Gudat, A. Ehresmann, R. Muller-Albrecht, H. Molter, H. Schmoranzer, M. Martins, N. Schwentner, S. Sasaki, "A 10-m normal incidence monochromator at the quasi-eriodic undulator U125-2 at BESSY II," Nucl. Instrum. Methods A **467-468**, 462-465 (2001).

C. C. Retsch, I. McNulty, "X-ray Speckle Contrast Variation across Absorption Edges," Phys. Rev. Lett. **87**, 077401-1-4 (2001).

C. C. Retsch, I. McNulty, G. S. Iannacchione, "Elastic coupling of silica gel dynamics in a liquid-crystal-aerosol dispersion," Phys. Rev. E **65**, 032701-1-4 (2002).

A. Richter, R. Guico, J. Wang, "Calibrating an Ellipsometer Using X-ray Reflectivity," Rev. Sci. Instrum. **72**, 3004-3007 (2001).

D. E. Roa, R. K. Smither, "Copper Crystal Lens for Medical Imaging: First Results," Proc. SPIE Vol. **4320**, Physics of Medical Imaging, L.E. Antonuk and M.J. Yaffe, eds. . (2001) pp. 435-446.

R. Röhlsberger, K. W. Quast, T. S. Toellner, P. L. Lee, W. Sturhahn, E. E. Alp, E. Burkel, "Imaging the Temporal Evolution of Nuclear Resonant X-ray Scattering," Appl. Phys. Lett. **78**, 2970-2972 (2001).

R. Röhlsberger, T. S. Toellner, K. W. Quast, W. Sturhahn, E. E. Alp, E. Burkel, "The Nuclear Lighthouse Effect: A New Tool for High-Resolution X-ray Spectroscopy," Nucl. Instrum. Methods A **467**, 1473-1476 (2001).

R. Röhlsberger, K. W. Quast, T. S. Toellner, P. L. Lee, W. Sturhahn, E. E. Alp, E. Burkel, "Observation of the 22.5-keV Resonance in ^{149}Sm by the Nuclear Lighthouse Effect," Phys. Rev. Lett. **87**, 047601-1-4 (2001).

B. Roldan Cuenya, W. Keune, W. Sturhahn, T. S. Toellner, M. Y. Hu, "Structure and vibrational dynamics of interfacial Sn layers in Sn / Si multilayers," Phys. Rev. B **64**, 235321-1-12 (2001).

J. T. Sage, S. M. Durbin, W. Sturhahn, D. C. Wharton, P. M. Champion, P. Hession, J. Sutter, E. E. Alp, "Long-Range Reactive Dynamics in Myoglobin," Phys. Rev. Lett. **86**, 4966-4969 (2001).

J. T. Sage, C. Paxson, G.R A. Wyllie, W. Sturhahn, S. M. Durbin, P. M. Champion, E. E. Alp, W. R. Scheidt, "Nuclear Resonance Vibrational Spectroscopy of a Protein Active Site Mimic," J. Phys. Condens. Matter **13**, 7707-7722 (2001).

O. H. Seeck, S. K. Sinha, I. D. Kaendler, D. Shu, K. Shin, M. Rafailovich, J. Sokolov, M. Tolan, "Interfacial Properties of Soft Matter Thin Films Studied by X-ray Reflectivity," in *Interfacial Properties on the Submicron Scale*, J.E. Frommer and R. M. Overney, eds., (ACS/Oxford Press, 2001) pp. 129-142.

L. Seve, W. Zhu, B. Sinkovic, J. W. Freeland, I. Coulthard, W. J. Antel, Jr., S.S P. Parkin, "Observation of Change in the Oxidation State at Ferromagnet/Insulator Interface upon Thermal Annealing," Europhys. Lett. **55**, 439-444 (2001).

T. Shaftan, M. Babzien, I. Ben-Zvi, S. G. Biedron, L. F. DiMauro, A. Doyuran, W. Graves, J. Jagger, E. Johnson, S. Krinsky, R. Malone, I. Pogorelsky, V. Sajaev, B. Sheehy, J. Skaritka, L. Solomon, G. Rakowsky, I. Vasserman, J. H. Wu, X. J. Wang, M. Woodle, V. Yakimenko, L. H. Yu, "High-Gain Harmonic Generation Free-Electron Laser at Saturation," Proceedings of the 2001 Particle Accelerator Conference, P. Lucas, S. Webber, eds., Vol. **1** (IEEE, 2001) pp. 246-248.

S. D. Shastri, P. Zambianchi, D. M. Mills, "Dynamical Diffraction of Ultrashort X-ray Free-Electron Laser Pulses," J. Synchrotron Rad. **8**, 1131-1135 (2001).

S. D. Shastri, J. M. Maser, B. Lai, J. Tys, "Microfocusing of 50 keV Undulator Radiation with Two Stacked Zone Plates," Opt. Commun. **197**, 9-14 (2001).

S. D. Shastri, P. Zambianchi, D. M. Mills, "Femtosecond X-ray Dynamical Diffraction by Perfect Crystals," Proc. SPIE Vol. **4143**, *X-ray FEL Optics and Instrumentation*, D.M. Mills, H. Schulte-Schrepping, and J.R. Arthur, eds. (2001) pp. 69-77.

S. D. Shastri, K. Fezzaa, A. Mashayekhi, W. -K. Lee, P. B. Fernandez, P. L. Lee, "Cryogenically cooled bent double-Laue monochromator for high-energy undulator x-rays (50-200 keV)," J. Synchrotron Rad. **9**, 317-322 (2002).

D. Shu, M. Ramanathan, T. M. Kuzay, "General Design of the Layout for New Undulator-Only Beamline Front Ends," Nucl. Instrum. Methods A **467-468**, 762-766 (2001).

D. Shu, J. Chang, T. M. Kuzay, D. G. Brasher, "Development and Applications of Rectangular Box-Type Explosively Bonded Structures for High-Heat-Load Beamline Components," Nucl. Instrum. Methods A **467-468**, 771-774 (2001).

D. Shu, T. S. Toellner, E. E. Alp, "Modular Overconstrained Weak-Link Mechanism for Ultraprecision Motion Control," Nucl. Instrum. Methods A **467-468**, 771-774 (2001).

D. Shu, P. K. Job, T. M. Kuzay, S. Korenev, "CVD-Diamond-Based Position-Sensitive Detector Test with Electron Beam from a Rhodotron[TM] Accelerator," Proc. 2001 Particle Accelerator Conf. (IEEE, 2001) pp. 2435-2437.

D. Shu, M. Ramanathan, "Design studies of the APS canted undulator beamline front ends," Rev. Sci. Instrum. **73**, 1580-1582 (2002).

D. Shu, M. Ramanathan, D. R. Haeffner, "Recent design upgrades of the APS beamline standard components," Rev. Sci. Instrum. **73**, 1584-1586 (2002).

D. Shu, Y. Han, T. S. Toellner, E. E. Alp, "A linear actuator system with 1 angstrom closed-loop control resolution and 50 mm travel range," Proc. SPIE Vol. **4771** (2002) pp. 78-90.

Yu V. Shvyd'ko, M. Lucht, E. Gerdau, M. Lerche, E. E. Alp, W. Sturhahn, J. Sutter, T. S. Toellner, "Measuring wavelengths and lattice constants with the Mössbauer wavelength standard," J. Synchrotron Rad. **9**, 17-23 (2002).

S. K. Sinha, "Theory of Inelastic X-ray Scattering from Condensed Matter," J. Phys. Condens. Matter **13**, 7511-7523 (2001).

S. K. Sinha, "The Impact of Synchrotron Radiation on Nanoscience," Appl. Surf. Sci. **182**, 176-185 (2001).

H. Sinn, E. E. Alp, A. Alatas, J. Barraza, G. Bortel, E. Burkel, D. Shu, W. Sturhahn, J. P. Sutter, T. S. Toellner, J. Zhao, "An Inelastic X-ray Spectrometer with 2.2 meV Energy Resolution," Nucl. Instrum. Methods A **467-468**, 1545-1548 (2001).

H. Sinn, "Spectroscopy with meV Energy Resolution," J. Phys. Condens. Matter **13**, 7525-7537 (2001).

R. K. Smither, D. E. Roa, "The Physics of Medical Imaging with Crystal Diffraction Lenses," Proc. SPIE Vol. **4320**, *Physics of Medical Imaging*, L.E. Antonuk and M.J. Yaffe, eds. (2001) pp. 447-458.

Y. -A. Soh, P. G. Evans, Z. Cai, B. Lai, C. -Y. Kim, G. Aeppli, N. D. Mathur, M. G. Blamire, E. D. Isaacs, "Local mapping of strain at grain boundaries in colossal magnetoresistive films using x-ray microdiffraction," J. Appl. Phys. **91**, 7742-7744 (2002).

M. Sowwan, Y. Yacoby, J. Pitney, R. MacHarrie, M. Hong, J. Cross , D. A. Walko, R. Clarke, E. Stern, "Direct atomic structure determination of epitaxially grown films:Gd2O3 on GaAs (100)," Phys. Rev. B **66**, 205311-1-12 (2002).

A.P. J. Stampfl, E. S. Friedman, T. J. Wilkinson, E. E. Alp, K. A. Yener, "Shedding Light on the Past," Nucl. Instrum. Methods A **467-468**, 1305-1307 (2001).

G. B. Stephenson, B. Stephenson, D. R. Haeffner, "Investigations of Astrolabe Metallurgy Using Synchrotron Radiation," MRS Bull. **26**, 19-23 (2001).

S. R. Stock, K. Ignatiev, W.- K. Lee, K. Fezzaa, G. R. Davis, J. C. Elliott, "Comparison of Crack Geometry Determined with Phase Contrast Radiography and with Microtomography," Mat. Res. Soc. Symp. Proc. **678** (2001) pp. EE3.6.1-EE3.6.6.

S. R. Stock, J. Barss, T. Dahl, A. Veis, J. D. Almer, "X-ray Absorption Microtomography (microCT) and Small Beam Diffraction Mapping of Sea Urchin Teeth," J. Struct. Biol. **139**, 1-12 (2002).

V. V. Struzhkin, H-K Mao, J. Hu, M. Schwoerer-Böhning, J. Shu, R. J. Hemley, W. Sturhahn, M. Y. Hu, E. E. Alp, P. Eng, G. Shen, "Nuclear Inelastic X-ray Scattering of FeO to 48 GPa," Phys. Rev. Lett. **87**, 255501-1-4 (2001).

W. Sturhahn, "Phase Problem in Synchrotron Mössbauer Spectroscopy," Phys. Rev. B **63**, 094105-1-5 (2001).

W. Sturhahn, T. S. Toellner, "Quantification of contaminants to incoherent nuclear resonant scattering," Phys. Rev. B **65**, 134305-1-12 (2002).

J. P. Sutter, E. E. Alp, M. Y. Hu, P. L. Lee, H. Sinn, W. Sturhahn, T. S. Toellner, G. Bortel, R. Colella, "Multiple-Beam X-ray Diffraction near Exact Backscattering in Silicon," Phys. Rev. B **63**, 094111-1-12 (2001).

G. Tajiri, A. Khounsary, D. Mancini, "A Simple and Effective Modification of a Sagittally Focusing X-ray Diffraction Optic," Proc. SPIE Vol. **4145**, A.K.Freund, T. Ishikawa, A.M. Khounsary, D.C. Mancini, A.G. Michette, and S. Oestreich, eds. (2001) pp. 114-121.

G. Tajiri, W.- K. Lee, P. Fernandez, D. Mills, L. Assoufid, F. Amirouche, "Nonlinear, Thermal-Distortion Predictions of a Silicon Monochromator Using the Finite Element Method," J. Synchrotron Rad. **8**, 1140-1148 (2001).

A. Thompson, J. Underwood, E. Anderson, S. McHugo, B. Lai, "Characterization of the Focal Quality of Micron Size Beams fron X-ray Mirrors and Zone Plates," Proc. SPIE Vol. **4145**, A.K. Freund, et al., eds. (2001) pp. 16-21.

T. S. Toellner, M. Y. Hu, W. Sturhahn, G. Bortel, E. E. Alp, J. Zhao, "Crystal Monochromator with a Resolution beyond 10[sup 8]," J. Synchrotron Rad. **8**, 1082-1086 (2001).

M. Ulmer, R. I. Altkorn, M. E. Graham, A. Madan, Y. S. Chu, "Production and performance of multilayer coated conic sections," Proc. SPIE Vol. **4496**, P. Gorenstein and R.B. Hoover, eds. (2002) pp. 127-133.

L. Vasiliu-Doloc, R. Osborn, S. Rosenkranz, J. Mesot, J. F. Mitchell, S. K. Sinha, O. H. Seeck, J. W. Lynn, Z. Islam, "Neutron and X-ray Evidence of Charge Melting in Ferromagnetic Layered Colossal Magnetoresistance Manganites," J. Appl. Phys. **89**, 6840-6845 (2001).

M. von Zimmerman, C. S. Nelson, J. P. Hill, D. Gibbs, M. Blume, D. Casa, B. Keimer, Y. Murakami, C. -C Kao, C. Venkataraman, T. Gog, Y. Tomioka, Y. Tokura, "X-ray Resonant Scattering Studies of Orbital and Charge Ordering in $Pr_{1-x}Ca_xMnO_3$," Phys. Rev. B **64**, 195133-1-17 (2001).

M. von Zimmermann, C. S. Nelson, J. P. Hill, D. Gibbs, M. Blume, D. Casa, B. Keimer, Y. Murakami, C. C. Kao, C. Venkataraman, T. Gog, Y. Tomioka, Y. Tokura, "X-ray Resonant Scattering Studies of Charge and Orbital Ordering in $Pr_{1-x}Ca_xMnO_3MnO3$," J. Magn. Magn. Mater. **233**, 31-37 (2001).

Y. D. Wang, X.-L. Wang, A. D. Stoica, J. D. Almer, U. Lienert, D. R. Haeffner, "Separating the recrystallization and deformation texture components by high-energy x-rays," J. Appl. Crystallogr. **35**, 684-688 (2002).

Y. X. Wang, F. De Carlo, D. C. Mancini, I. McNulty, B. Tieman, J. Bresnahan, I. Foster, J. Insley, P. Lane, G. von Laszewski, C. Kesselman, M.- H. Su, M. Thiebaux, "A High-Throughput X-ray Microtomography System at the Advanced Photon Source," Rev. Sci. Instrum. **72**, 2062-2068 (2001).

A. P. Wilkinson, C. Lind, S. R. Stock, K. E. Kurtis, N. Naik, D. R. Haeffner, P. L. Lee, "Mapping the Distribution of Corrosion Products in Cement Exposed to Sulfate Using Energy Dispersive X-ray Diffraction," Mat. Res. Soc. Symp. Proc. (2001) p. 678.

A. P. Wilkinson, C. Lind, R. A. Young, S. D. Shastri, P. L. Lee, G. S. Nolas, "Preparation, transport properties and structure analysis by resonant x-ray scattering of the type-1 clathrate $Cs_8Cd_4Sn_{42}$," Chem. Mater. **14**, 1300-1305 (2002).

T. J. Wilkinson, E. S. Friedman, E. E. Alp, A.P J. Stampfl, "The Geoarchaeology of a Lake Basin: Spatial and Chronological Patterning of Sedimentation in the Amuq Plain, Turkey," Researches en Archeometrie, ed., M. Fortin (Laval University, 2001) pp. 211-226.

G. Xu, X. Su, C. B. Stagarescu, D. E. Eastman, B. Lai, Z. Cai, I. C. Noyan, C.- K. Hu, "Quantitative Metrology Study of Cu/SiO_2 Interconnect Structures Using Fluorescence X-ray Microscopy," Appl. Phys. Lett. **78**, 820-822 (2001).

S. Xu, B. Lai, Z. Cai, D. Shu, "Vibration-damping structure for an x-ray microprobe supporting system," Rev. Sci. Instrum. **73**, 1599-1601 (2002).

Y. Yoo, T. Ohnishi, G. Wang, F. Duewer, X.-D. Xiang, Y. S. Chu, D. M. Mancini, Y.- Q. Li, R. C. O'Handley, "Continuous Mapping of Structure-Property Relation in $Fe_{1-x}Ni_x$ Metallic Alloys Fabricated by Combinatorial Synthesis," Intermetallics **9**, 541-545 (2001).

Y. Yue, C. F. Powell, R. Poola, J. Wang, M.-C. Lai, S. E. Parrish, "Quantitative Measurements of Direct-Injection Gasoline Fuel Sprays in the Near-Nozzle Region Using Synchrotron X-rays," SAE Technical Paper Series, 2001-01-1293, Society of Automotive Engineers (2001) pp. 1-6.

Y. Yue, C. Powell, R. Cuenca, R. Poola, J. Wang, "Synchrotron X-ray Messurement of Direct Injection Gasoline Fuel Sprays," Proc. ASME 2001: *Diesel Combustion and Emissions, Fuel Injection and Sprays*, V.W. Wong, ed., ICE-Vol. **37-1** (2001) pp. 109-113.

P. Zambianchi, S. D. Shastri, D. M. Mills, "Numerical Simulations of Dynamically Diffracted Ultrashort X-ray Free-Electron Laser Pulses," Proc. SPIE Vol. 4500 (2001) pp. 75-88.

Y. Zhang, P. L. Lee, G. S. Nolas, A. P. Wilkinson, "Gallium distribution in the clathrates $Sr_8Ga_{16}Ge_{30}$ and $Sr_4Eu_4Ga_{16}Ge_{30}$ by resonant diffraction," Appl. Phys. Lett. **80**, 2931-2933 (2002).

J. Y. Zhao, E. E. Alp, T. S. Toellner, W. Sturhahn, H. Sinn, D. Shu, "A water-cooled compound refractive lens as a white beam collimator," Rev. Sci. Instrum. **73**, 1611-1613 (2002).

J. Y. Zhao, T. S. Toellner, M. Y. Hu, W. Sturhahn, E. E. Alp, G. Y. Shen, H. K. Mao, "High-energy-resolution monochromator for [83]Kr nuclear resonant scattering," Rev. Sci. Instrum. **73**, 1608-1610 (2002).